NATIONAL TECHNICAL UNIVERSITY OF ATHENS
Multidisciplinary Master Program Computational Mechanics
School of Mechanical Engineering
Parallel CFD & Optimization Unit

Investigation on Meshing Techniques for the CFD Modelling of Rotating Wheels in Cars

Master Thesis

Alexandros Papakonstantinou

Supervisor: Kyriakos C. Giannakoglou,
Professor NTUA

Industrial Supervisor: Antoine Delacroix
Manager TME

Athens, February 2021

NATIONAL TECHNICAL UNIVERSITY OF ATHENS
Multidisciplinary Master Program Computational Mechanics
School of Mechanical Engineering
Parallel CFD & Optimization Unit

Investigation on Meshing Techniques for the CFD Modelling of Rotating Wheels in Cars

Master Thesis

Alexandros Papakonstantinou

Supervisor: Kyriakos C. Giannakoglou, Professor NTUA

Athens, February 2021

Abstract

This thesis presents the application and assessment of the Sliding Mesh (SM) method in the computational flow prediction around a Toyota passenger car with rotating wheels. The wheels motion is commonly modelled using simplistic approximations of the rotating motion such as the Rotating Wall Boundary Condition (RWBC) or the Multiple Reference Frame (MRF) method, both introducing a number of drawbacks. In the contrary, the SM method utilizes a realistic mesh rotation in real time and is characterized to be highly accurate in the prediction of the flow regimes around rotating bodies.

Rotating car wheels have a great contribution in the aerodynamic resistance which is one of the major energy loss factors in passenger vehicles. Accurate prediction of the flow around them, at the lowest possible cost, is highly demanded for the design of more aerodynamic vehicles. As new emission regulations put stricter demands on modern automotive industry, the aerodynamic development of cars and wheels is now emerging.

The application of the SM method for rotating wheels was carried out using snappyHexMesh mesh generator and the Arbitrary Mesh Interface (AMI) technique for the coupling of the stationary and the rotating mesh regions, as both implemented in the open source software *OpenFOAM*©. The AMI coupling is used for the computation of the fluxes at the non-matching AMI interface. The quality of the AMI coupling relies heavily upon the meshing and loss of conservativeness at the interfaces may occur in cases of low mesh quality.

To this end, a preliminary investigation over the parameters of the snappyHexMesh and the AMI shape was carried out for a single rotating wheel, in order to determine a robust meshing technique, capable of delivering both high mesh quality at the interfaces and relatively low run times. Flow simulations over a single rotating wheel were conducted using the SM method in order to evaluate the impact of the AMI quality on the flow as well as the run time. The latter was found to be highly affected from the AMI face count rather than the overall mesh size.

The meshing technique obtained by the parametric study was applied in a flow simulation around a passenger car with rotating wheels. Flow analysis was carried out with the computation of the time-dependent Navier-Stokes equations using the Spalart-Allmaras DDES turbulence model with wall functions. The SM method's results were compared with those of the RWBC method, MRF model and data from experimental measurements. The SM method proved to be much more accurate in the prediction of the drag coefficient, at the expense of higher computations cost though.

Major part of this work was carried out in the premises of Toyota Motor Europe (TME) in Brussels, Belgium, during a 6 month long internship, with Mr. Antoine Delacroix as the industrial advisor.

ΕΘΝΙΚΟ ΜΕΤΣΟΒΙΟ ΠΟΛΥΤΕΧΝΕΙΟ

Διατμηματικό Πρόγραμμα Μεταπτυχιακών Σπουδών 'Υπολογιστική Μηχανική'
Σχολή Μηχανολόγων Μηχανικών
Μονάδα Παράλληλης Υπολογιστικής Ρευστομηχανικής & Βελτιστοποίησης

Διερεύνηση Τεχνικών Πλεγματοποίησης στη CFD Μοντελοποίηση Περιστροφής Τροχών Αυτοκινήτων

Μεταπτυχιακή Εργασία

Αλέξανδρος Παπακωνσταντίνου

Επιβλέπων: Κυριάκος Χ. Γιαννάκογλου, Καθηγητής ΕΜΠ

Αθήνα, Φεβρουάριος 2021

Περίληψη

Η διπλωματική εργασία αυτή αποσκοπεί στην εφαρμογή της μεθόδου Ολισθαίνοντος Πλέγματος (Sliding Mesh-SM) στην υπολογιστική πρόλεξη ροής γύρω από επιβατικό όχημα Toyota με περιστρεφόμενους τροχούς. Οι επικρατέστερες μέθοδοι μοντελοποίησης της περιστροφής των τροχών είναι απλοικές προσεγγίσεις της περιστροφικής κίνησης όπως η επιβολή μη-μηδενικής εφαπτομενικής ταχύτητας (rotatingWallVelocity Boundary Condition - RWBC) και η μέθοδος Πολλαπλών Συστημάτων Αναφοράς (Multiple Reference Frame - MRF), παρουσιάζοντας και οι δύο αριθμό μειονεκτημάτων. Αντιθέτως, μέσω της μέθοδου του Ολισθαίνοντος Πλέγματος υλοποιείται πραγματική περιστροφή του πλεγματικού χωρίου αποτελώντας μία από τις πιο ακριβείς μεθόδους πρόλεξης ροών γύρω από περιστρεφόμενα σώματα.

Η περιστροφή των τροχών επιδρά σε πολύ μεγάλο βαθμό στην αεροδυναμική αντίσταση των επιβατικών αυτοκινήτων. Η ακριβής πρόλεξη του συντελεστή αεροδυναμικής αντίστασης και των ροικών πεδίων γύρω από τους τροχούς, αποτελούν βασική προυπόθεση για αεροδυναμικό σχεδιασμό των τροχών. Με την θέσπιση νέων αυστηρότερων νομικών πλαισίων σχετικά με τις εκπομπές ρύπων, ο αεροδυναμικός σχεδιασμός με στόχο την ελαχιστοποίηση των απωλειών ενέργειας των επιβατικών οχημάτων καθιστάται πλέον απαραίτητος.

Για την εφαρμογή του Ολισθαίνοντος Πλέγματος χρησιμοποιήθηκε το λογισμικό γένεσης πλέγματος snappyHexMesh, και η τεχνική Διεπαφής Αυθαίρετων Πλεγμάτων (Arbitrary Mesh Interface - AMI) για την σύζευξη του στατικού και περιστρεφόμενου πλεγματικού χωρίου στο λογισμικό ανοιχτού κώδικα $OpenFOAM^{©}$. Η AMI τεχνική πραγματοποιείται για τον υπολογισμό των ροών στη μη-σύμμορφη AMI διεπιφάνεια. Χαμηλής ποιότητας πλεγματοποίηση οδηγεί στην εισαγωγή σφαλμάτων διατήρησης τοπικά στην AMI διεπιφάνεια.

Για αυτό το λόγο, προκατασκευαστικά πραγματοποιήθηκε διερεύνηση των παραμέτρων του πλεγματοποιητή snappyHexMesh και της AMI γεωμετρίας σε μεμονωμένο τροχό, με στόχο το σχεδιασμό μιας εύρωστης τεχνικής πλεγματοποίησης ικανής να αποδώσει υψηλής ποιότητας πλέγμα στην AMI διεπιφάνεια και χαμηλό χρόνο επίλυσης. Πραγματοποιήθηκε συγκριτική μελέτη ανάμεσα σε τέσσερις διαφορετικές διεπιφάνειες και αξιολογήθηκε η επίδραση των AMI βαρών στη διαμόρφωση των ροικών πεδίων και στο χρόνο επίλυσης. Ο χρόνος επίλυσης βρέθηκε να επηρεάζεται από το πλήθος των επιφανειακών κελιών πάνω στη διεπιφάνεια παρά από το συνολικό μέγεθος του πλέγματος.

Η τεχνική πλεγματοποίησης στην οποία κατέληξε η παραπάνω παραμετρική μελέτη, εφαρμόστηκε στη προσομοίωση ροής γύρω από επιβατικό αμάξι με περιστρεφόμενους τροχούς. Η πρόλεξη του ροικού πεδίου πραγματοποιήθηκε με επίλυση των εξισώσεων Navier-Stokes για ασυμπίεστο ρευστό σε χρονικά μεταβαλλόμενη τυρβώδη ροή. Το μοντέλο τύρβης που χρησιμοποιήθηκε είναι το Spalart-Allmaras DDES με συναρτήσεις τοίχου. Τα υπολογιστικά αποτελέσματα της μεθόδου Ολισθαίνοντος Πλέγματος, συγκρίθηκαν με αποτελέσματα ανάλυσης με χρήση της οριακής συνθήκης Εφαπτομενικής Ταχύτητας, της μέθοδου Πολλαπλών Συστημάτων Αναφοράς αλλά και πειραματικών μετρήσεων. Η μέθοδος Ολισθαίνοντος Πλέγματος αποδείχθηκε πιο ακριβής στον υπολογισμό του συντελεστή αντίστασης αλλά με πολύ μεγαλύτερο χρόνο επίλυσης.

Το μεγαλύτερο μέρος της διπλωματικής εργασίας πραγματοποιήθηκε στις εγκαταστάσεις της Toyota Motor Europe (TME) στις Βρυξέλλες, Βέλγιο, κατά τη διάρκεια 6-μηνης πρακτικής άσκησης, με τον κ. Antoine Delacroix ως επιβέποντα από τη μεριά της βιομηχανίας.

Acknowledgements

First and foremost, I would like to express my gratitude and thankfulness to my professor, Kyriakos C. Giannakoglou, for providing me with his reliance offering me the unique opportunity to undertake this master thesis. It has been a life changing experience for me. His trust along the way and his guidance played a main role in this work completion.

Also, I would like to truly thank my industrial manager, Mr. Antoine Delacroix, as most of the part of this thesis took part in the premises of Toyota Motor Europe. Under his valuable and accurate instructions, and mostly his experienced perspective, this master thesis was a deeply interesting experience. His patience and generosity on explaining new things, both in the technical aspect and in working culture help me expand my skills in undertaking projects like this.

My grateful thanks are also extended to my colleague Panagiotis Koutsantonis, for his constant and honest support on me throughout this work providing the chance to collaborate with a high level R&D employees. Also, I would to place my special gratitude also to my colleague Pablo Fernandez for offering me his time and his guidance on technical procedures essential to this thesis.

Many thanks also must be expressed to Dr. E. M. Papoutsis-Kiachagias, member of the Parallel CFD & Optimization Unit of NTUA, for his radical advise and support whenever I needed him.

Last but not least, I would like to thank my friend Thodoris Niforos for his support and companionship along the way.

Acronyms

NTUA	National Technical University of Athens
PCopt	Parallel CFD & Optimization Unit
TME	Toyota Motor Europe
CFD	Computational Fluid Dynamics
CAD	Computer Aided Design
CAE	Computer Aided Engineering
OpenFOAM	Open Field Operation And Manipulation
PDE	Partial Differential Equation
CPU	Central Processing Unit
RANS	Reynolds-Averaged Navier-Stokes
DDES	Delayed Detached Eddy Simulation
DES	Detached Eddy Simulation
DNS	Direct Numerical Simulation
URANS	Unsteady Reynolds-Averaged Navier-Stokes
N-S	Navier-Stokes
AMI	Arbitrary Mesh Interface
SM	Sliding Mesh
MRF	Multiple Reference Frame
BC	Boundary Condition
RWBC	Rotating Wall Boundary Condition
LIC	Line Integral Convolution
WT	Wind Tunnel
HPC	High Performance Computing
w.r.t	with respect to

Contents

1. Introduction

1.1 Car Aerodynamics and Efficient Mobility

Over the past two decades, modern industry and research focus more and more on the development of efficient mobility solutions in a zero-emission perspective. New stricter legislations over fuel consumption and CO2 emissions for passenger cars have put a heavy demand on the automotive industries to focus on a more energy efficient vehicle development. Transport is responsible for almost 30% of the EU's total CO2 emissions, of which nearly the 70% comes from road transportation. Passenger cars are responsible for around the 12% of this percentage. Since 2015, the first targets for mandatory emission reduction from EU legislation apply for new cars. As part of the efforts to reduce the CO2 emissions, EU has set the target of reducing emissions from transport by 30% by 2030 and by 60% by 2050 compared to 1990 levels, [1].

In order for car manufacturers to tackle current challenges, excessive focus must be put on the study of the car aerodynamics as this has a huge impact on the vehicles energy consumption performance. The development of fast and accurate CFD solutions and their integration to an industrial vehicle design workflow, offers great potential to the flow prediction over multiple car models in relatively lower time and cost compared to wind tunnel measurements.

1.2 Aerodynamic Drag of Vehicle

One of the main key performance indicators (KPIs) for the aerodynamic design of a car is the aerodynamic drag. The aerodynamic drag expresses the resistance the vehicle has to overcome while it moves into the air with a certain speed and shape. In this perspective, one of the main objectives of the aerodynamic development of a car focuses on the accurate prediction of the aerodynamic drag. The capability of the accurate computation of the drag of a vehicle offers engineers the ability to drive the vehicle design to the direction of drag reduction. Particularly the automotive sector is highly involved in this aspect because aerodynamic resistance is connected to the increase in fuel consumption, CO2 emissions, noise and driving instabilities.

Aerodynamic drag can be considered and studied as a result of two different phenomena that are developed on the surface of the body, due to its shape and the physical properties of both the fluid and the solid that is moving across the fluid. One of the sources of the aerodynamic drag is the skin friction between the fluid molecules and the surface of the body. The friction forces on a surface depend on its roughness, meaning that a rough surface shows more surface friction than a smooth one. The magnitude of the surface friction depends on the viscosity of the fluid and the Reynolds number. The second source of aerodynamic drag is the pressure distribution exerted normal to the body's surface. By the integration of both the friction and pressure distribution over the body's surface, the resulting force F and moment M are derived. The resulting total force F and moment M are decomposed into three components each w.r.t. the axes of the coordinated system used. In a simplified 2D problem, taking into account the freestream velocity $\vec{U}_\infty$, the main forces of interest are the lift which is the perpendicular to $\vec{U}_\infty$ and drag which is in the parallel direction of $\vec{U}_\infty$ and in the opposite direction of the vehicle's motion.

Thus, the aerodynamic drag is one of the forces the car must overcome in order to move forward through the air. The higher the value of the aerodynamic drag the more energy the vehicle requires in order to move. In the vehicle development, among other performance characteristics (noise, design, ergonomy etc.), the aerodynamic drag coefficient (C_D) is the main target from the aerodynamic point of view. C_D is the non-dimensional drag force, w.r.t. the basic flow quantities, such as the dynamic pressure of the flow q_∞ and the frontal area of the vehicle S. With ρ_∞ being the air density and U_∞ as the free-stream air velocity, the dynamic pressure can be derived as $q_\infty = \frac{1}{2}\rho_\infty U_\infty^2$. The drag coefficient is computed using the following formula:

$$C_D = \frac{D}{q_\infty S} \tag{1.1}$$

Similar non-dimensional coefficients are derived for the rest of the forces acting on the solid body moving through the air. The commonly used aerodynamic coefficients are the lift coefficient $C_L = \frac{L}{q_\infty S}$ and the moment coefficient $C_M = \frac{M}{q_\infty S l}$.

1.2.1 Aerodynamic Impact of Rotating Wheels

A typical passenger vehicle mainly consists of four different areas, the upper-body, the under-body, the engine-cooling and the wheels. About 50% of the total aerodynamic drag is generated from the upper body and the engine-cooling, as in the same time the under-body is responsible for 20% of the total aerodynamic drag. Wheels and wheel-houses generate up to 30% of the total drag, [2]. Extended focus has been put especially on the aerodynamic study and optimization of the upper

body of the car which is also closely related to the aesthetic result of the automotive product. Nowadays, research switches to the wheels and the wheel-houses. The study of the aerodynamics and the improvement of these areas, in a drag reduction perspective keeping the aesthetic design a constant objective, are gradually becoming so important.

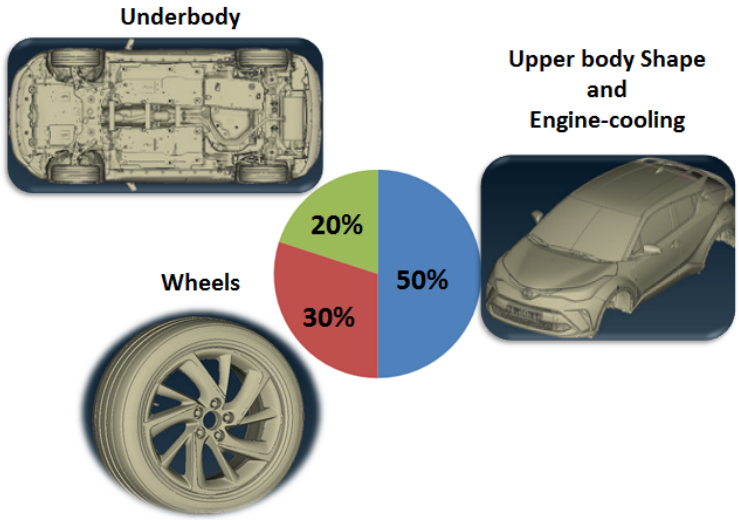

Figure 1.1: Contribution to overall drag of different parts of the vehicle.

The flow around the wheels is very complex due to the intense turbulence developed by the rotating wheel and the contact patch between the tire and the road, resulting to a highly unsteady flow regime. The grooves on the tire and the design of the rim have a huge impact on the aerodynamic drag, thus, wheels must be designed by balancing commercial design and minimizing drag.

Despite the huge influence of the wheel rotation on the aerodynamic performance of vehicles, modelling of wheels rotation is still and open issue. CFD simulations, most common practice makes assumptions and uses simple models to mimic mesh rotation and approximate the wheel angular motion. These assumptions lead to differences between the numerical simulations and the wind tunnel measurements. At first, the rotation of the tire and the rim is commonly approximated using the Rotating Wall Boundary Condition (RWBC), by which the velocity vector is imposed tangential to the rotating wheel (the boundary condition of the velocity at the wheel's points is a Dirichlet type; velocity should be equal to the linear velocity of the rotation at this radius). This method shows a low demand in computational resources and easy implementation but, due to the complexity of the rims, a large portion of the surface will be modelled erroneously [36]. The RWBC method can be used both in steady and unsteady flow solvers.

Another method for the modelling of the rim rotational motion is the Multiple Frame of Reference (MRF) method, by which the rims are enclosed in a separate mesh region inside of which the governing flow equations are solved w.r.t. a relative reference frame and additional source terms are added in the momentum equations approximating the rotational motion without though moving the mesh. The MRF method shows low accuracy and low simulations run-time since this is also based on a steady flow model.

In the contrary, the SM method performs a real mesh rotation implementing a simulation of the rotating motion which is very close to the real-life scenario. Compared with the RWBC and the MRF methods, the SM method delivers more accurate results for the rotating rims simulation [29],[36]. Thus, the SM is considered to be the state of the art in the simulation of the rotating motion of the car wheels. The integration of the SM method to a vehicle development workflow is an important tool offering the potential for a far better understanding of the flow phenomena generated around the car's wheels and lead to the design of more aerodynamic wheels and cars in cost of higher run times, since an unsteady CFD code must be used.

1.3 CFD applications and Numerical Mesh Generation

CFD aerodynamic analysis have already established their solid ground among the industrial vehicle development procedures, as a valuable tool to further gain insight in the fluid phenomena related to the vehicle's aerodynamic performance. Also CFD analysis can be used in order to perform aerodynamic shape optimization (e.g. by using the adjoint method), leading to aerodynamically improved designs. CFD also offers the benefit to the industrial vehicle development to avoid costly, time consuming and polluting wind tunnel testings. In this way, based on a relatively fast and accurate CFD code, more car designs can be reliably evaluated accelerating the vehicle development workflow.

Every CFD analysis begins with the generation of the computational mesh, which nowadays stands as an individual area of study among the CAE technologies. The accuracy and speed of the flow analysis is vastly depended on the quality of the generated numerical mesh. Among the huge variety of open source and commercial mesh generation software, in this work, the snappyHexMesh mesh generator is used which is available in the main distribution of *OpenFOAM*©.

The SM method operation itself is heavily dependent on the quality of the mesh, the generation of which is a vital part of this work. The rotating region must be identified in the mesh generation stage, and the mesh quality on the interfaces that couple the rotating and the stationary mesh regions are of high importance for accuracy of the SM method. Mesh generation must first ensure a high quality geometry

representation of the interface in the coupling area and, then, proceed to the flow analysis.

1.4 Scope and Structure of the Thesis

The scope of this thesis is to assess the SM method for its accuracy benefits on the car wheels rotation using the snappyHexMesh for the CFD mesh generation. The AMI technique for the coupling of the rotating and stationary mesh regions will be used. A preliminary investigation over the snappyHexMesh parameters and the AMI interface's shape is being carried out in a single rotating wheel, for a robust meshing technique delivering well resolved AMIs to be obtained. The outcome of the latter parametric investigation will be used in the application of the SM method for the flow simulation over a passenger car with rotating wheels. The results will be compared with the standard aero workflow results and the experimental data.

The thesis outline is introduced below:

- **Chapter 2:** The RANS equations solved to predict the turbulent flow field around the rotating wheel and the car are being presented. Also, the turbulence modelling and the wall treatment is analyzed.
- **Chapter 3:** The main concept of the wheel aerodynamics is given and the different modelling approaches of the wheel rotation are introduced.
- **Chapter 4:** The snappyHexMesh mesh generator is analyzed and the bottlenecks and the optimal meshing solutions are introduced.
- **Chapter 5:** At first, the snappyHexMesh parameter investigation is presented in a standalone wheel, targeting the development of a robust meshing process for high quality mesh at the AMI interfaces. After that, four differently weighted AMI interfaces are used for the simulation of the wheel's rotation and their impact on the flow characteristics and results are discussed. Finally, the SM method is applied to simulate the air flow around a car with rotating wheels. These results are compared with the corresponding RWBC, MRF and experimental results.
- **Chapter 6:** Conclusions are made along with proposal for future work as well as some further improvements.

2. CFD Analysis

2.1 Flow Modelling

The differential equations used to describe the motion of viscous fluid flows are the Navier-Stokes (N-S) equations. The generic form of these equations for incompressible flows with constant molecular viscosity are presented in equations 2.1 and 2.2 expressing the conservation of mass and conservation of momentum respectively.

$$\nabla \cdot u = 0 \tag{2.1}$$

$$\rho \frac{DV}{Dt} = -\nabla p + \mu \nabla^2 V \tag{2.2}$$

where u is the velocity component, p is the pressure, ρ is the fluid density and μ the viscosity coefficient which is assumed constant.

This work focuses on the external flow around a moving vehicle and its rotating wheels which is characterized as highly turbulent. This means that all the flow variables are governed by intensively unsteady fluctuations in their distribution in the fluid domain, and chaotic changes occur in the pressure and velocity flow variables. This fluctuations occur in very small time scales and caused at a point by convection of eddies of many size and time scales. As these eddies move through the flow the velocity field changes arbitrarily at a fixed point in the domain. In turbulent flows, the vortices of different sizes interact with each other and result in an important increase in friction drag and thus, the energy needed by a body to pass through a turbulent flow field is increased.

2.2 Turbulence Modelling

For the simulation of turbulent flows and the resolution of the extremely small scale fluctuations of the flow quantities many different methods have been developed. Very small discretization of the turbulent flow domain in time and space is needed in order to resolve the time and spacial scales. This is the so-called Direct Numerical Simulations (DNS), [3], which has an unbearably large computational cost. So, in industrial applications turbulence must be modelled.

2.2.1 Reynolds Averaged Navier Stokes Equations (RANS)

One of the main ideas around the turbulence modelling comes from the Reynolds or time-averaging of the instantaneous N-S equations. This leads to the RANS equations which is one of the simplest and reliable available approach.

The idea behind the equations is the Reynolds decomposition, which can be summarized in the formula $u(x,y,z) = \overline{u(x,y,z)} + u'(x,y,z)$, whereby an instantaneous quantity is decomposed into its time-averaged and fluctuating component. By applying the Reynolds decomposition to all the flow variables, the time-averaged N-S equations in Einstein notation and in Cartesian coordinates can be written as follows:

$$\frac{\partial \overline{u_j}}{\partial x_j} \tag{2.3}$$

$$\rho \overline{u_j} \frac{\partial \overline{u_i}}{\partial x_j} = \rho \overline{f_i} - \frac{\partial \overline{p}}{\partial x_i} + \frac{\partial}{\partial x_j}\left[\mu\left(\frac{\partial \overline{u_i}}{\partial x_j} + \frac{\partial \overline{u_j}}{\partial x_i}\right) - \rho \overline{u_i' u_j'}\right] \tag{2.4}$$

In the above relation, the term $\rho \frac{\partial \overline{u_i}}{\partial t}$ is added in the momentum equations (2.4), to formulate the Unsteady Reynolds-Averaged Navier Stokes Equations (URANS). The non-linear term $\left(-\rho \overline{u_i' u_j'}\right)$ is an apparent stress term, owing to the fluctuating velocity field. This term stands for the so-called **Reynolds stresses**. At this point, the Boussinesq hypothesis is made in order to model the Reynolds stresses resulting to an additional unknown field and the derivation of a new quantity known as the turbulent viscosity ν_t. The Boussinesq hypothesis is presented below:

$$\tau_{ij}' = -\rho \overline{u_i' u_j'} = \rho \nu_t \left(\frac{\partial \overline{u_i}}{\partial x_j} + \frac{\partial \overline{u_j}}{\partial x_i}\right) - \frac{2}{3} k \delta_i j \tag{2.5}$$

where $k = \frac{1}{2}\overline{u_i' u_i'}$ and the τ_{ij}' denotes Reynolds stress term.

In order for the ν_t to be computed, additional equations are needed for the closure of the system of equations. The issue of the 'problem closure', is tackled by the use of turbulence models.

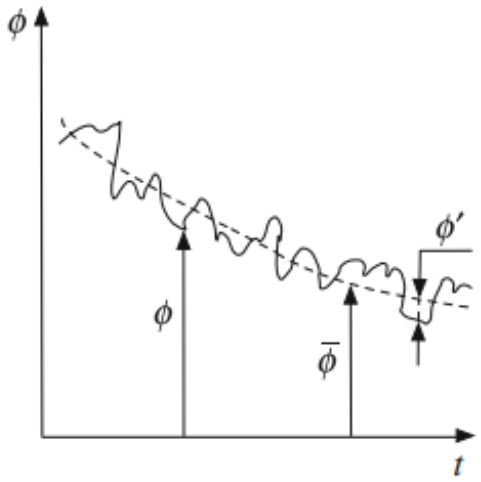

Figure 2.1: Simplified representation of the mean $\overline{\phi}$ quantity value(continuous line) and the instantaneous fluctuating ϕ' quantity value [4]

2.2.2 The Spalart-Allmaras (S-A) Turbulence Model

In this work, the S-A [5] turbulence model is used which is a one equation mixing-length turbulence model for incompressible flows. It was designed for aerospace applications involving wall-bounded flows and has been shown to give good results for boundary layers subjected to adverse pressure gradients. The S-A model solves a modelled transport equation (2.9) for the model variable $\widetilde{\nu}$ so it is not necessary to compute a length scale related to the local shear layer thickness. In its original form, the model is effectively a low-Reynolds number model ($y^+ \sim 1$)[1], requiring the viscosity-affected region of the boundary layer to be properly resolved.

The turbulent (eddy) viscosity is given by

$$\nu_t = \widetilde{\nu} f_{v1} \tag{2.6}$$

$$f_{v1} = \frac{X^3}{X^3 + C_{V1}^3} \tag{2.7}$$

$$X = \frac{\widetilde{\nu}}{\nu} \tag{2.8}$$

[1] y^+ stands for the non-dimensional distanse from the wall, defined as $y^+ = \frac{\upsilon_\tau y}{\nu}$, y is the distance from the wall boundary, ν is the kinematic viscosity and $\upsilon_\tau = \sqrt{\frac{\tau_w}{\rho}}$ being the friction velocity where τ_w is wall shear stress. Here, y^+ corresponds to the distance of the first cell center from the wall, and determines the resolution of the mesh near to the wall boundaries of the computational domain.

The main model PDE of the S-A model follows:

$$\frac{\partial(\widetilde{\nu}u_i)}{x_j} = C_{b1}(1-f_{t2})\widetilde{S}\widetilde{\nu}+\frac{1}{\sigma}\left[\frac{\partial}{x_j}\left((\nu+\widetilde{\nu})\frac{\widetilde{\nu}}{x_j}\right)+C_{b2}\frac{\partial\widetilde{\nu}}{\partial x_i}\frac{\partial\widetilde{\nu}}{\partial x_i}\right]-\left[C_{w1}f_w-\frac{C_{b1}}{\kappa^2}f_{t2}\right]\left(\frac{\widetilde{\nu}}{d}\right)^2 \tag{2.9}$$

The model's constants are $\sigma = 2/3$, $C_{b1} = 0.1355$, $C_{b2} = 0.622$,$\kappa = 0.41$. $C_{w1} = 3.239$, $C_{v1} = 7.1$. The variable d is the distance of each field point from the nearest wall and $\widetilde{S}$,f_{t2},f_w are derived using:

$$\widetilde{S} = \Omega + \frac{\widetilde{\nu}}{\kappa^2 d^2} f_{v2} \tag{2.10}$$

$$\Omega = \sqrt{2W_{ij}W_{ij}} \tag{2.11}$$

$$W_{ij} = \frac{1}{2}\left(\frac{\partial u_i}{\partial x_j} - \frac{\partial u_j}{\partial x_i}\right) \tag{2.12}$$

$$f_{v2} = 1 - \frac{X}{1 + X f_{v1}} \tag{2.13}$$

$$f_w = g\left[\frac{1 + c_{w3}^3}{g^6 + c_{w3}^3}\right]^{1/6} \tag{2.14}$$

$$g = r + c_{w2}(r^6 - 6) \tag{2.15}$$

$$r = min\left[\frac{\widetilde{\nu}}{\widetilde{S}\kappa^2 d^2}, 10\right] \tag{2.16}$$

$$f_{t2} = c_{t3} e^{c_{t3}X^2} \tag{2.17}$$

In this work, the S-A turbulence model is used along with the RANS equations, in simulations in order to obtain a fully converged field to be used as the initial solution guess for the unsteady simulations in $OpenFOAM^{©}$ v2006.

2.2.3 Wall Treatment

The near wall-region is characterized of steep velocity gradients and intense turbulence. The proper computation of the velocity profile and the turbulent variables in this area, is crucial for the accuracy of the numerical solution. A very fine mesh has to be employed placing the first cell center to a small distance of the wall ($y^+ \sim 1$), the so-called *Low-Reynolds number modelling*. In industrial applications, the use of such fine meshes exceed the available computational resources and such a technique is not considered.

In this work, the so-called *High-Reynolds number* modelling is used along with the Spalart-Allmaras model. The *High-Reynolds number* modelling is an alternative methodology to deal with the near-wall regions avoiding the dense meshing in this area. This method utilizes a coarser grid in the boundary layer and the so-called wall functions. The wall-functions are empirical equations employed to model the physics of the flow in the near-wall region. The wall-functions try to connect the region close to the wall with the fully developed flow region. In the *High-Reynolds number* modelling approach, the first cell center from the boundary surface should be in the logarithmic region of the boundary layer at approximately $y^+ = 40 - 100$. This approach is more applicable in industrial applications since the viscous sublayer is not numerically resolved, and thus, a much smaller cell size can be used in this area.

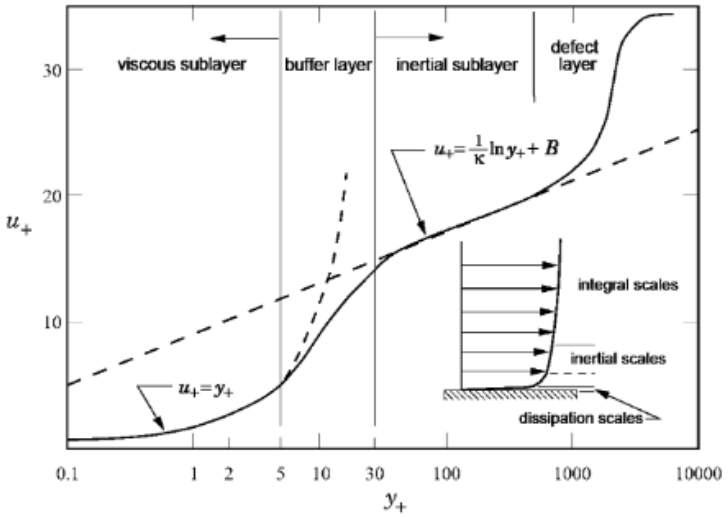

Figure 2.2: Representation of the velocity profile in the characteristic regions of the turbulent boundary layer [6].

In the S-A model, wall functions are used to approximate the value of ν_t at the cell closest to the wall. The kinematic eddy viscosity is computed according to

$$\nu_t = \frac{u_\tau^2}{\frac{\partial U}{\partial n}} - \nu \tag{2.18}$$

where n is the normal to the wall vector and ν is kinematic viscosity of fluid near to the wall. As u_τ is computed based on the y^+ value, the formulation for the computation of y^+ in $OpenFOAM^{©}$, is the so-called Spalding Law [18]. As the latter suggests, the inner sublayer region and the logarithmic region of the boundary layer are modelled with a single equation (eq. 2.19). The Spalding Law computes a continuous ν_t profile and is imposed as a boundary condition (*nutUSpaldingWallFunction*) providing a wall constraint on ν_t based on velocity.

$$y^+ = u^+ + e^{-\kappa B}\Big[e^{\kappa u^+} - 1 - \kappa u^+ - 0.5(\kappa u^+)^2 - \frac{1}{6}(\kappa u^+)^3\Big] \tag{2.19}$$

where κ is the von-Karman constant equal to 0.41 and $B \approx 5.5$.

2.2.4 Delayed Detached Eddy Simulation (DDES)

The DDES [24] is a hybrid RANS-LES model which combines the speed of the RANS and accuracy of the LES. In the DDES formulation based on the S-A model, the last term of equation 2.9, which represents the destruction of $\widetilde{\nu}$ depending on the wall distance d, is replaced by

$$\overline{d} = d - f_d\, max(0, d - C\Delta) \tag{2.20}$$

where the r_d parameter, taken from the S-A model and modified accordingly

$$f_d = 1 - tanh[(8r_d)^3] \tag{2.21}$$

$$r_d = \frac{\nu_t + \nu}{\kappa^2 d^2 \sqrt{(\frac{\partial u_i}{\partial x_j})^2}} \quad or \quad \frac{\widetilde{\nu}}{\kappa^2 d^2 S} \tag{2.22}$$

where $\overline{d}$ is the DDES model length scale, C is a calibration constant equal to 0.65 , d is the distance from the wall, Δ is the characteristic mesh size, chosen as $\Delta = max(\Delta x, \Delta y, \Delta z)$ and κ is the von-Karman constant.

By the formulation of the dissipation length scale $\overline{d}$ (eq. 2.20), the model reduces to RANS in the attached boundary layers and to LES in the detached flow regions. In this way, early transition from RANS to LES is avoided close to the wall if the mesh is not proper. In [25], was demonstrated that in a flow simulation over an

airfoil, early RANS-LES switch led to premature flow separation when setting the cell edge length inside the wall boundary layer below a critical value. In DDES, early RANS-LES transition is avoided by the introduction of f_d, which acts as a shielding function designed to be 0 in the boundary layers ($d = \overline{d}$) and 1 in the LES regions ($r_d \ll 1$). This way, the DDES length scale $\overline{d}$ detects the boundary layer and delays the switch to LES taking into account both the grid resolution and the eddy viscosity ν_t.

In this work, the DDES S-A model with wall functions is used in the transient simulations in order to obtain the flow field around the car, provided by $OpenFOAM^{©}$ v2006.

3. Rotating Wheel Modelling

In this chapter, CFD methods capable of modelling the rotation of solid bodies are discussed. Regardless the fast paced developments in the field, CFD simulations of rotating bodies mostly rely on assumptions and approximations of the real case scenario. In the case of car's wheels, the design can be that delicate combining aesthetic design, aerodynamic and structural efficiency. These co-existing goals on the wheel design can lead to a shape that requires special computational treatment in order to obtain an accurate prediction of the flow field around a rotating wheel.

In this chapter, the basics around the wheel aerodynamics will be presented and the CFD methods used in this thesis for the modelling of the rotating motion will be analysed.

3.1 Modelling Considerations

Wheel aerodynamics have become an essential aspect of the automotive industry vehicle development because they can significantly impact the overall vehicle road performance, the driving noise, the comfort, safety and most important the aesthetic result of the design.

At first, the extremely complex flow regime around a fast rotating car wheel should be approached from an aerodynamics point of view in order to understand the governing flow mechanisms. The problem of the wheel rotation modelling its not just laying on the computation of the velocity and pressure distribution on the tire and the rim of the wheel, but, in practice complexity is introduced due to additional modelling obstacles that arise, as the tires's contact patch, the static deformation, the breaking system components position behind the rim etc.

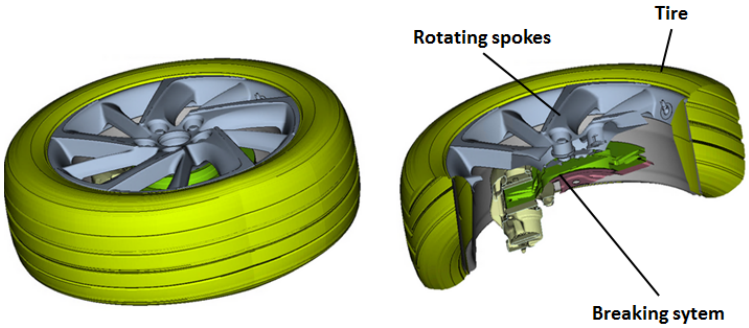

Figure 3.1: Left: Illustration of a typical car wheel. Right: Wheel cross-section.

3.1.1 Tire Contact Patch

Contact patch is the portion of a car's tire that is in contact with the road and is flat and parallel to it. It is commonly used in the cases of pneumatic tires, where the term is used strictly to describe the portion of the tire's thread that touches the road surface. The contact patch is the only connection between the road and the vehicle. The size and shape of the contact patch as well as the pressure distribution within the contact patch, are important qualities to be considered. Due to elasticity of common rubber tires the shape of the contact patch depends on the load of the vehicle body. Also, the tire shape is different from a moving tire (dynamic deformation) to a stationary one (static deformation). In most of relevant studies around wheel dynamics due to the difficulty of making observations or even determining the contact of a moving tire, the contact patch will be obtained considering the tire as stationary. But even in the scenario of a stationary car's contact patch, 3D scanner devices and 3D laser scanners are deployed in order to capture the deformed tire configuration.

Obtaining a proper representation of the wheel's contact patch is not the only thing to take into account. The contact patch ruins the axisymmetry of the tire, meaning that proper modelling has to be considered in order to model the deformed tire in this area.

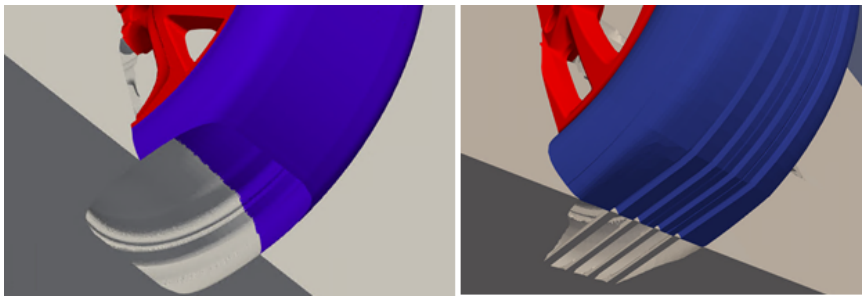

Figure 3.2: Wheel contact patch modelling in two wheels. Left: Slick tire Left: Grooved tire.

3.1.2 Dynamic and Static Deformation of Tire

The problem of the contact patch modelling brings with it the consideration regarding the static and the dynamic deformation of the tire. As said before, the tire can not be treated separately and should be modelled as part of the vehicle. Thus, the load from the car's body weight deform the tire in a stationary state, transforming it into a non-axisymmetric and non-circular-like solid body, Figure 3.3. In a dynamic state, the axial and radial deformation of the tire are also changing relatively to the rotating velocity of the wheel as the latter increases the rotational forces on the tire [30]. The contact patch cannot be obtained together with the dynamic deformation and can only be estimated. In this work, only the static deformation of the tire is taken into account.

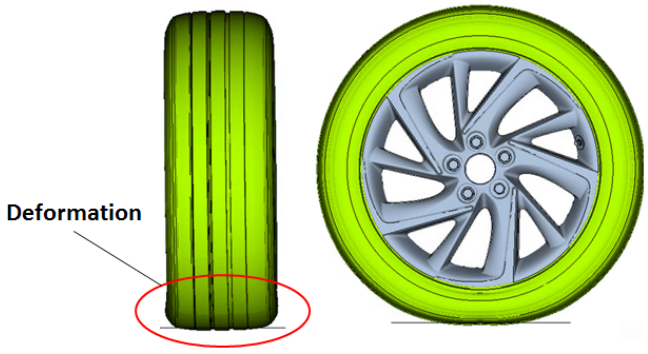

Figure 3.3: Illustration of the tire static deformation under the load of the vehicle.

3.1.3 Wheel Aerodynamics

The wheel rotation results in complex flow patterns, due to its shape, the roughness of the rubber tire, the rim shape, the grooves on the tire and the high angular velocity of a realistic automotive application. A large region of flow separation is generated behind the rotating wheel and a huge pressure drop in this area directly results in drag increase on the tire. The wheel wake is purely turbulent with strong trailing vortices governing the flow wake. The flow regime can be better understood considering the flow around a stationary and a rotating wheel, because the flow around a stationary wheel is a quite typical flow example around a body and the flow configurations are well known.

At first, for a stationary wheel, similarly to the corresponding flow around a 2D stationary cylinder, the main point of the flow de-attachment is at the top point of the wheel or cylinder, Figure 3.4. This results to the classic turbulent wake regions behind the wheel and a low pressure bubble there. In the case of the rotating wheel, this separation 'start' point is located earlier in the horizontal direction due to two factors. The first factor is the angular velocity of the wheel which gives the highest

point of the wheel a velocity vector opposite to direction of the flow. Additionally, the material roughness of the tire puts extra resistance on the flow on the tire's surface, resulting in earlier flow separation enhancing the turbulent region in the back of the wheel. This consequently results to an increase in the aerodynamic drag. With the presence of threads on the tires surface or even considering the wheel partially encapsulated inside the wheelhouse, the flow tends to be much more chaotic and turbulent than the fairly simplistic example given.

Also, the high pressure region at the front of the tire, where the streamlines firstly contact the tire, is placed in a lower point than the middle of the tire which would be in the case of a non-rotating wheel. The high pressure area with the presence of the rough road in a close distance create a very complex area for aerodynamic overview. The flow separation comes much earlier than in the case of the stationary wheel, and thus, vortices surround the wheel in all directions. These phenomena are enhanced even more by the rotation of the rim, which acts like a mixer in the flow making the flow regime at the vicinity of wheel even more chaotic.

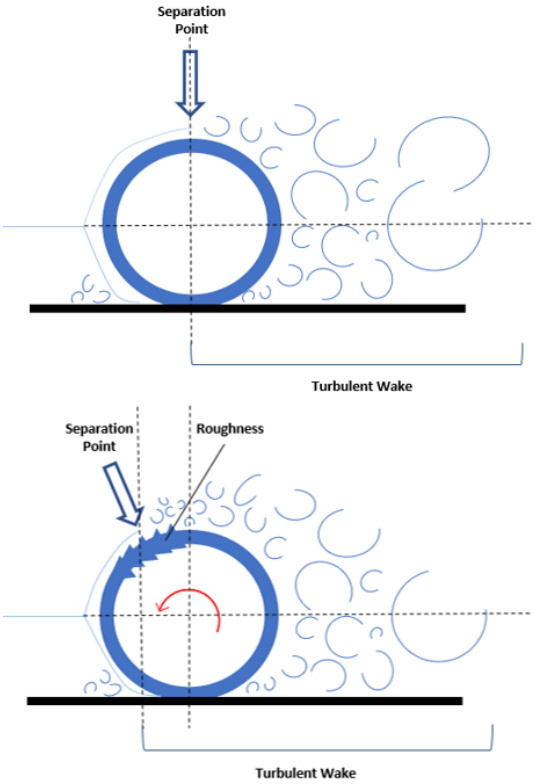

Figure 3.4: Schematic illustration of the flow separation bubbles around a spinning wheel and the separation point on its upper surface. Above: Stationary wheel. Down: Rotating wheel

3.2 Rotation Modelling Methods

In this section the main rotational motion modelling methods will be presented and analyzed. The methods are the Rotating Wall Boundary Condition (RWBC), the Multiple Reference Frame (MRF) and the Sliding Mesh (SM) as implemented in $OpenFOAM^{©}$, which is used for the simulations carried out in this thesis. Studies have been conducted comparing the MRF and the SM methodologies especially in the areas of turbomachinery and wind turbines. Comparisons between the RWBC, with the MRF and the SM method [29],[36], showed the superiority of the SM method in terms of the accurate prediction of the flow field around the wheel's rim at the cost of a steep increase in computational time.

This work, focuses on the modelling of the rotation of the wheel's rim. Each rotation modelling method will be applied to account for the rim rotation. As for the tire and rest of the wheel components, these are modelled using the RWBC only.

3.2.1 Rotating Wall Boundary Condition (RWBC)

The RWBC is the most simple way to simulate the rotating motion of a body and can be used with both steady and unsteady flow solvers. This solution does not require great effort in the implementation and the case setup neither in the meshing stage of mesh generation. RWBC is imposed, by introducing a velocity vector tangent to the wall surfaces and with magnitude equal to $\vec{\Omega} \times \vec{r}$, where $\vec{\Omega}$ is the angular velocity vector and $\vec{r}$ is the position vector with magnitude equal to the distance of the surface face centroid from the axis of rotation. To preserve the conservation of mass, the velocity vector cannot have a perpendicular component to the cell surface as this would physically introduce flow through the solid body surface violating the continuity principal. Thus, surfaces that are not parallel to the rotation will be modelled incorrectly and a wrong velocity vector will be imposed on the faces centroid, as can be seen in Figures 3.5, 3.6. The more complex the rim is the more erroneous the modelling will be.

The RWBC is useful in order to model the purely axisymmetric rotating solid parts of the wheel as long as they do not include surfaces perpendicular to the rotation. RWBC can be applied on the tire, tackling the problem of the loss of axisymmetry due to the contact patch as long as the tire is a slick one. In the contrary, complex grooved tires introduce surfaces perpendicular to the rotation direction causing these areas to be modelled erroneously with the RWBC.

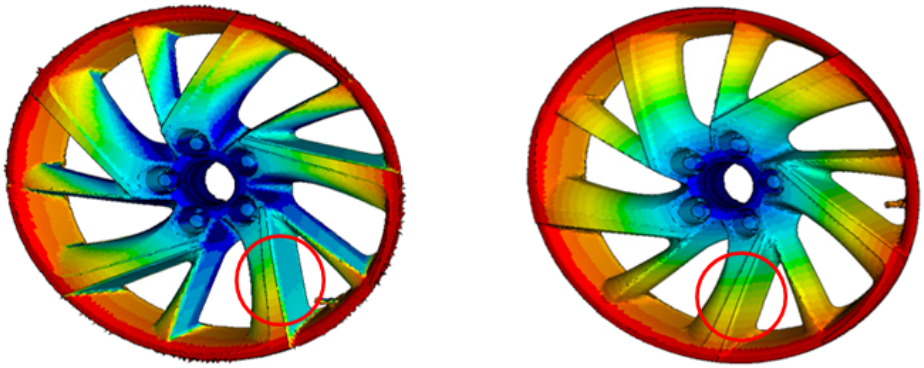

Figure 3.5: Comparison between the TV and the correct velocity distribution on the wheel spokes. Left: TV simulation. Right: correct distribution

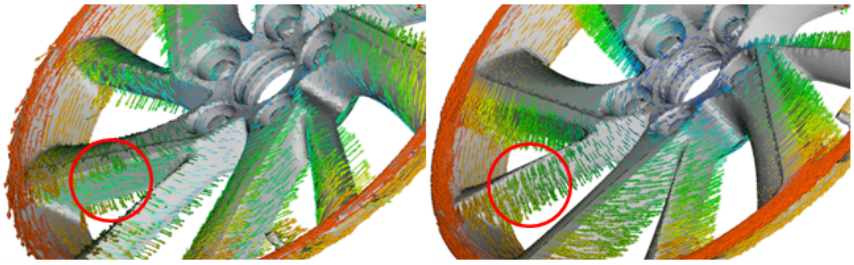

Figure 3.6: Comparison between the TV and the correct velocity vectors distribution on the wheel spokes. Left: TV simulation. Right: correct distribution

3.2.2 Multiple Frame of Reference (MRF)

The MRF method is able to overcome issues related to the use of the RWBC. The MRF simulates the rotational motion of the body with a non-rotating mesh and steady state flow solvers, by considering a separate region in the fluid domain and setting a relative rotating frame of reference w.r.t. the global reference frame. The computational domain needs to be split in two or more regions.

In the rotating region frame the steady state N-S equations are solved w.r.t. the relative reference frame and additional source terms are introduced in the momentum equations simulating the rotating motion with a non-rotating mesh.

The velocity vector expressed w.r.t. the relative reference frame is

$$\vec{u}_R = \vec{u}_A - \vec{\Omega} \times \vec{r} \tag{3.1}$$

where 'A' stands for 'absolute' and 'R' states for 'rotating' reference frame, respectively. To derive the MRF equations that are used to compute the flow field inside the relative frame, the incompressible steady state N-S equations in the inertial reference frame must be taken into account, as seen in (3.2).

$$\begin{cases} \vec{u}_A \cdot \nabla \vec{u}_A = -\nabla(p/\rho) + v\nabla \cdot \nabla(\vec{u}_A) \\ \nabla \cdot \vec{u}_A = 0 \end{cases} \tag{3.2}$$

In equations (3.2), equation (3.1) will be used as the $\vec{u}_I$ velocity term. This is going to generate extra terms involving Ω and r.

$$\begin{cases} \vec{u}_R \cdot \nabla \vec{u}_R = -\nabla(p/\rho) + v\nabla \cdot \nabla(\vec{u}_R) - 2\vec{\Omega} \times \vec{u}_R - \vec{\Omega} \times \vec{\Omega} \times \vec{r} \\ \nabla \cdot \vec{u}_R \end{cases} \tag{3.3}$$

Now the unknown is the relative velocity, $\vec{u}_R$, and the pressure. The re-formulation of the governing equations in terms of the relative velocity leads to the generation of two extra source terms in the right hand side in equations (3.3). $2\vec{\Omega} \times \vec{u}_R$ is the Coriolis term and $\vec{\Omega} \times \vec{\Omega} \times \vec{r}$ is the centrifugal term.

By using equation (3.1), the velocity $\vec{u}_A$ can be obtained. By computing the $\vec{u}_R$ inside the MRF domain, the global final solution for the velocity field can be obtained. Using equation (3.1) we can obtain the MRF relations expressed with terms of absolute velocity as,

$$\begin{cases} \vec{u}_R \cdot \nabla \vec{u}_A + \vec{\Omega} \times \vec{u}_A = -\nabla(p/\rho) + v\nabla \cdot \nabla(\vec{u}_A) \\ \nabla \cdot \vec{u}_A \end{cases} \tag{3.4}$$

The rotating body must be enclosed inside a rotating region which must be an axisymmetric volume w.r.t. the axis of rotation of the body, this interface is created in the mesh generation process. The information exchange between the stationary and the rotating region is done through the interface. As described in [31], MRF may give misleading results in the case where the inlet flow velocity direction is perpendicular to the rotating axis. This derives from the mathematics in (3.4), as it can easily be noticed that the term $\vec{\Omega} \times \vec{u}_A$ is not zero when the vector of $\vec{\Omega}$ and $\vec{u}_A$ are in a random and non-zero angle. This will produce a remaining extra pressure gradient term $\nabla p = \rho(\vec{\Omega} \times \vec{u}_A)$ which is a non-physical effect at a rotating object case. Also, test attempts rotating an empty MRF region showed that this erroneous pressure gradient term is also generated without even the presence of a solid inside the MRF domain.

In this thesis, the MRF method will be used for the rim rotation modelling and in order to provided a converged flow field for the initialization of the SM unsteady simulation.

3.2.3 Sliding Mesh (SM)

This thesis mainly focuses on the SM method, due to its accuracy a car simulation with rotating wheels can benefit from. The SM method has shown to be the most accurate and most suitable method to model the rotating rims of the wheel, as the actual mesh rotation is applied, bringing the simulation closer to the real-life scenario. The main drawbacks of the SM method application is at the first, the requirement for a high quality mesh generation, as well as, the large computational cost that demonstrates. The latter is related to the face count participating in the AMI interpolation coupling, rather than the overall mesh size. Ways to tackle the run time issue are essential for the integration of the SM in an industrial workflow.

In the SM method, the computational domain should split into two regions, the stationary and the rotating one. The rotating regions are defined in the meshing pre-processing stage of the simulation, using axisymmetric volumes to encapsulate the solid that is rotating. The boundaries of these volumes act as interfaces between the rotating and the stationary meshes. The interface has to be duplicated in two individual entities in order to be able to apply relative motion between them. On the construction and after the mesh interface rotation, a non-matching mesh region is formed locally at the interface, Figure 3.7. Data exchange must be performed through these non-matching interfaces and the quality of this information communication is what characterizes the SM method as physically reliable or not. This reliability is related to the way the flow data is transported from the one mesh region to another via the interfaces, in order for the flow data to be shared and the fluxes at the interface to be conserved. Loss of conservation on the interface is capable of leading the simulation to loss of accuracy, experience stability issues or even divergence. These issues lie mostly on the mesh generation procedure and arise in cases of discontinuities especially close to the interface.

The conservation of the flow quantities by the coupling between the stationary and the rotating mesh regions has been an extensive subject of study within the computational physics community. Methods to remove the interfaces and perform de-attachment and re-attachment [13],[15],[16] of the mesh along the interfaces have been implemented with a high increase in computational cost and are limited in applications using only structured meshes. As re-meshing is computationally demanding and as the interfaces cannot be neglected from being part of the SM method, excessive effort is invested on the improvement and optimization of the numerical coupling though the SM interfaces.

As long as more and more practical applications desire to benefit from the SM accuracy potential, the SM method is applied to complex problems where the time for

preparing a fully suitable mesh is not available. Thus, issues due to the inadequate meshing quality arise, such as the lack of a conformal mesh at the interface between the stationary and rotating mesh regions, especially in unstructured meshes, Figure 3.7. The problem of achieving conservation via the SM interfaces was first studied in [10], in 2D meshes and many similar methods followed. Non-conservative methods gained ground due to the implementation simplicity of the interpolation schemes applied to utilize the data exchange via the interfaces. A lot of work has been done in the implementation of conservatory interpolation mechanisms on the interface, such as the well know General Grid Interface (GGI) introduced in [11] using overllaping-areas weights to interpolate field values at the interface.

In this thesis, the Arbitrary Mesh Interface (AMI) method will be used, implemented in the main code of the *OpenFOAM*©.

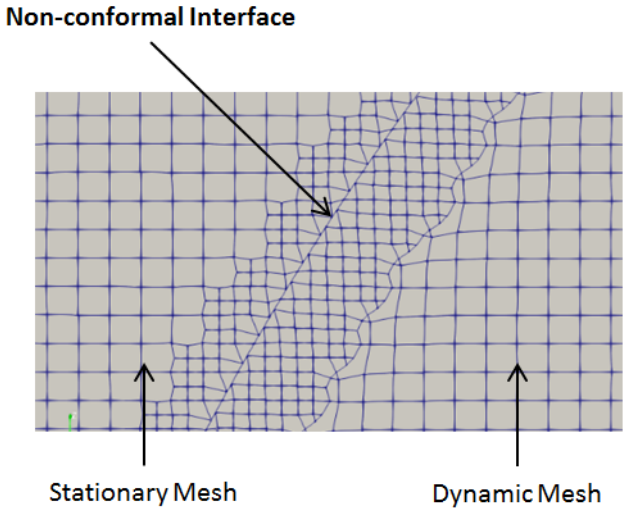

Figure 3.7: 2D representation of the non-conformal interface.

3.2.4 Arbitrary Mesh Interface (AMI)

As presented in [9], the AMI is based on the concept of a supermesh using the approach of local supermeshing to compute the fluxes at the non-conformal mesh at the interfaces and handle dissimilar meshes in 3D overlapping domains. The AMI, compared with the rest of methods, regarding fluxes conservation at the non-matching interfaces, is a highly applicable and efficient method but may introduce lack of conservativity. In order to minimize accuracy losses due to the lack of conservativity, excessive care must be taken during the mesh generation process. The more conformal the interfaces are, the lower the accuracy losses will be.

The AMI is based on the projection of the stationary and the dynamic interfaces onto an intermediate mesh, the computation of fluxes contribution from the overlapping faces and the so-called AMI interpolation to compute the fluxes at the cells surfaces. In the AMI terminology, the interfaces are called ***target*** interface (stationary) and ***source*** or ***donor*** interface (moving). For the FVM to be applied, the fluxes at the non-matching mesh must be computed. Every cell centroid is receiving contributions from two or more cells due to the overlapping faces at the interface. Consistent interpolation of a field, from the source to the target mesh, is not an option in the AMI, resulting in loss of conservativity, minimum and maximum values and issues that arise when handling discontinuous fields.

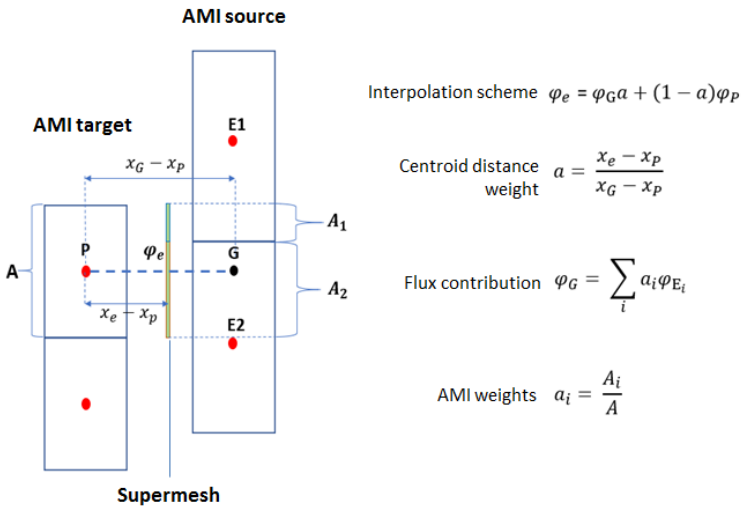

Figure 3.8: 2D representation of the AMI supermesh functionality, from [38].

In [9], a Galerkin projection method is used, in order to achieve reliable conservation between non-conformal interfaces. The Galerkin projection is a function which minimizes the L_2 norm of the interpolation error. For the Galerkin projection to work, an intermediate mesh (supermesh) between the two AMI interfaces is considered, Figure 3.8. The supermesh approach combined with the Galerkin projection is an efficient way to interpolate fields between spaces of discontinuous functions. The construction of the supermesh is carried out by an intersection-by-intersection strategy, meaning that all the intersection pairs of the elements T_S of the source interface mesh and T_T of the target interface mesh must be identified and stored. For every new position of the mesh, every element in the source and target interfaces is projected onto the intermediate supermesh. For every T_S element of the source interface, a search algorithm is employed to identify all the elements T_T of the target interface mesh that intersect with the T_S elements. Briefly, an element in T_S is chosen and the first element from the T_T mesh which intersects with the T_S element is the so-called seed element. An advancing front-like algorithm is used in order to

sequentially identify all the neighbouring elements of the seed element that intersect with the T_S element.

The mechanism of the element intersection is explained in Figure 3.9. The target interface mesh is the Cartesian grid in black, while a randomly selected source element is shown in red. At first, a seed element is detected which intersects with the red element. Next, all the neighbouring elements of the seed element are checked for intersections with the red element of the source mesh. The advancing front-like process continues by keeping all neighbouring elements intersecting with the red element.

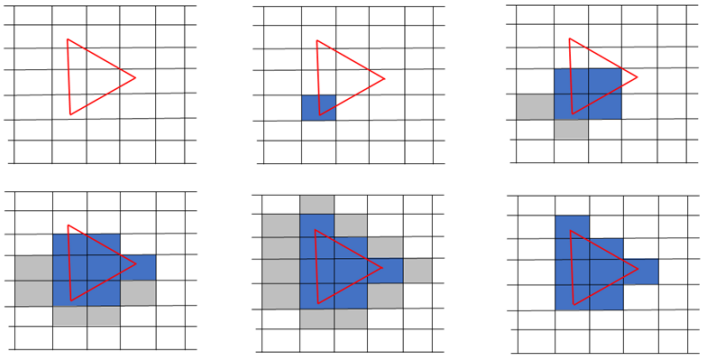

Figure 3.9: Illustration of source and target element intersection via an advancing front method. From [9]

When, at a local intersection area, all the intersecting elements are identified, a clipping algorithm is used for the intersections to be meshed, Figure 3.10. In other words the overlapping faces of the T_S and T_T interface meshes are identified. These overlapping faces give rise to an essential feature of the AMI functionality, the AMI weights.

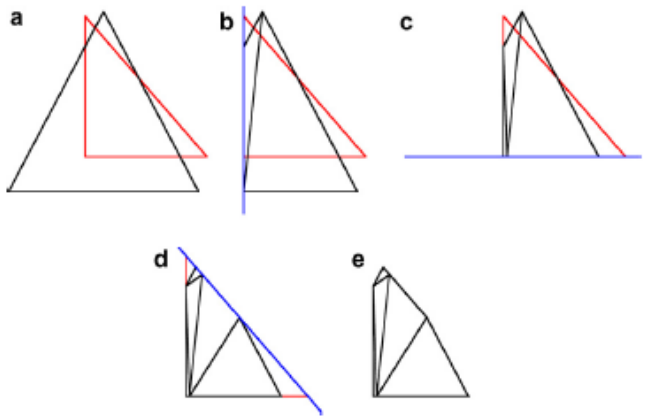

Figure 3.10: The supermesh triangulation via vertices clipping. From [9]

AMI weights

In non-conformal coupled interfaces, each face accepts contributions from partially overlapping faces from the neighbouring interface surface faces. The AMI weights define the contribution on the flux computation of each face as a fraction of the face areas of the overlapping faces. As described previously, the intersection-by-intersection algorithm is used to define the shared areas of the overlapping faces. For each face the sum of the AMI weights is normalized and should equal to 1 defining a perfect face conforming. Not well matched target and source mesh geometries result in localized conservation errors and the sum of AMI weights diverges from 1. Low meshing quality can result in the absence of a face from the target or the source interface. In this case, the sum of AMI weights of this particular face will be zero driving the method fail due to high conservation errors that are introduced.

4. CFD Mesh Generation

The process of the mesh generation is an individual science in the area of CFD and a large variety of different meshing software are available. Mesh generation is the practice of splitting the computational domain into discrete geometrical entities, known as cells of certain types depending of the mesher. In this way, a spatial discretization is provided for the domain where the PDEs can be discretized using FVM and to be solved using iterative algorithms.

Through the mesh generation stage, essential components of the CFD analysis are determined.

- The shape and the size of the computational domain are specified, defining the region where the equations are solved.
- The physical domain is discretized using geometrical elements. This is very important as different CFD solvers may require particular cell shapes and sizes to optimize their performance.
- The domain boundaries are identified and their type is specified. For an external aerodynamics analysis, it is essential to define certain parts of the domain as the inlet, the outlet the road and the rest of the surrounding walls.

4.1 SnappyHexMesh Mesh Generator

SnappyHexMesh is provided in the main *OpenFOAM*© distributions and is used for the meshing of 3D complex geometries. SnappyHexMesh is a Cartesian-prismatic unstructured mesh generation tool. The experience of its developers has shown that snappyHexMesh is not recommended for low y^+ meshes and the region between the prismatic (layering) and the Cartesian mesh is often subject to non-orthogonality issues and large cell size gaps. It generates meshes dominated by hexahedral and polyhedra cells, which is generally a good practice because of the relatively decreased cell count resulted in comparison with other techniques.

Basic requirement is to provide the mesher the surface data (triangulated surfaces) and the background mesh which is used for application of an octree-based algorithm

to divide the computational domain. SnappyHexMesh mainly splits the reference background initial mesh wrapping around the surface meshing both the bodies and the intermediate space.

4.1.1 Background Mesh

The first step of the snappyHexMesh mesh generation process, is the generation of a background mesh with hexahedral elements. This background mesh is generated by the blockMesh utility and encloses the surfaces in a box-shaped domain. For an optimal performance of the mesher, the aspect ratio of the vertices length of the background mesh must be 1. The desired cell size in which the surface is going to be discretized depends on the background mesh cell size.

4.1.2 Castellation

The second stage is the *castellation* of the background mesh, on which the octree-division is applied. The level of the base cell split is defined by the *refinement level* option in an octree-based logic as can be seen in the Figure 4.1. In this stage, surface mesh refinement is applied as also refinement regions are created in the turbulent wakes of the bodies. The most important options in the castellation stage are the *features*, *refinementSurfaces* and *refinementRegions*.

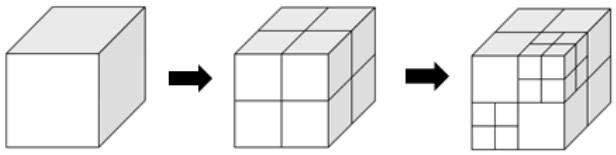

Figure 4.1: Illustration of the octree-like split of the computational domain in three stages starting from the background mesh. Each stage corresponds to a different refinement level applied.

Cell Zone - faceType

In the castellation section, the faceZone and a cellZone is assigned at the AMI region, defining an individual mesh sub-region in the domain. Later, the mesh can be split w.r.t. the AMI cellZone in order for the SM to perform mesh rotation. In this stage, in order for the snappyHexMesh to determine the cellZone and faceZone assigned to the volume of the AMI STL file, a faceType must be assigned to the internal faces of the faceZone. SnappyHexMesh can conform internal faces to an internal surface geometry such as the AMI, by the identification of the faceType parameter. In this way, the faces of the geometry turn into faceZone with a specific functionality for the mesher. This is more often met in multiphase simulation where

a faceZone is used to define the intersection of the fluid and solid region, e.g. in a conjugate heat transfer simulation, or in cases boundary faces need to be set.

In the SM method, the faceZone defined topologically by the AMI, needs to be processed according to the faceType keyword. The different faceType parameters have a huge impact on the meshing result and the AMI weights. The faceType options available are the following:

- **internal**: This option maintains the faceZone as internal faces, both for the AMI_{source} and the AMI_{target} patches.
- **baffle**: The faceType baffle option creates co-located pairs of faces from the faceZone. The baffle faceType, creates co-located pair of faces from the faceZone that share the same topological characteristics, representing the zero-thickness boundary in the mesh. This option offers the capability of creating the AMI_{source} and the AMI_{target} patches sharing the same number of faces.
- **boundary**: Similar to baffle type but creates non-co-located pairs of faces from the faceZone, representing a baffle with non-matching faces. The boundary faceType creates the two faceZones of the interface separately. Two non-identical interfaces are created, thus, in most of cases the AMI face count may be different on the AMI interfaces.
- **no faceType**: No faceType assigned.

RefinementSurfaces

The *refinementSurfaces* is the section where the refinement level applied on the surfaces is defined for the surfaces discretization. The software offers the capability of applying different refinement levels on the surface and the edges of the each surface patch, Figure 4.2. This is done by defining a min and a max refinement level for the surface.

In order to properly capture geometry's edges, snappyHexMesh needs to refine the mesh in these areas. In this way a larger number of cells are used in order to describe the edged shape.

The first way snappyHexMesh distinguishes the edges from the planar part of the surface is done based on the ***resolveFeatureAngle*** keyword which contains an angle value. The refinement is applied to the cells than can see intersections that form an angle in excess of the specified *resolveFeatureAngle* value. *resolveFeatureAngle* is a global parameter and cannot be assigned to individual patches.

Features

The second way that snappyHexMesh can identify the edges, is by means of the ***features*** utility. This utility uses the *.eMesh* files that contain data related to the defined edges of selected surface patches, where the identification of the desired edges is through the ***resolveAngle*** parameter.

The difference between *features* and the *refinementSurfaces* is that, *features* offers greater control, as the *resolveAngle* parameter is a local parameter. In this case, the user can identify certain edges on individual patches using a different *resolveFeature-Angle* value for each one of them.

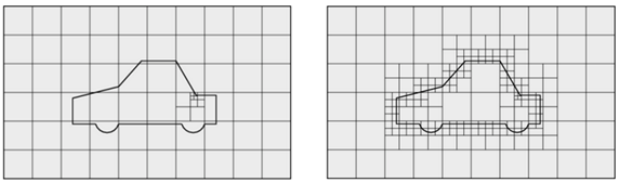

Figure 4.2: Illustration of the Castellation stage in a simplified 2D geometry. Left: The geometry placed in the background mesh. Right: The surface mesh refinement by the background mesh split.

Cell Removal

Once the mesh has been split on the features (or edges) and the surfaces of the solids, the process of cell removal begins. For the cell removal process to be successful, a point identifying the mesh domain is needed. For aerodynamic cases, this point lies in the area between the car body and the background mesh boundaries.

Refinement Regions

The last option of the castellation section is the definition of the refinement regions in the mesh, where we want to obtain a more descriptive perspective of the flow phenomena. In most cases in external aerodynamic cases, refinement regions are set at the turbulent wakes of the bodies.

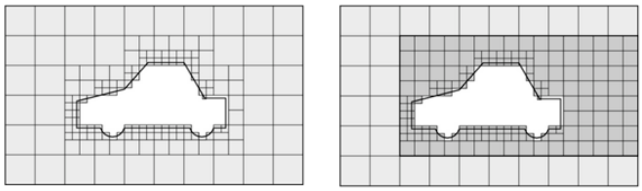

Figure 4.3: Left: 2D illustration of the cell removal stage. Right: The refinement region addition.

4.1.3 Snapping

In order for the jagged castellated surface to be removed from the mesh, in the snapping process the cell vertices are moved and adjusted onto the surfaces. In this way, the mesher captures the initial triangulated geometry and the process is controlled by specific parameter values, Figure 4.4.

In this thesis, an extensive investigation over the capability of the snapping parameters to resolve patches intersections and edges in order to capture the AMI interfaces is carried out. As long as, adequate mesh quality can be obtained at the AMI interfaces using a specific value-set of the snapping parameters, refining can be avoided reducing the mesh density on the AMI interfaces and lead to decreased simulation time.

The process is as follows:

- Displace the vertices of the jagged-castellated mesh on the boundaries onto the initial triangulated surfaces.
- Solve for relaxation of the internal mesh with the latest displaced boundary vertices.
- Identify the vertices that lead to mesh quality parameters violation.
- Reduce the displacement of those vertices and repeat the procedure from step 2, until the fulfilment of mesh quality criteria.

The snapping parameters are the following:

i) *nSmoothPatch*, is the number of patch pre-smoothing iterations before finding correspondence to surface. The recommended value for this parameter is 3-5. In this work wide range of the parameter's value will be evaluated for its impact on the AMI interfaces geometry resolution.

ii) *tolerance*, is the ratio of the distance of points to be attracted by surface feature edges or points to the maximum edge length. Setting a low *tolerance* value, the distance for points to be attracted by edges will be reduced resulting to well snapped mesh in thin gaps and narrow areas of the geometry. In this study, the possibility of high quality meshing at patches intersections will be examined which are considered as narrow areas.

iii) *nSolveIter*, is the number of the overall mesh displacement iterations. Higher values lead to better snapping result.

iv) *nRelaxIter*, is the maximum number of snapping relaxation iterations for the invalid cells to be fixed or removed. This parameter is recommended to be set in low values(100-150) for large scale meshes, because it increases the total meshing time.

v) *nFeatureSnapIter*, defines number of feature edge snapping algorithm iterations. This parameter is related to the capturing of the feature edges which have been defined by the *features* utility. In this work, the resolution of the AMI interface edges, which will be assigned as feature edges, is of high interest, thus, the impact of this parameter will be examined.

vi) *implicitFeatureSnap*, this parameter offers the user the automated feature identification of certain edges not requesting from the user to manually 'feed' the mesher with the desired angle (*featureAngle*) in order for a higher refinement level to be applied on specific geometry features. The *implicitFeatureSnap* specifies the edges automatically based on the *resolveFeatureAngle* value acting as a global parameter. Snapping is not performed directly to the geometry features, but the mesh is being snapped to a representation of the surface calculated from local surface topology.

vii) *explicitFeatureSnap*, this parameter is used to snap the mesh based on the .eMesh files data where created by the *surfaceFeatureExtract* utility. This method attracts points of the mesh to the nearest supplied feature edge and has a local application.

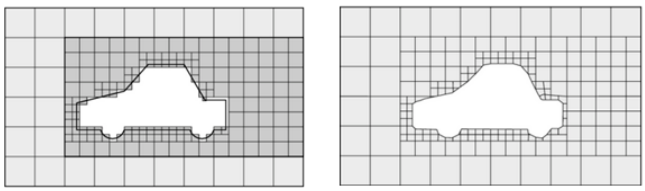

Figure 4.4: Left: The jagged castellated mesh. Right: The snapping result.

4.1.4 Viscous Layer Addition

At this point of the meshing process, the insertion of viscous layers is performed. The boundary mesh is mostly needed in the CFD analysis to capture the steep gradients close to the solid surface boundaries. The snappyHexMesh uses a mesh shrinking algorithm in order to perform layer growth on the boundary surface. The mesh close to the boundary is pushed outwards the surface based on the surface cell normal vector inserting additional prismatic cells layers. The process ensures the minimum height of the first layer, defined by the parameter *minThickness*. Mesh shrinking, may, in many areas, lead to a violation of the mesh criteria due to the bad mesh

quality close to the surface and result in a increased meshing time. To avoid such behaviour, a well snapped smooth surface should be provided by the snapping stage.

4.1.5 Mesh Quality Criteria

Due to the iterative process in which every snappyHexMesh stage is based, the quality of the mesh in every step is tested in order to fulfil specific quality criteria. These quality criteria are set w.r.t. the solvers point of view ensuring numerical stability and minimized errors during the PDEs calculation process. Upon termination of every step, the user can be informed about the mesh quality outputting certain quality criteria violation if existing. More specifically, skewness and non-orthogonality are criteria of high interest.

5. Applications

5.1 The challenge

For the SM method application, the mesher must preliminarily create an axisymmetric closed volume (cellZone) enclosing the rotating parts of the wheel, Figures 5.3, 5.4, in order to set this region as rotating based on the corresponding dynamicMeshDict file of $OpenFOAM^{©}$. The boundaries of this axisymmetric closed volume determine the so-called AMI interface on which the AMI interpolation will be carried out and the coupling between the rotating and stationary mesh will take place.

The initial attempts in the SM application using snappyHexMesh, used an AMI volume from a commercial CAD software. The latter is a high quality STL file, but it is not generated based on the snappyHexMesh surface capturing requirements. The initial AMI interface properly encloses the rotating rim of the wheel, maintaining a predefined distance from patches of the tire, the rim and the breaking system components, Figure 5.4. The use of the latter interface along with the default meshing settings of the snappyHexMesh resulted in distorted mesh on the sharp edges of the AMI and the patches intersections, generating dissimilar target and source AMIs. When these overlap drive the sum of AMI weights to diverge from one, Figure 5.1. Thus, an investigation of the proper meshing technique must be carried out. In this thesis, a meshing technique is investigated in order for the SM method to be applicable, balancing adequate meshing quality on the AMI interface and low simulation time.

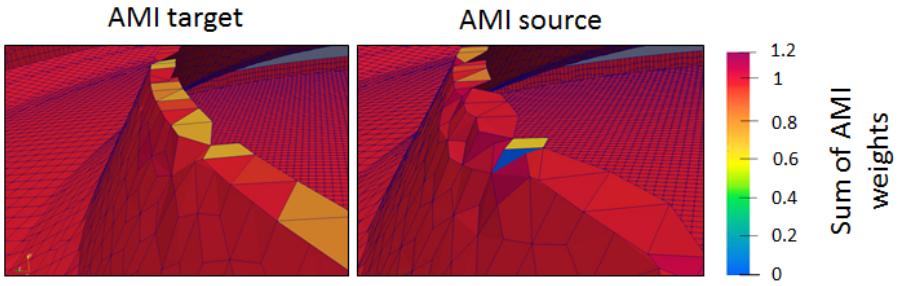

Figure 5.1: Mesh on the edge of the AMI interface and the computed sum of AMI weights in the AMI faces. Left: Sum of AMI weights for the target AMI interface. Right: Sum of AMI weights for the source AMI interface.

The areas of investigations regarding the meshing technique include:

- **snappyHexMesh parameters**: Every parameter is evaluated based on its impact on the resolution of the AMI interface's edges. The evaluation and the choice of every individual parameter will lead to a final set up of the mesher. A proper set of the parameters can lead to well resolved edges at the interface without the need of extra refinement in order to capture them keeping in the same time the AMI face count low as possible.

- **AMI shape and position**: Because of its shape based on the maintenance of a constant distance from the patches, the initial AMI interface, resulted in many intense edges and steep angles between the AMI interface surface and the other wheel components intersections. Mesh quality at these intersections and the edge capturing must be ensured in order to lead to an adequate geometry resolution of the AMI interface. As the AMI encloses the rotating part, it intersects other parts of the wheel, Figure 5.4. The meshing quality of this intersection proved to be an extremely challenging area and showed important impact on the average sum of AMI weights performance.

- **AMI face density**: The AMI face count effects in a great level the simulation time, as 30-50% of the total time of the unsteady solution is consumed by the rotating mesh operation. To tackle this, the total faces on the AMI must remain low in number as possible. A dense AMI interface can drive full car simulations to infeasible run times for an industrial environment.

5.2 Stand-Alone Wheel

A single wheel will be used in order to investigate the different options the snappyHexMesh parameters offers, as also the variety of potential shapes and geometries of the AMI interface. Every change on the parameters and the geometry is being monitored computing the average sum of AMI weights as an characteristic KPI to rate the mesh quality on the interface. The average sum of AMI weights is calculated by the averaging of all the sums of AMI weights of all faces on the interface. The objective of the investigation is to determine a robust meshing technique in order to achieve average sum of weights close to 1.

The meshing technique was applied to six different tire and rim designs in order to test its applicability and its robustness to be ensured. In order for the AMI interface to be applied to a realistic car model, all the essential breaking system components are placed behind the spokes, Figure 5.4. The position of the breaking system components is not standard in every full model CAD assembly, thus, a generic strategy for the AMI shape and position is required.

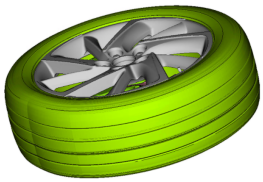

Figure 5.2: Wheel CAD model. Green: tire patch. Gray: rim patch.

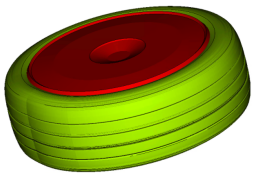

Figure 5.3: The AMI interface(red) enclosing the rim.

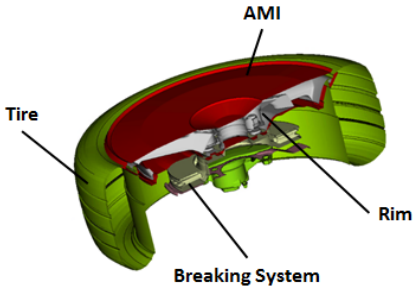

Figure 5.4: Cross section of the wheel and the AMI.

5.2.1 Meshing Parameters Investigation

In order to evaluate each different parameter's impact on the average sum of AMI weights performance, an AMI interface was generated using the default snappyHexMesh parameters with a zero-experience approach to the meshers functionality. The AMI shape is at first simplified introducing only the essential edges in order for it to be adjusted and the AMI geometry was kept constant during the parameters value investigation. Also, extra refinement is being applied at the sharp edges of the AMI in order to properly resolve them. The wheel was placed in a background mesh, Figure 5.5, that was generated by the *blockMesh* OpenFOAM utility. The size and the position of the background mesh are used in the CFD analysis of the rotating standalone wheel that will follow.

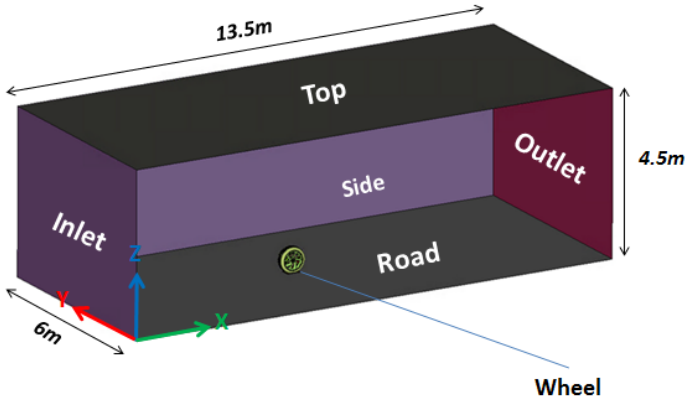

Figure 5.5: The dimensions of the background mesh used for the standalone rotating wheel simulation.

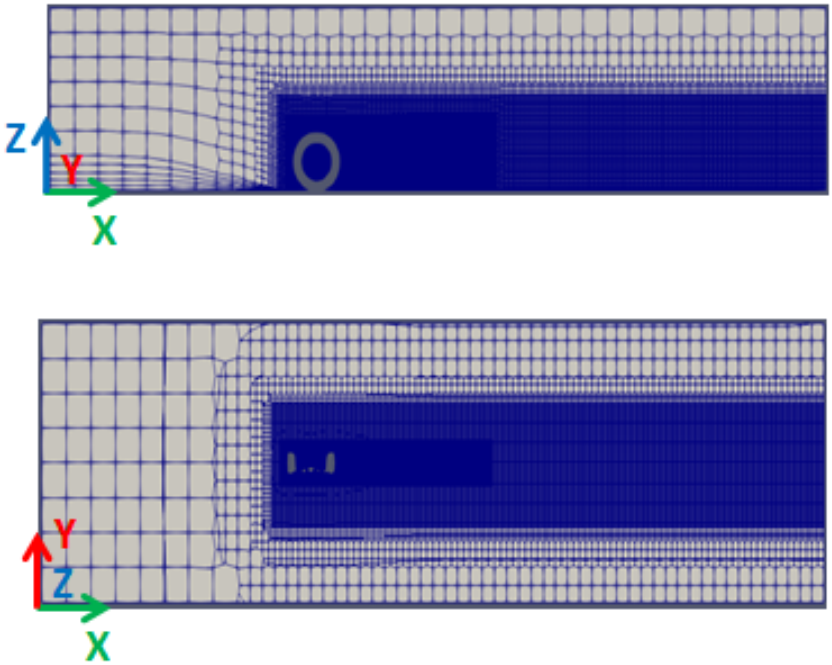

Figure 5.6: Computational mesh for the standalone rotating wheel simulation. Up: domain cross-section on the ZX plane. Down: domain cross-section on the YX plane.

The investigation is carried out by comparing each parameter individually and advancing to the next by keeping the best parameter from the previous investigation. The way to present the impact of each parameter is to compute and plot the average sum of AMI weights in each time step for time equal to the duration of a full wheel revolution. These kind of graphs offer enough information about the quality of the AMI interface, but visual inspection of the meshed interface is also mandatory. Fluctuations of the average sum of AMI weights from their average value mean that the interfaces are not adequately meshed. If the cell size and shape across the AMI

surface is uniform then, when the AMI_{target} is sliding on the AMI_{source} patch, we expect to have a stable performance of the AMI weights along an interface revolution.

faceType Parameter

The impact of the faceType can be seen from the Figure 5.7. The co-located or non-co-located faceZones produce different result effecting the coupling of the interfaces in terms of the average sum of AMI weights. Each different faceType, create different cell size and distribution on the interface causing losses in the AMI face matching. Not all the faceType options are present in the graph due to their inability to produce an AMI interface.

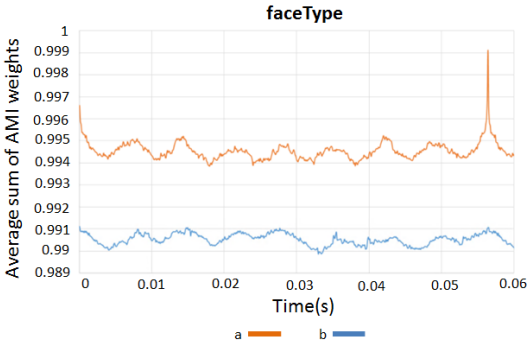

Figure 5.7: Comparative graph of the average sum of AMI weights for a full wheel revolution for two faceType parameter options.

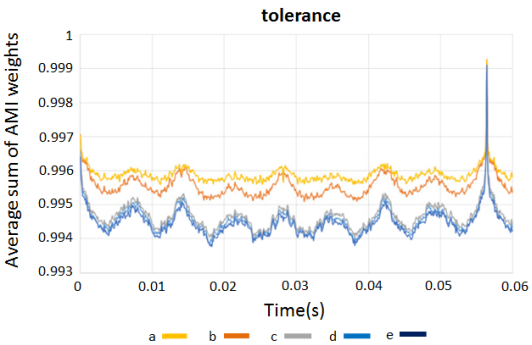

Figure 5.8: Comparative graph of the average sum of AMI weights for different value of the tolerance parameter value.

tolerance Parameter

In Figure 5.8, the impact of the *tolerance* parameter on the average sum of AMI weights is presented. The tolerance parameter value was set as low as possible, in order to determine a small distance between the AMI surface and the mesh vertices that were about to be attracted by the AMI patch. In this way, the intersections are the most benefited areas makes this parameter. Low tolerance values in narrow areas makes snapping avoid attracting mesh vertices that are in a relatively bigger distance, which may result in a distorted mesh at the AMI.

nSolveIter Parameter

In Figure 5.9, the impact of the nSolveIter parameter is introduced. The nSolveIter parameter does not show great impact in the AMI weighting in all the four different values applied. These values have noticeable differences in terms of average sum of AMI weights. It was found that high values of this parameter do not lead to better

snapping on the AMI and increase the overall meshing time. Thus, relatively low values were set to obtain the same snapping at a smaller cost.

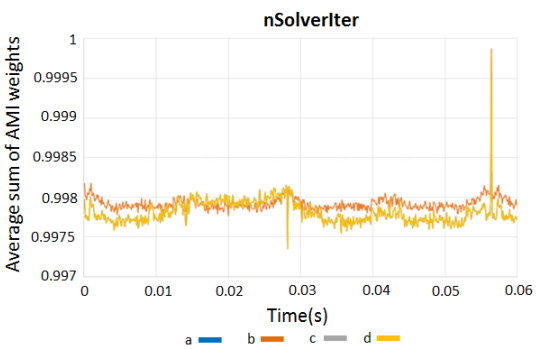

Figure 5.9: Comparative graph of the average sum of AMI weights for different value of the nSolveIter parameter value.

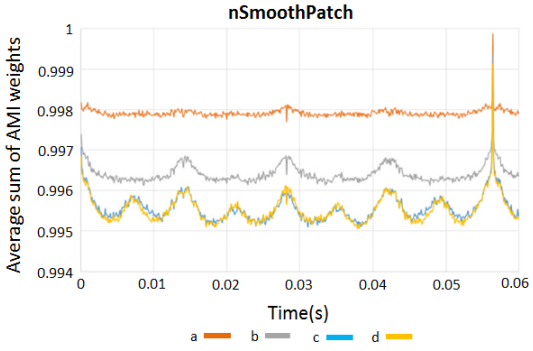

Figure 5.10: Comparative graph of the average sum of AMI weights for different value of the nSmoothPatch parameter value.

nSmoothPatch Parameter

The nSmoothPatch parameter defines the number of smoothing iterations along the surface, and has proven to be extremely effective, Figure 5.10. It was found that, low values of this parameter lead to better AMI resolution. As it can be seen, the *a* parameter shows increased AMI weighting with a more stable average sum of AMI weights performance along a full revolution.

nRelaxIter Parameter

This is one of the main parameters that increase the overall meshing time. The value of the *nRelaxIter* parameter has small impact on the improvement on the average sum of AMI weights, Figure 5.11. Thus, a relatively low value of the parameter was applied.

nFeatureSnapIter Parameter

The *nFeatureSnapIter* shows to have adequate impact on the average sum of AMI weights, as it preserves the defined features edges of the AMI, Figure 5.12. The range of values of the nFeatureSnapIter parameter applied did not show large improvement over the average sum of AMI weights, and low values of the parameter was used in order to avoid higher meshing times.

Feature snap Method

The choice of the method from which the mesher will determine the edges of the surface patches is of great important as it has a huge impact on the performance of

the average sum of AMI weights and the meshing quality on the interface, Figure 5.13.

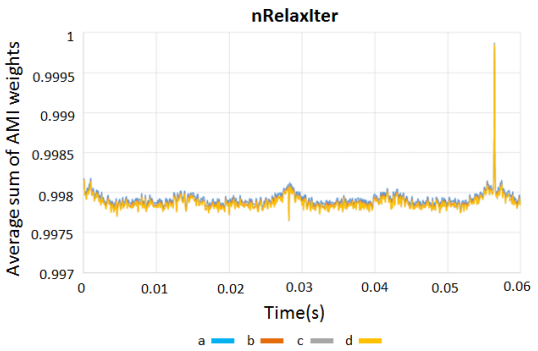

Figure 5.11: Comparative graph of the average sum of AMI weights for different value of the nRelaxIter parameter value.

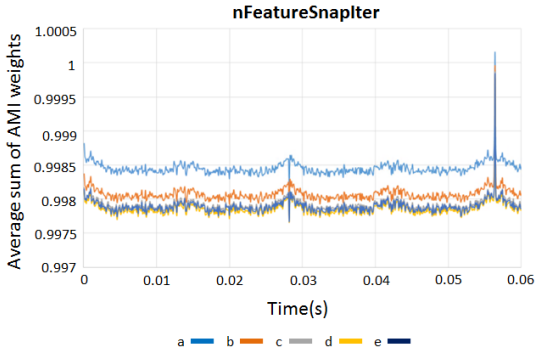

Figure 5.12: Comparative graph of the average sum of AMI weights for different value of the nFeatureSnapIter parameter value.

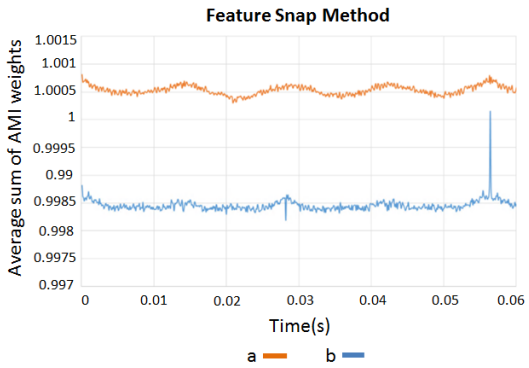

Figure 5.13: Comparative graph of the average sum of AMI weights for different feature snap methods.

In Figure 5.14, the overall impact of the snappyHexMesh parameters is plotted in terms of the average sum of AMI weighting. In Figures 5.15a, 5.15b, 5.15c, a visual inspection of the impact of the meshing parameters on characteristic AMI-patches intersections between the initial meshing parameters and the final set.

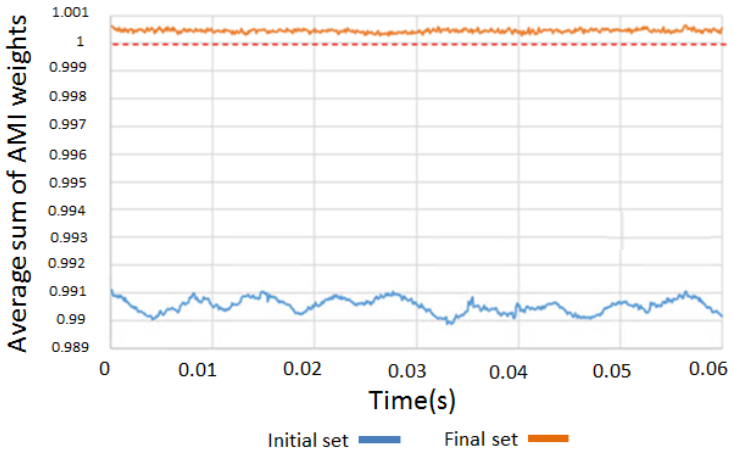

Figure 5.14: Total improvement over the average sum of AMI weighting by the application of the final set of the snappyHexMesh parameters.

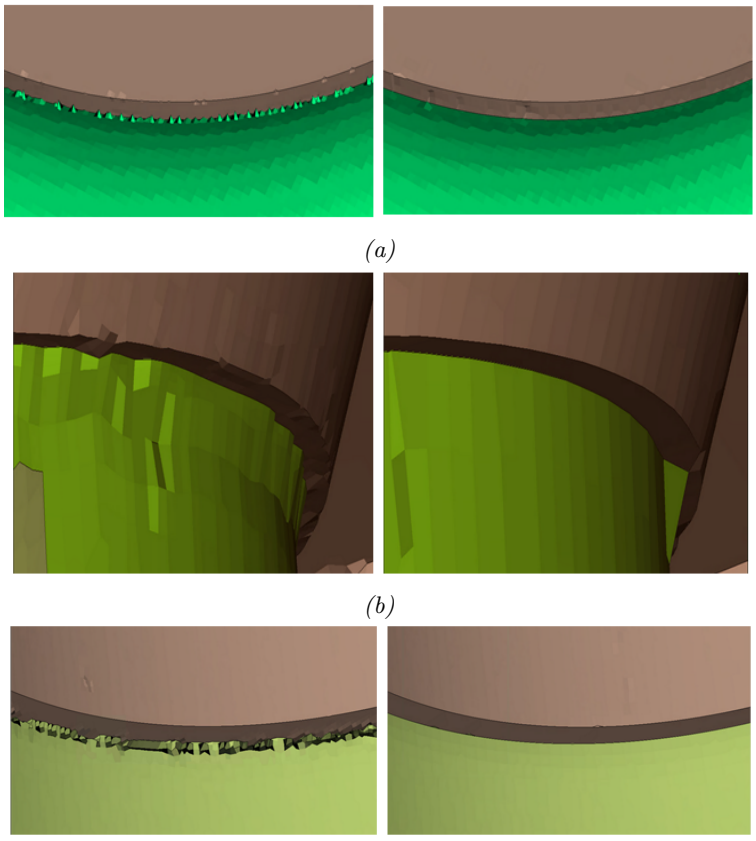

(a)

(b)

(c)

Figure 5.15: Three main intersections of the AMI interface(with gray) with wheel components. Left: Initial set of meshing parameters. Right: Optimal set up.

5.2.2 Patches Intersection Treatment

The full CAD model of the wheel along with the breaking system components, introduce mainly three patch intersections between the AMI interface and the other components. For the mesher, the intersection between patches define a complex problem of performing high quality snapping on surfaces which share edges.

The AMI interface must intersect the patches in a way to preserve the intersection meshing quality. For such meshing conditions, the snappyHexMesh offers integrated tools or the option of refining the narrow regions to capture the intersections. In order to keep the face density of the AMI interface as low as possible, another meshing technique is needed.

In this work, the snappyHexMesh background mesh is generated aligned w.r.t. the global coordinate system, Figure 5.16. During the castellation stage the background mesh is being split into hexahedral elements with equal edge length, before the generation of more complex cell types when meeting the boundary surfaces. SnappyHexMesh shows difficulty fitting cells in narrow gaps like the AMI-patches intersections and sharp edges resulting in bad snapping on them. In order for the patches intersections to be resolved, the quality of the hexahedral elements must be preserved. Thus, the orientation of the surfaces at the intersections and the edges must be as aligned as possible with the global coordinates system to assist the mesher to preserve the hexahedral element quality.

The geometrical modification that accompanied the meshing parameters investigation, in order to optimally capture the patches intersections are presented as follows:

i) **Initial**: The *Initial* is the AMI design exported by the CAD software. The way the CAD software chose how the AMI patch would intersect the other wheel components wasn't based on a average sum of AMI weights preservation, but in the maintenance of a constant distance of the AMI from the rest of the patches, resulting to an arbitrary angle between the patches surfaces. In Figure 5.17, the average sum of AMI weights along a full wheel rotation can be seen. In this case, fluctuating values of the average sum of AMI weights is the result of the low meshing quality on the edges of the AMI.

ii) **One Inclined**: The *One Inclined* intersection shows the geometrical relation of the patches that intersect. One of the patch surface at the intersection was modified such that the generated hexahedral elements were mostly aligned with the global coordinates system, resulting in a better resolved intersection and edges. In this way, the improvement in the average sum of AMI weights was

critical, bringing these close to one, Figure 5.17. Still the average sum of AMI weights experience a fluctuating behaviour showing the low mesh quality on the intersection and how the intersection still impacts the AMI weights.

iii) **None inclined**: The *None inclined* intersection type, introduces no steep or large angles between the patches. The patches surface orientation at the intersection is mostly aligned with the global coordinates system as possible. In this way, the hexahedral elements are assisted to perfectly fit at the intersection resulting to a high quality mesh. This results in a less fluctuating behaviour of the average sum of AMI weights than the *One Inclined* intersection type, Figure 5.17.

iv) **None inclined - No extra refinement**: The *None inclined - No extra refinement* intersection type, is a combination of the previous *None inclined* intersection with no extra refinement on the sharp AMI edges. The preservation of the hexahedral elements at the intersection allowed to resolve the intersection without higher refinement applied at the area. This resulted in better AMI weighting, Figure 5.17, due to the uniform cell size distribution at the AMI, so, AMI interpolation was performed between faces with the same area leading to improved matching. In previous intersection types, refinement was applied to capture the AMI-patches intersections and thus, AMI interpolation was performed between faces with dissimilar areas leading to losses in face matching.

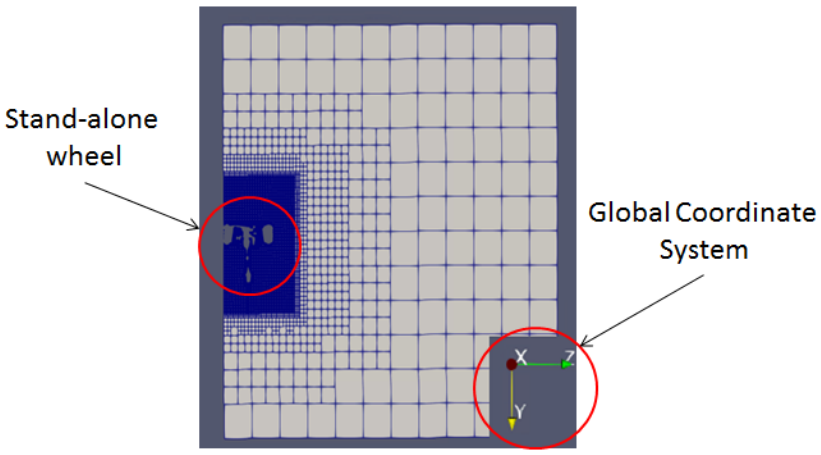

Figure 5.16: The CFD mesh cross-section of the standalone wheel case.

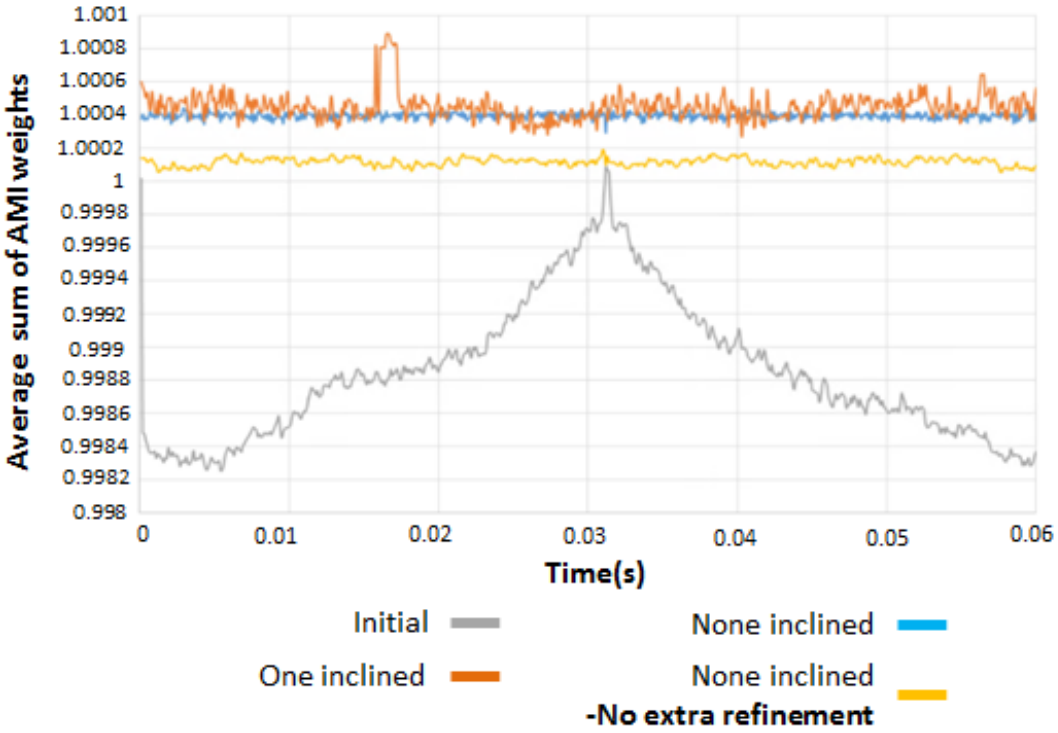

Figure 5.17: The average sum of AMI weights for the four intersection types.

5.2.3 Stand-Alone Wheel simulations

In this section, single rotating wheel simulations are carried out using different AMI interfaces. The objective is to demonstrate and evaluate the impact of each different AMI on the $C_D * A$ value, the simulation time and the computed flow field around the wheel. The best meshing practice found during the previous investigation was applied for a fair comparison. The quality of the AMI interface from a weight-wise point of view, can cause an impact on the flow field and the aerodynamic drag coefficient. The quantification of this impact is useful to understand if the meshing effort invested on the determination of the 'high quality' AMI interface is useful and applicable in full vehicle simulations. As there are no experimental data from measurements of flow around single rotating wheel, the comparison was conducted sideways.

The wheel geometry consists mainly from the tire, the spokes, the breaking system components and the AMI interface enclosing the rotating parts, Figure 5.4. Four different CFD analysis are carried out with four different AMI interfaces. The CFD results with be presented in two planes around the wheel.

The wheel radius is $R = 0.3358$m, the inlet velocity is $U = 27.78\frac{m}{s}$ and the Reynolds number is equal to $12.44 \cdot 10^5$

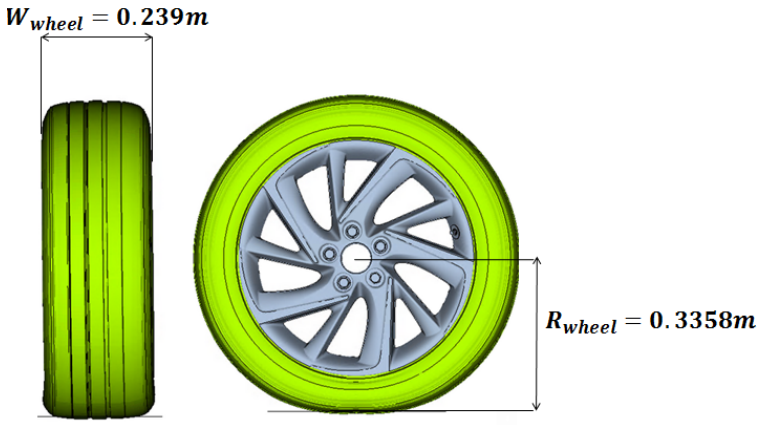

Figure 5.18: Wheel geometry

The AMI interface variants

From the meshing process, four AMI interfaces were created and a comparison was made:

i) **Initial**: The *Initial* AMI was generated without using the geometry and meshing parameters proposed by the parametric investigation. The default meshing parameters are applied with no geometry modification in the initial AMI CAD data generation.

ii) **Coarse$_1$** : This interface was generated applying the meshing parameters and AMI geometry that were proposed by the investigation, but a lower refinement level was applied on the AMI surface in order to reduce the AMI face count.

iii) **Coarse$_2$ - best practice**: The *Coarse$_2$* is the result of the best meshing practice application identified by the latter parametric investigation, Figure 5.17.

iv) **Fine**: The Fine AMI interface was generated applying the meshing parameters and the AMI geometry that were proposed, but extra refinement was used at the AMI intersection and sharp edges resulting to a dense AMI.

The AMI face count for each one of the AMI interfaces can be seen in Figure 5.20.

CFD Mesh

The computational domain generated by the snappyHexMesh, Figure 5.6, is rectangular with 13.5m upstream length, 4.5m high and 6m inlet and outlet width, Figure 5.5. The wheel's contact patch is created by the intersections of the 'road' patch of the computational domain with the tire, Figure 3.2. Four refinement volumes have been created surrounding the wheel in order to accurately predict the flow field while keeping the number of the cells low, avoiding the refinement of the whole domain.

The meshes for the four different AMI cases consisted of $7.5 \cdot 10^6$ cells, with $12 \cdot 10^3$ surface cells. Approximately $7 \cdot 10^6$ of them were hexahedral elements, $3 \cdot 10^5$ polyhedral, $3.5 \cdot 10^4$ prisms, and less than 100 are tetrahedra. The mesh included prism layer mesh of 3 layers on all surfaces.

CFD Boundary Conditions

The boundary conditions for the pressure and the velocity are presented in the table 5.1.

Boundary Conditions		
Boundary Patch	**Velocity**	**Pressure**
Inlet	Dirichlet U = (27.78 0 0) m/s	zero Gradient
Outlet	inletOutlet	zero Dirichlet
Sides	symmetry	Symmetry
Road	movingWallVelocity (28.78 0 0)	zero Gradient
Top	symmetry	Symmetry
Tire	rotatingWallVelocity	zero Gradient
Spokes	movingWallVelocity	zero Gradient
AMI patches	cyclicAMI	cyclicAMI

Table 5.1: Boundary Condition for the stand alone wheel CFD analysis

5.2.4 CFD Results

The CFD simulation consisted of two parts.

1. Steady state MRF simulation (solution initialization)

At first, a steady state MRF simulation (non-rotating mesh) utilizing the S-A high-Re turbulence model was carried out in order to supply the unsteady simulation with a fully converged flow field as the solution initialization. To achieve convergence of the flow variables 7000 solver iterations of the **SIMPLE** algorithm [39], were necessary. A second-order linear upwind scheme was used for the discretization of the convection terms and a linear limited scheme for the Laplacian terms. A linear interpolation scheme was used for the transform cell-centre flow quantities to face centres and the Green–Gauss theorem was applied for the discretization of the spatial quantities.

2. Unsteady SM simulation

The SM method was applied for the mesh rotation. A DDES S-A simulation was carried out with a time step of $dt = 1.4 \cdot 10^{-4}$ sec, and was conducted for 1 sec of physical time. The unsteady flow data were obtained using the **PIMPLE** solver with mesh motion, [40]. For the time derivative discretization, a second-order backward scheme was appplied. A second-order linear upwind scheme was used for the discretization of the convection terms, a linear scheme for the quantities interpolation and a linear limited scheme for the Laplacian terms.

The mesh rotation was performed before the PIMPLE loop. Before the solution of the momentum equations, the mesh is rotated and its addressing is updated for time $t = t + \Delta t$. At each mesh update, the AMI weighting was recomputed as the AMI target and source patches have an updated relative positioning. At this point, before solving the governing equations on the updated mesh, one must ensure that the values obtained in the previous iteration for u and p still satisfy continuity when remapped on the current mesh. A modified form of Poisson equation is solved for the pressure corrector field ***pcorr***, which gradient is used to update the velocity for the updated mesh, [35]. In rotational meshes, the computational cost increases, compared to unsteady simulations with stationary mesh, caused by the computation of the ***pcorr*** field and in the case of the AMI application, the computation of the AMI weights in every mesh position.

Averaging of the transient solution for the velocity and pressure variables was performed starting at the 0.5 sec of simulation until the end of the iterative solution (0.5 sec $\rightarrow$ 1 sec). The wheel's radius was 0.3358m, its angular velocity was 82.7 rad/s, a total of approximately 13 full revolutions of the wheel simulated.

The flow around the rotating wheel was computed with the same case set up for the four different AMI interfaces used. The average sum of AMI weights, the $C_D * A$ value, the simulation time, and the flow fields in the vicinity of the wheel were compared.

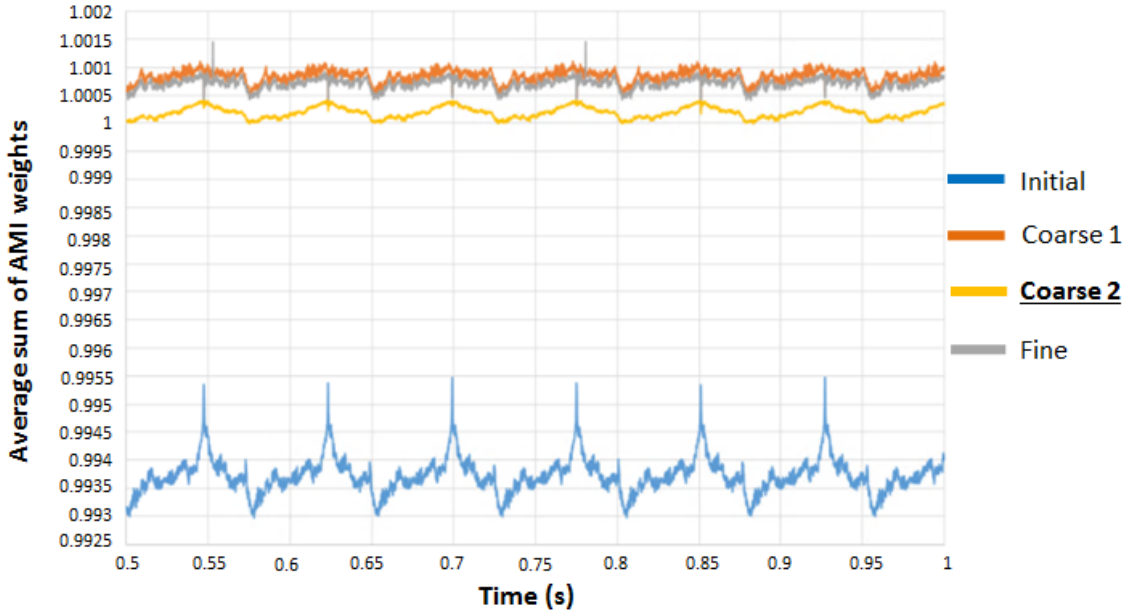

Figure 5.19: The average sum of AMI weights for the AMI interfaces along the last 0.5s of the simulation.

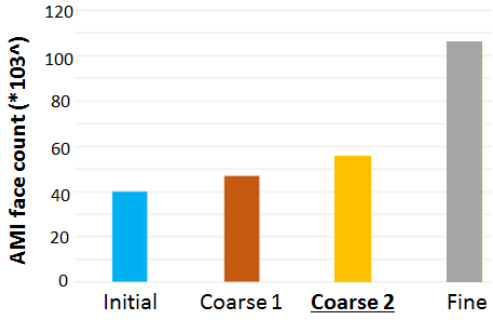

Figure 5.20: Number of AMI faces for the single rotating wheel SM cases.

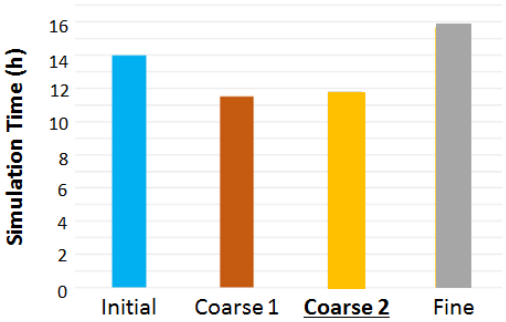

Figure 5.21: Simulation total time for the single rotating wheel SM cases.

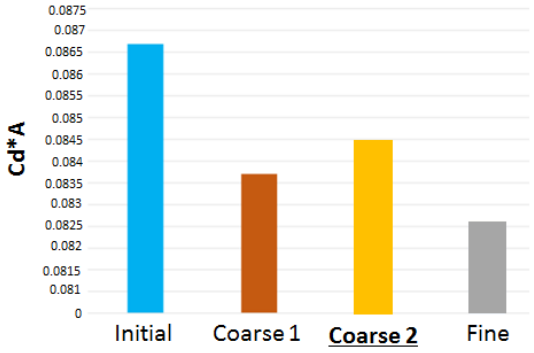

Figure 5.22: $C_D * A$ value for the four single rotating wheel SM cases.

The aerodynamic analysis results for the four cases are presented in two planes of specific dimensions in the flow field around the wheel. In Figures 5.23, 5.24, the dimensions and positions of these planes are introduced.

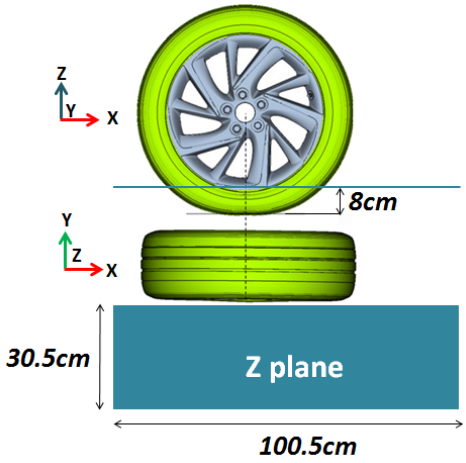

Figure 5.23: Z plane orientation.

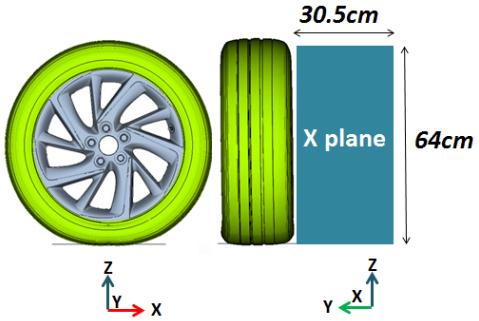

Figure 5.24: X plane orientation.

Summary of the Single Wheel Simulation Results

At first, in Figure 5.20, the $Coarse_2$ interface shows the average sum of AMI weights being closer to 1 due to the uniform face area distribution on the interface as no higher mesh refinement was applied on the AMI edges. The $Fine$ and $Coarse_1$ interfaces show worse weighting compared to the $Coarse_2$ due to the non-uniform face area distribution on the AMI as explained in section 5.2.2.

In Figures 5.20 and 5.21, the impact of the number of the AMI face count on the simulation time can be seen. In the case of $Fine$ AMI, the increase in run time due to the AMI face count, is about 25% higher from the run time obtained by the $Coarse_2$ AMI which has 50% less faces. Thus, preserving the average sum of AMI weights at a level close to 1 and keeping the AMI faces as low as possible is the desired strategy. In Figure 5.21, the relatively higher simulation time of the *Initial* AMI compared to the small AMI faces, is explained by the low mesh quality at the AMI-patches intersection for this AMI, resulting in invalid cells slowing down the solution. It is clear that, in full car simulation with four AMI regions, the run time increase may be huge compared with the standard aero methodologies. Thus, the number of the AMI faces is one of the most important KPIs to consider.

From Figure 5.22, it can be seen that the *Initial* AMI computes a different $C_D * A$ value compared to the others. This can directly be related to the AMI weights impact on the results, as can be seen in Figure 5.19. $C_D * A$ values for $Coarse_1$ and $Coarse_2$, have a smaller relative delta that is aligned with the almost same levels of the average sum of AMI weights that they share.

From the flow field data presented in Figures 5.25 - 5.32, the impact on the flow field for the different AMI interfaces for the two different planes is presented. In Figure 5.25, the almost identical distribution of the pressure coefficient for the $Coarse_2$ and $Fine$ interfaces can be seen, the same is repeated in Figure 5.29 distribution of the pressure coefficient for the Z plane. Similarities in the Z velocity component for the $Coarse_2$ and $Fine$ AMIs is noticed also in Figure 5.28. $Coarse_2$ and $Fine$ interfaces share the same flow patterns for all the flow variables that are plotted. In the contrary, $Initial$ and $Coarse_1$ interfaces compute dissimilar fields for all the variables.

In conclusion, the meshing practice proposed and applied with the $Coarse_2$ AMI interface shows better average sum of AMI weights among the others, 50% less AMI faces and 25% reduction in simulation time from the $Fine$ AMI. No great differences are noticed in $C_D * A$. Thus, the meshing practice obtained by the parametric investigation can be applied with the best-found level of average sum of AMI weights and with a relatively faster analysis time.

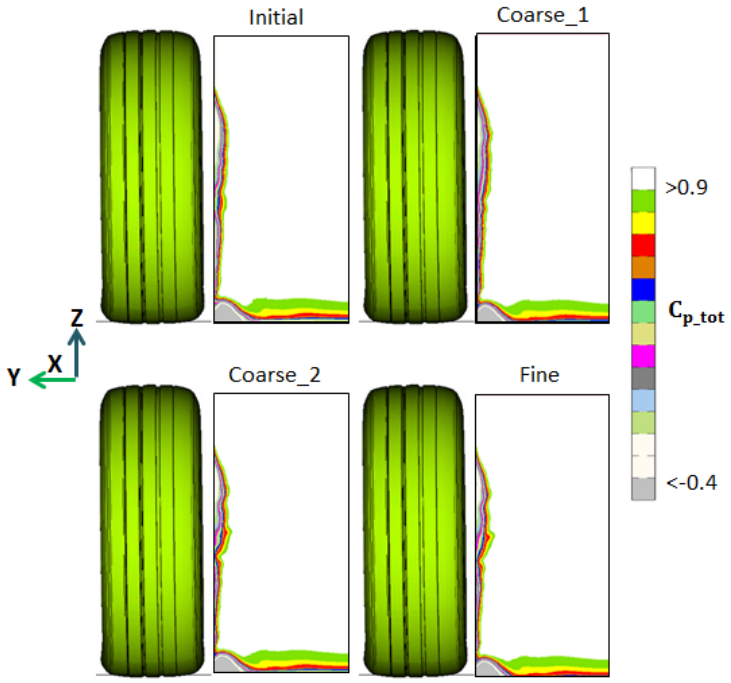

Figure 5.25: Total pressure coefficient ($C_{p,Total}$) distribution on the X plane.

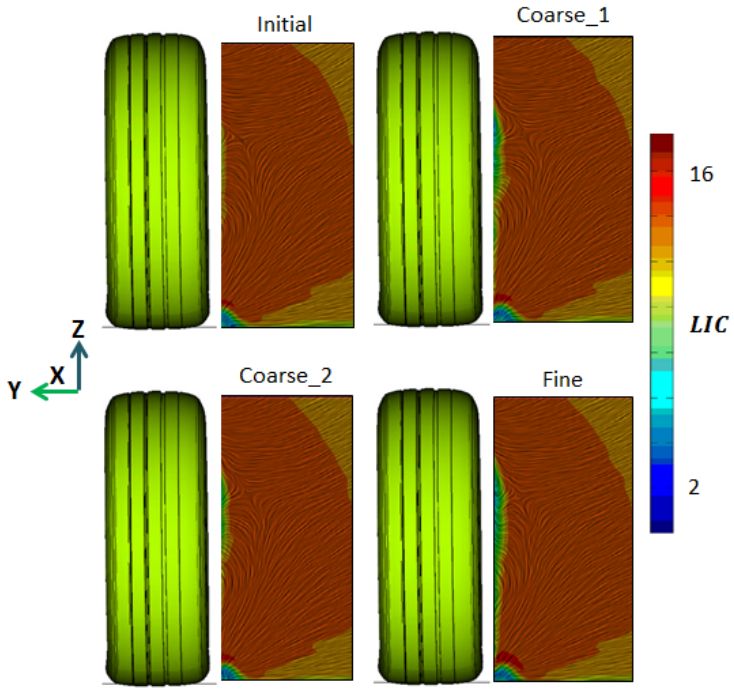

Figure 5.26: LIC of the streamlines of the flow field on X plane.

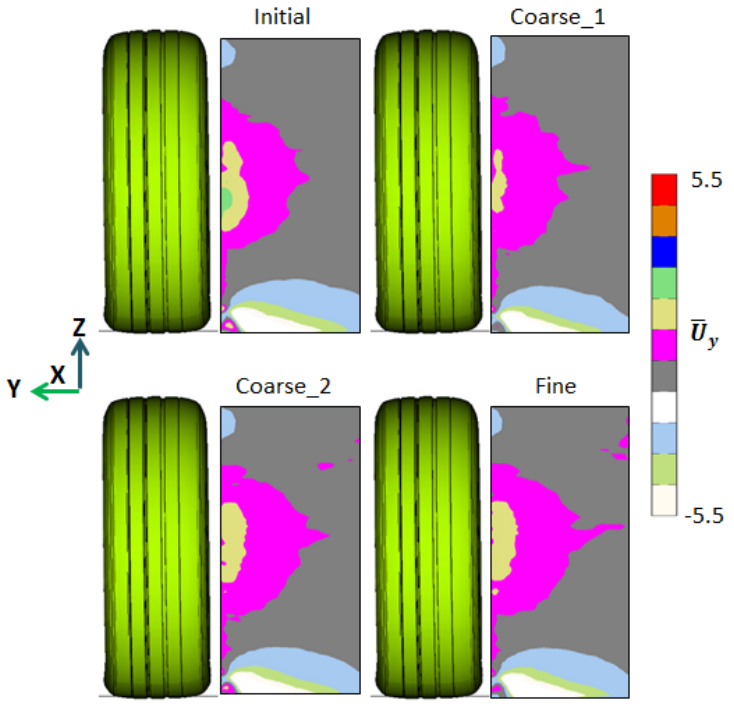

Figure 5.27: Distribution of the mean Y velocity component on the X plane.

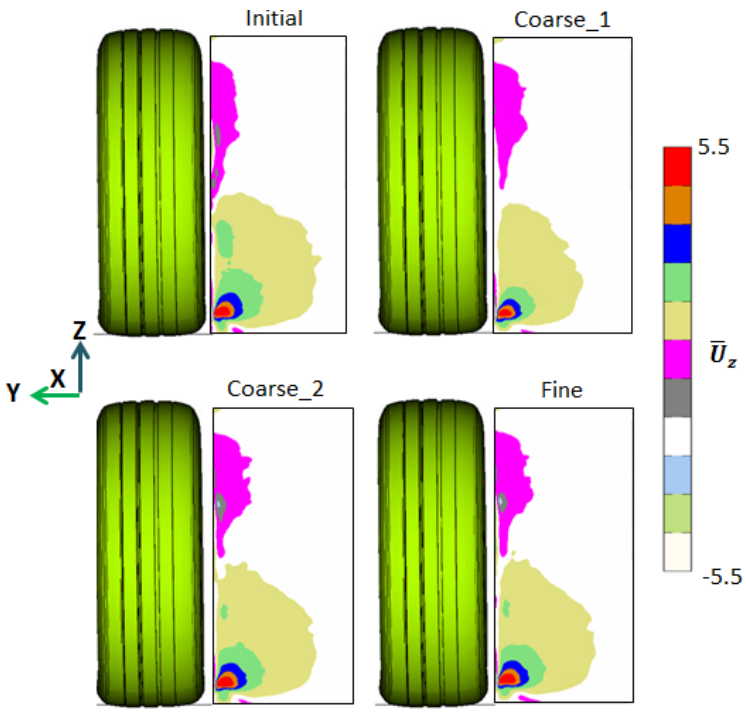

Figure 5.28: Distribution of the mean Z velocity component on the X plane.

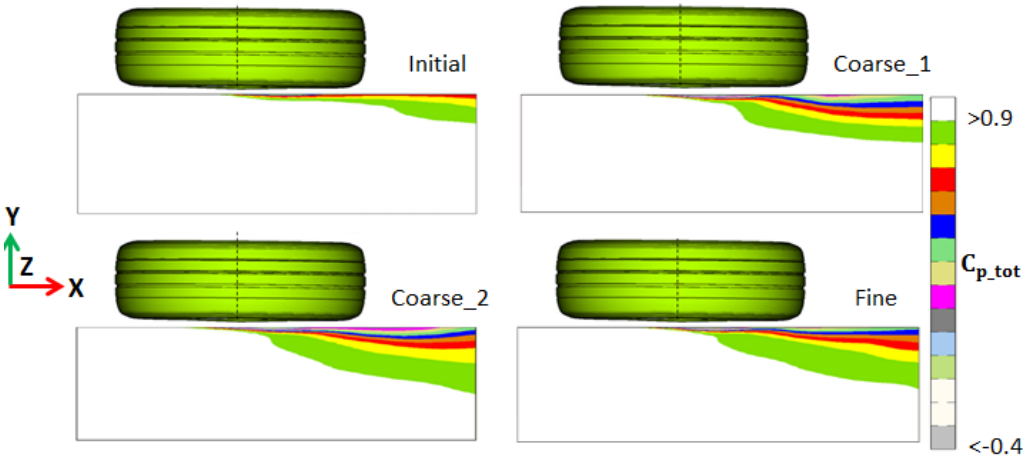

Figure 5.29: Total pressure coefficient ($C_{p,Total}$) distribution on the Z plane.

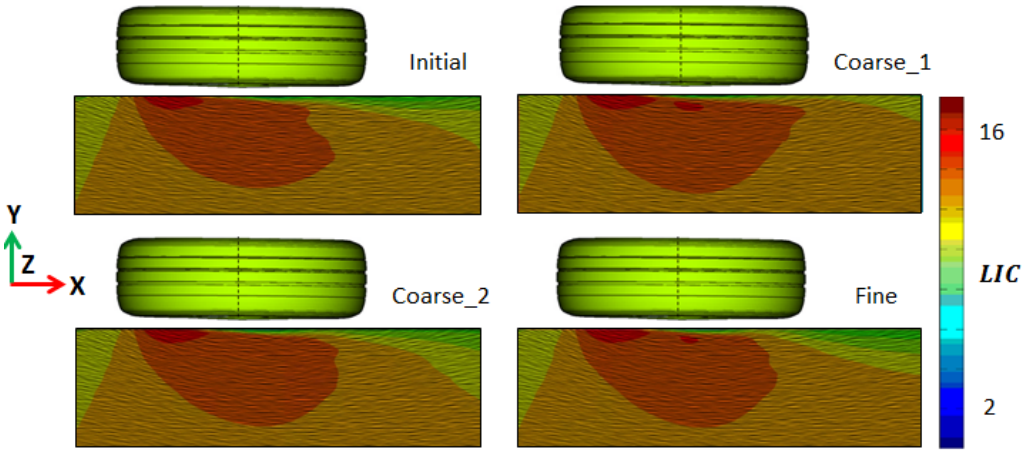

Figure 5.30: LIC of the streamlines of the flow on Z plane.

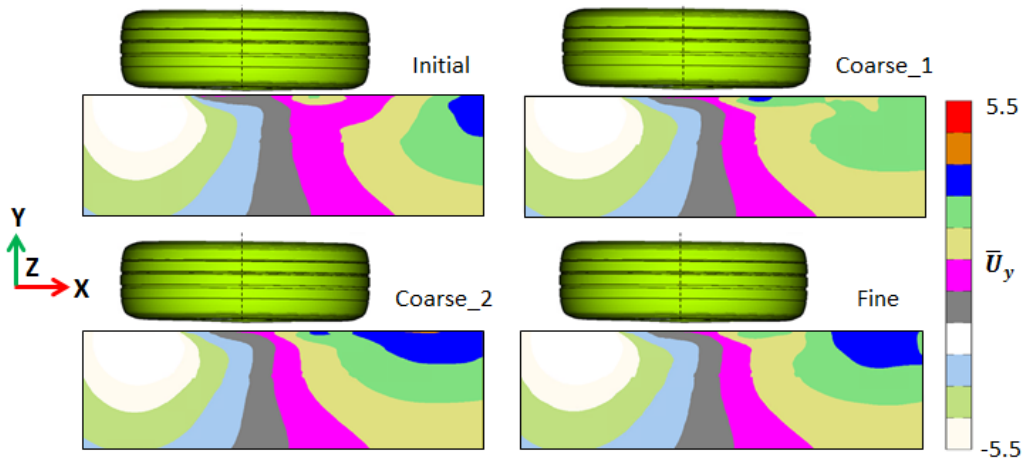

Figure 5.31: Distribution of the mean Y velocity component on the Z plane.

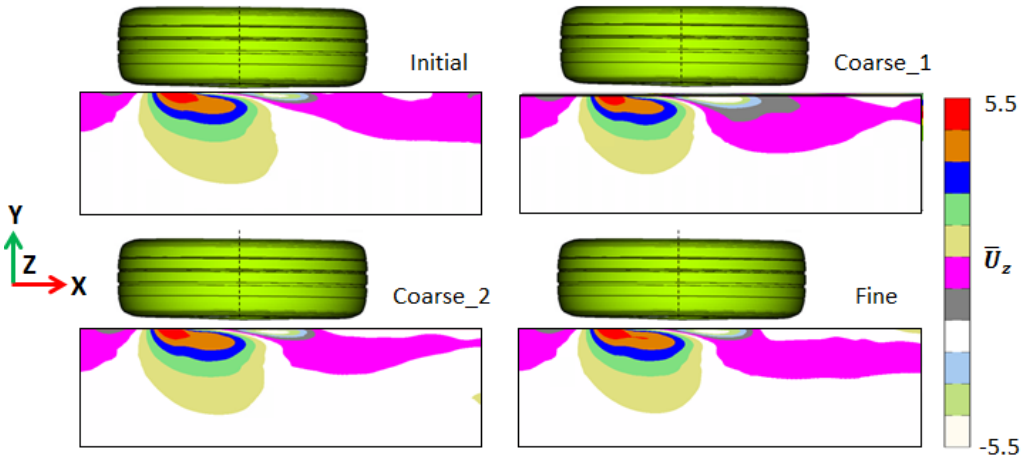

Figure 5.32: Distribution of the mean Z velocity component on the Z plane.

5.3 Application to a Production Car

In this chapter, the SM method is applied for the simulation of the flow around a production car with rotating wheels. The SM method results are compared with results obtained from simulations using the RWBC and the MRF methods for the wheel rotation modelling as well as with experimental data. The car model used is the same, except from the SM and MRF cases, where four additional STL files will be added in order to define the rotating mesh regions and operate as the AMI interfaces.

The solution field for a variety of flow variables is visualized on two planes close to the front wheels and will be compared and the corresponding experimental data. The ΔC_D values for the three different models will be obtained based on the C_D value measured in the experiment.

5.3.1 Experimental Set up

Wind tunnel measurements were conducted on the semi-anechoic S2A GIE wind tunnel in France, Paris [37]. Rolling belts under the wheels and the car were used in order to mimic the moving road, 5.33. A six-component balance was used to measure all the aerodynamic forces acting on the car body. For the pressure and velocity measurements in areas in the vicinity of the rotating wheels where there are 3D flow patterns, omnidirectional L-shaped 18hole probes are placed mounted in a 3D traversing system. Measurements of the aerodynamic quantities took place in planes shown in Figures 5.41, 5.42. Both of the planes were placed 5cm from the wheel and 8cm from the ground in order for the data collection system to be placed.

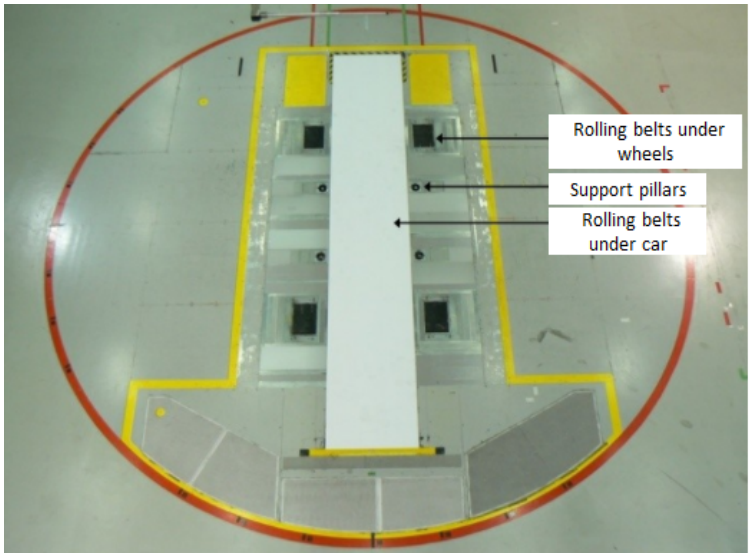

Figure 5.33: Wind tunnel rolling belts system, from [37].

5.3.2 CFD Mesh

The numerical mesh included the full car model without considering model symmetry on the flow domain. The size of the computational domain is presented in Figure 5.34. Mesh refined regions are generated in order to capture the turbulent wakes around the mirrors, the wheels, and the rear wake area of the car. The mesh consists of $100 \cdot 10^6$ cells, $90 \cdot 10^6$ hexahedral, $14 \cdot 10^6$ prismatic and about $8 \cdot 10^6$ polyhedral cells. Three viscous layers are generated on all patches in order for the boundary layer to be resolved with $y^+ \approx 30 - 100$. The tire and rim patches are meshed with $375 \cdot 10^3$ surface cells approximately.

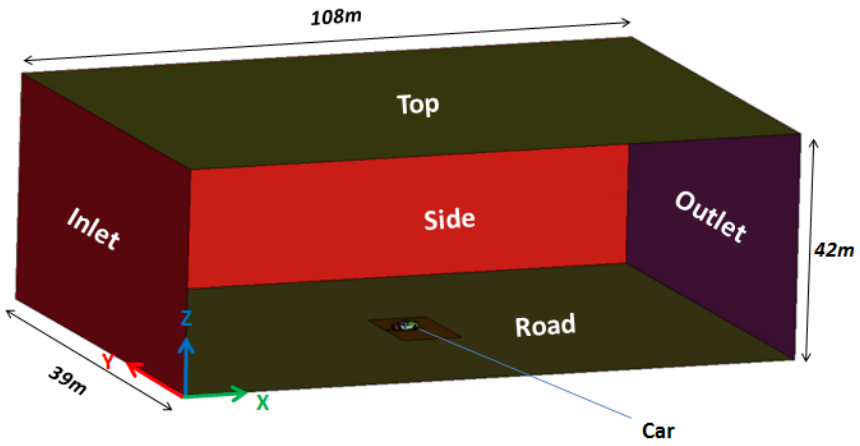

Figure 5.34: Size of the computational domain for the full car flow simulations.

5.3.3 Boundary Conditions

The boundary conditions imposed on the patches of the CFD mesh are presented in Table 5.2 for the RWBC, MRF and SM simulations. Five moving belt patches have been placed in order to simulate the moving road. Four belts under the wheels and a long one under the car body are placed, as done in the aerodynamic measurements, Figure 5.33. The rest of the road patch is modelled using slip boundary condition.

Boundary Conditions		
Boundary Patch	**Velocity**	**Pressure**
Inlet	Dirichlet U = (38.88 0 0) m/s	zero Gradient
Outlet	inletOutlet	zero Dirichlet
Sides	symmetry	Symmetry
Road	slip	zero Gradient
Belts	movingWallVelocity	zero Gradient
Top	symmetry	Symmetry
Tire	rotatingWallVelocity	zero Gradient
Spokes (for RWBC)	rotatingWallVelocity	zero Gradient
Spokes (for AMI and MRF)	movingWallVelocity	zero Gradient
AMI patches (for AMI and MRF)	cyclicAMI	cyclicAMI

Table 5.2: Boundary Condition for the car CFD analysis, for the RWBC, MRF and SM cases.

5.3.4 CFD Results

The unsteady RWBC simulation

The RWBC method was applied with an unsteady flow solver and the DDES S-A turbulence model with wall functions. The simulation was run for 3 sec of physical time with a constant time step of $\Delta t = 10^{-4}$ sec of the PIMPLE solver. Averaging of the unsteady field was performed for the last 2 sec of the simulations at the time window 1 sec $\rightarrow$ 3 sec, obtaining the mean values of the pressure and velocity fields. For the solution initialization, a fully converged flow field was computed by a RANS S-A simulation using the SIMPLE algorithm [39], running for 7000 solver iterations in total.

The MRF simulation

The MRF model steady simulation was carried out until reaching convergence of the flow variables residuals and 7000 solver iterations of the SIMPLE algorithm were necessary. The AMI interfaces used for the SM simulation were used also for the MRF simulation, so the relative reference frame to be distinguished from the global one. For turbulence modelling, a RANS S-A set up with wall functions was used.

The numerical schemes used for the discretization and solution of equations were the same as the RANS S-A standalone wheel simulations.

The SM simulation

The SM unsteady simulation with mesh rotation, was conducted using four AMI interfaces for the wheels of the car, identifying four separate rotating mesh regions. The rest of the wheel parts, namely the tire and the breaking system components, are modelled by imposing the RWBC on the boundary patches. The solution of the unsteady SM simulation was initialized using the fully converged solution provided by the latter MRF steady state analysis. The SM simulation was run for 3 sec of physical time with a constant time step of $\Delta t = 10^{-4}$ sec of the PIMPLE solver. Simillary to the RWBC simulation, averaging of the unsteady field was performed for the time window 1 sec $\rightarrow$ 3 sec. The AMI interfaces were generated using the *None-inclined* intersection type and with *Fine* meshing set up for the snappyHexMesh parameters, counting $95 \cdot 10^3$ AMI surface cells.

The numerical schemes for the discretization of the equations in time and space and the iterative solution of the equations system in the unsteady DDES S-A simulations were the same as the ones used for the standalone wheel simulations, see section 5.2.4. The Reynolds number is equal to $4.6 \cdot 10^6$.

In Figures 5.35, 5.36 and 5.37, the history of the normalized C_D value is presented. The C_D value for the SM simulation, is shown to have a less oscillatory behaviour around its mean value and a more stable performance compared with the RWBC unsteady simulation. For the latter, the C_D value its shown to have more peaks during its convergence with a less stable behaviour.

In Figures 5.38, 5.39 and 5.40 the convergence of the velocity components, the pressure and the $\widetilde{\nu}$ is presented for the RWBC, MRF and SM simulation respectively.

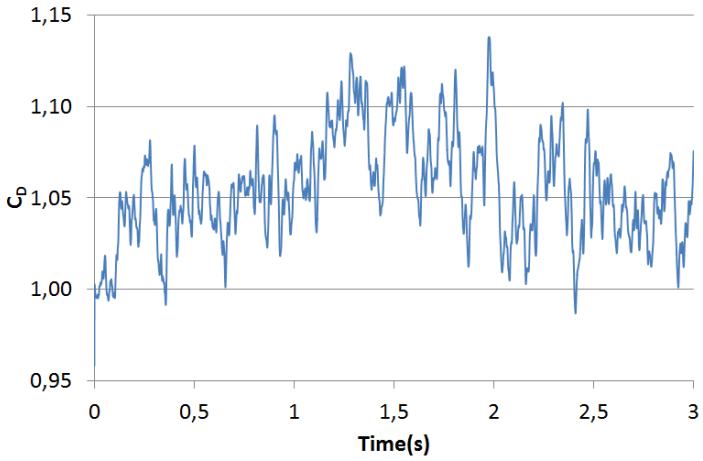

Figure 5.35: Time history of the unsteady normalized C_D value for the RWBC unsteady simulation.

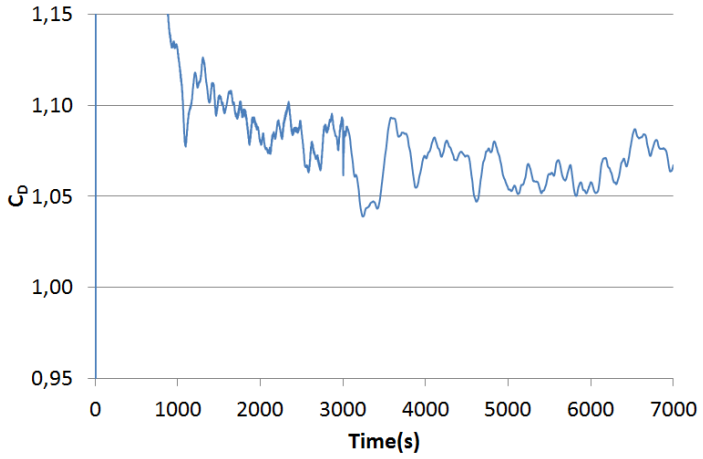

Figure 5.36: Time history of the steady normalized C_D value for the MRF model steady state simulation.

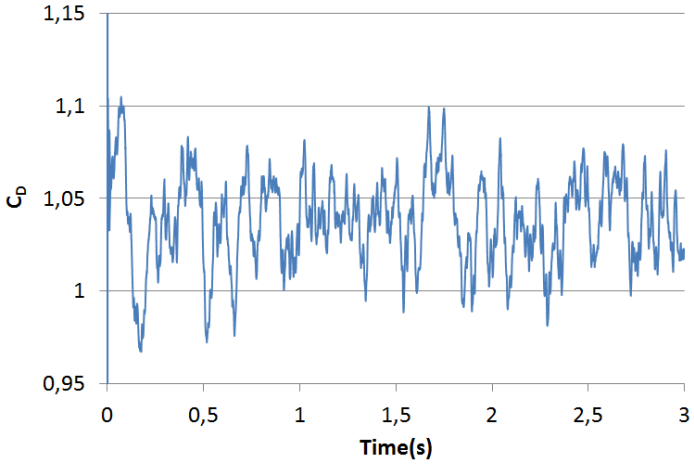

Figure 5.37: Time history of the unsteady normalized C_D value for the SM unsteady simulation.

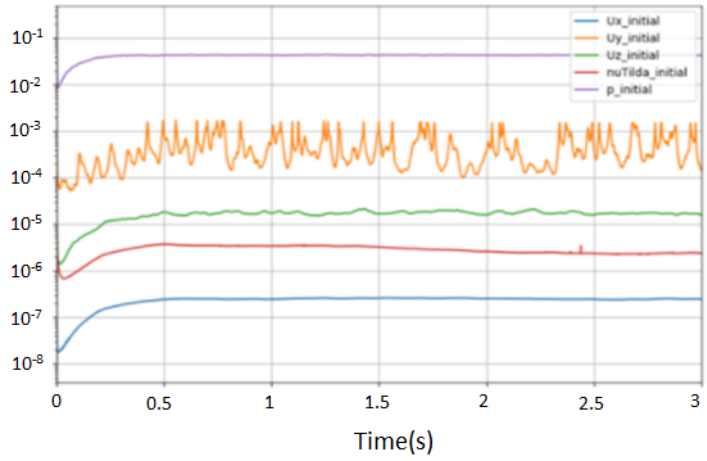

Figure 5.38: Residuals of the governing equations over simulation time for the RWBC simulation.

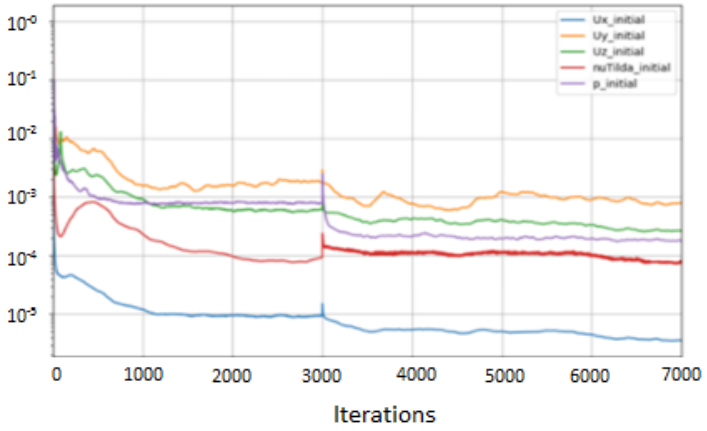

Figure 5.39: Residuals of the governing equations over the solver's iterations for the MRF simulation.

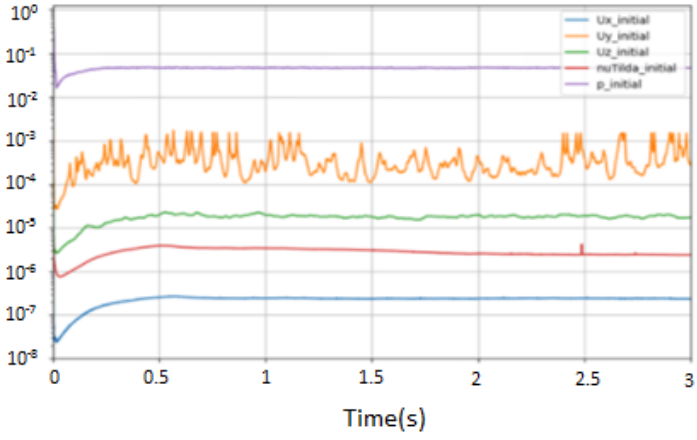

Figure 5.40: Residuals of the governing equations over simulation time for the SM simulation.

Correlation with Experimental Measurements

For the comparison of the computed flow fields, two planes were used for the data visualization in the vicinity of one of the rotating wheels of the car. In Figures 5.41, 5.42, positions of the two planes and size are presented w.r.t the car model size and position.

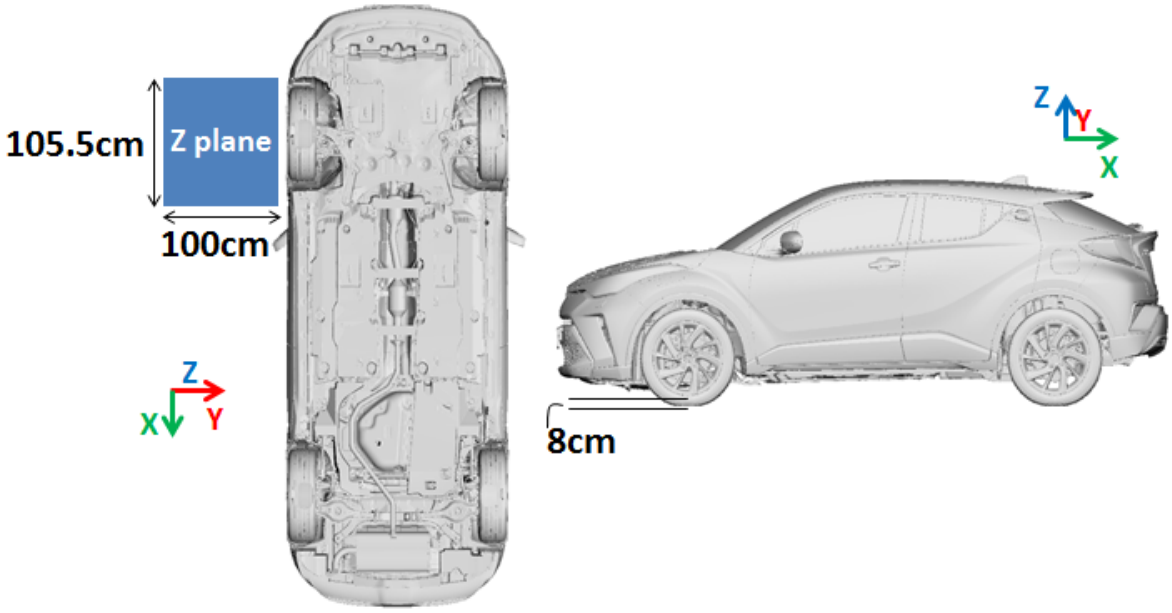

Figure 5.41: The size and position of the Z plane relatively to the car.

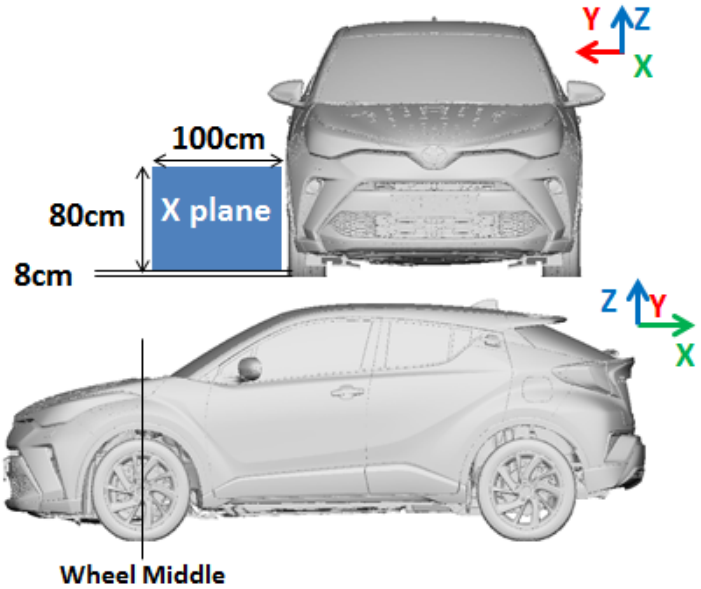

Figure 5.42: The size and position of the X plane relatively to the car.

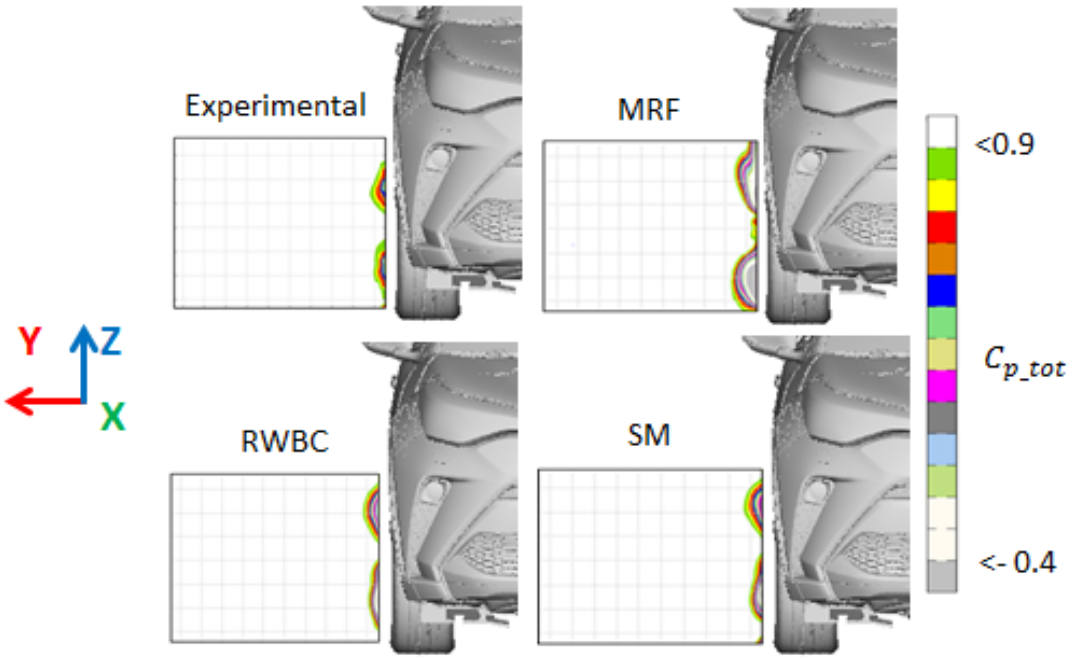

Figure 5.43: Distribution of the total pressure coefficient ($C_{p,Total}$) on the X plane.

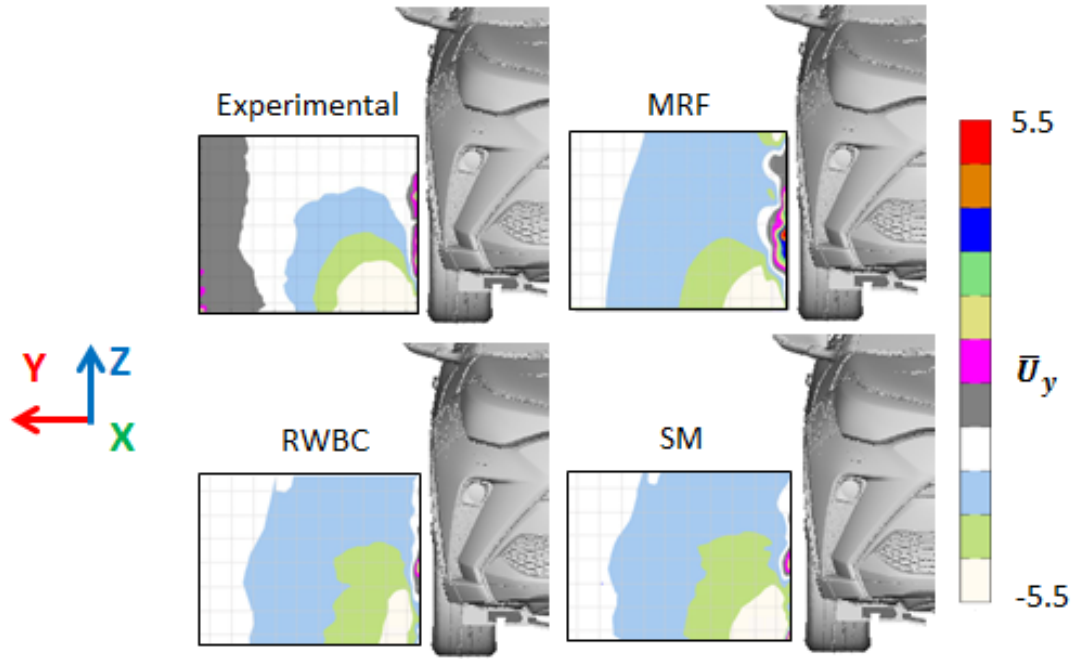

Figure 5.44: Distribution of the mean velocity Y component on the X plane.

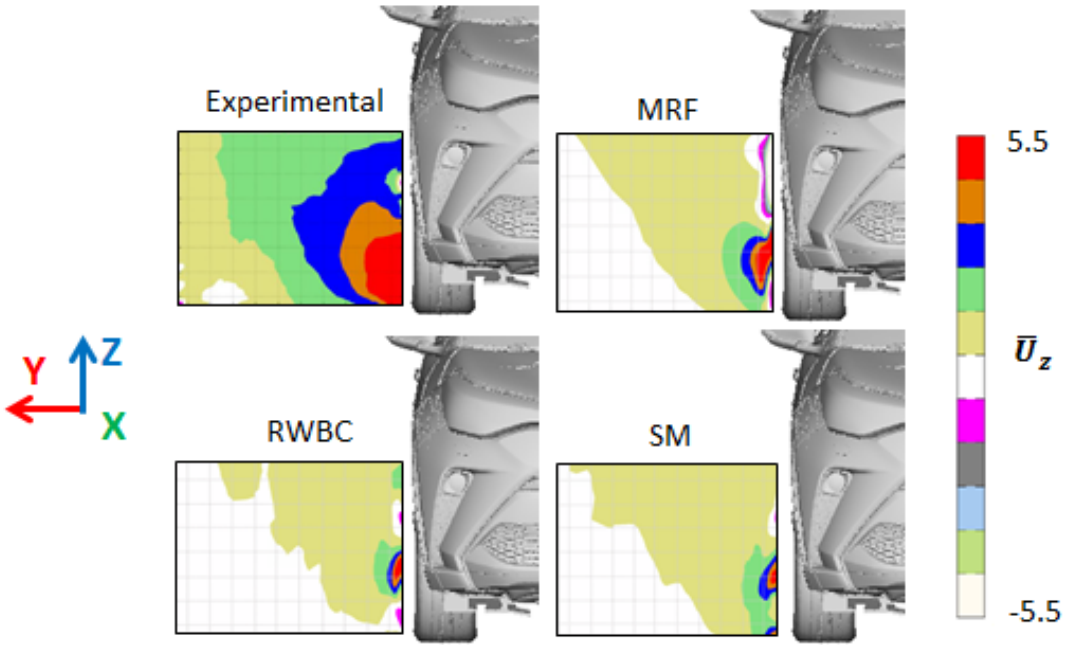

Figure 5.45: Distribution of the mean velocity Z component on the X plane.

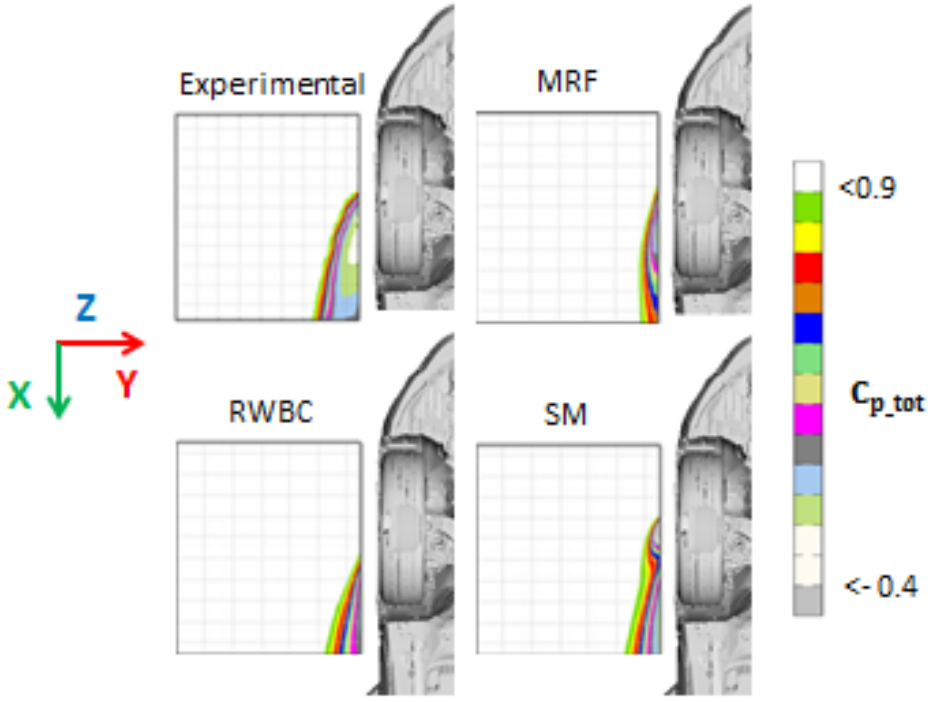

Figure 5.46: Distribution of the total pressure coefficient ($C_{p,Total}$) on the Z plane.

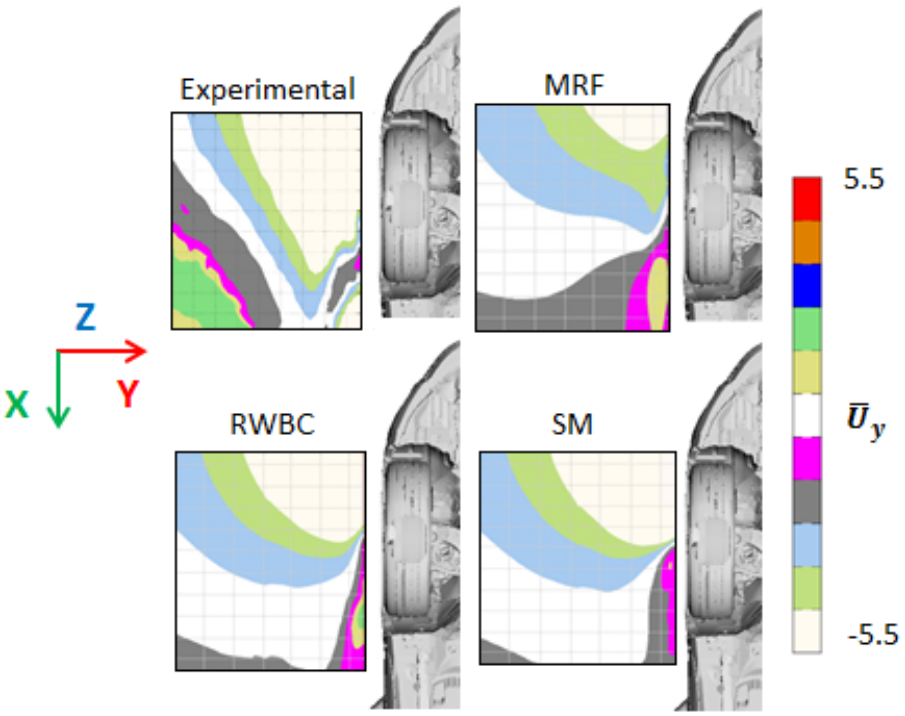

Figure 5.47: Distribution of the mean velocity Y component on the Z plane.

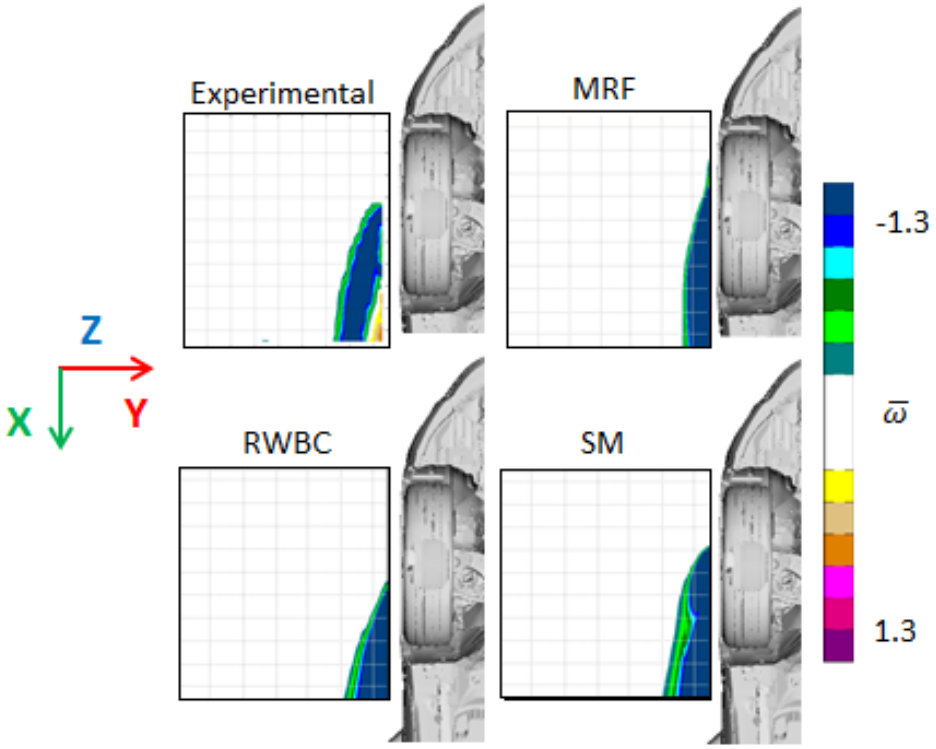

Figure 5.48: Distribution of the mean vorticity magnitude on the Z plane.

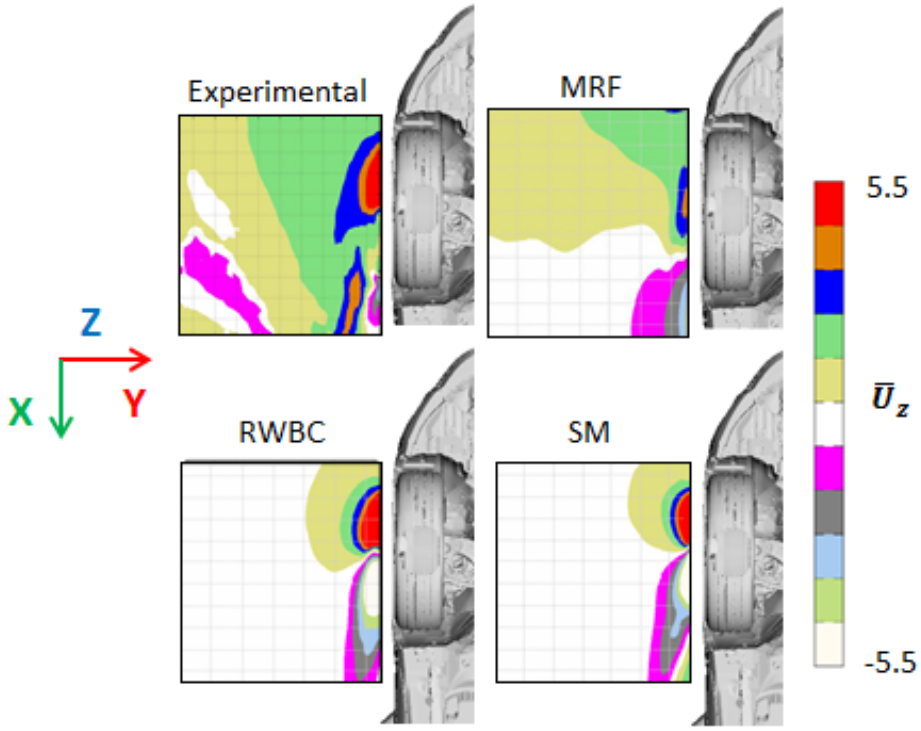

Figure 5.49: Distribution of the mean velocity Z component on the Z plane.

From the comparison of the experimental with the MRF, RWBC and SM simulations, it is clear that a steady state analysis using the MRF model is not adequate to describe the turbulent complex wakes around the car rotating wheels. An unsteady simulation must be carried out in order to predict in a higher accuracy the turbulent wake of the close-to-wheel area. In this area, the MRF model predicted a totally different wake flow structure both close to and far from the rotating wheel.

Results from the RWBC and the SM unsteady simulations show a good agreement. Both show inability to predict the flow field in full agreement with the wind tunnel measurements especially in the area far for the wheel as it can be seen in Figures 5.44, 5.45, 5.47 and 5.49. In Figures 5.47 and 5.44, the RWBC and SM simulations computed a very thin region of high values of the Y velocity component in the near to the wheel area which is closer to the experimental data. In Figure 5.49, the RWBC and SM simulations successfully computed a bubble-shaped region of high value of the Y velocity component close to the wheel, as the experimental data suggests. Both RWBC and SM models, show relatively well predicted flow fields for the total pressure coefficient, Figures 5.43, 5.46.

The SM method differentiates from the RWBC, delivering more accurate results in the case of the total pressure coefficient, as seen in Figures 5.43, 5.29, and also in the prediction of the mean vorticity magnitude field in the Z plane delivering very good correlation with the experimental results, Figure 5.48.

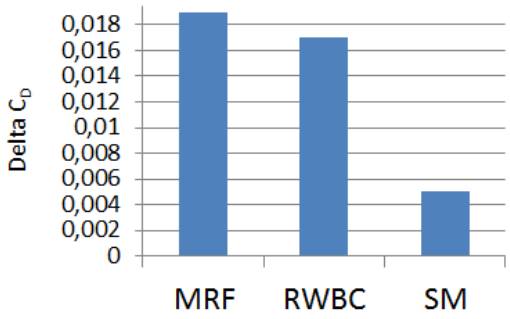

Figure 5.50: The Delta C_D value for the MRF, RWBC and SM simulations.

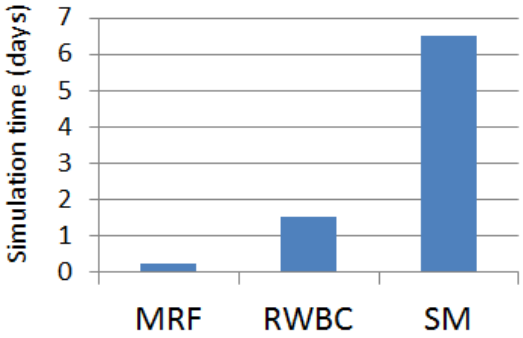

Figure 5.51: The simulation time for the MRF, RWBC and SM simulations.

In Figure 5.50, the Delta values of the C_D coefficient between the experimental and the computational data is presented. As it can be seen, the SM method introduces a smaller Delta value, in comparison with the MRF and the RWBC simulations. This difference between the Delta C_D values for the SM and RWBC model, stands for a noticeable improvement for the drag coefficient prediction for the SM model.

The importance of graph 5.50 is very high because it shows the potential of the SM method to deliver a much more accurate prediction of the drag coefficient as well as the strong impact that wheel rotation can have on the overall aerodynamic performance of the car. Choosing less accurate models than the SM, the CFD analysis neglects a large portion of the rim rotation effect on the flow, predicting different aerodynamic KPIs. The time demanded for the comparison between the experimental and the computational results is not always feasible in a highly paced industrial workflows. Thus, the aerodynamic development may be based on the evaluation of car aerodynamic performance mainly according to the C_D value predicted by CFD. An industrial workflow can be highly benefited from the SM method that delivers accurate results for a different number of rim designs.

Finally, the SM method needed almost four times the simulation time of the RWBC simulation, Figure 5.51. This introduces the demand for the AMI source code optimization in order for the SM to operate faster.

6. Summary and Conclusions

6.1 Summary

In this work, the SM method's potential for the accurate prediction of aerodynamic performance of a passenger car was evaluated using the snappyHexMesh mesh generation software. Preliminarily, an investigation over the AMI shape and the snappyHexMesh parameters was conducted in order to come up with a meshing technique capable of delivering high quality AMI mesh with low face count at the interfaces. The impact of the AMI weighting on the flow fields, the aerodynamic drag and the simulation time was studied with the comparison of four different AMI interfaces on a single rotating wheel SM simulation. The SM method was applied for the wheel rotation modelling in a full car CFD simulation using the meshing technique obtained by the aforementioned parametric investigation. The numerical flow analysis over the car was conducted using the DDES S-A turbulence with wall functions. The SM aerodynamic results were presented on two planes close to the wheel in order to capture the turbulent wheel wake produced by the rotating rim. The SM results were compared with the RWBC, the MRF and experimental data. Finally, the Delta C_D values, w.r.t. the wind-tunnel measurements, for the RWBC, MRF and SM simulations were compared.

6.2 Conclusions

The snappyHexMesh shows a potential for the AMI interfaces geometry resolution with a low number of AMI faces. For this to be done, a parametric investigation of the mesher's parameters and the AMI shape was necessary. Applying this meshing technique, AMI interfaces with average sum of AMI weights during a full rotation of the interface close to 1 were generated. Additionally, extra refinement on the AMI edges was not applied, leading to 50% reduction in AMI faces from the refined one, demonstrating 25% decrease in simulation time.

In the full car simulations, the SM method, was superior to the MRF and the RWBC models w.r.t. its prediction accuracy regarding the aerodynamic vehicle behaviour. The SM method proved its accuracy potential on the computation of the

Delta C_D value delivering a way smaller value equal to 0.005 and good agreement with the experimental data. The SM method is showed to be highly time consuming with the time increase depending on the AMI face count rather than the overall mesh cell size. The flow prediction over the car needed four times the run time of the RWBC simulation. The latter arises as the main drawback of the SM method that needs to resolved.

6.3 Proposals for Future Work

This work shows areas of high interest to be further investigated as the following:

- The SM method must be similarly evaluated and applied in a variety of rim designs for the method's ability to accurately predict the car's aerodynamic behaviour after minor design modifications.
- The impact of lower AMI weightings (less than 1) on the prediction of the car aerodynamic behaviour should be evaluated. Whenever high quality meshing is not achieved the possibility of the use of less well meshed AMIs should be studied.
- Improvements on the AMI code must be followed and supported regarding the code speed up and optimization.

ΕΘΝΙΚΟ ΜΕΤΣΟΒΕΙΟ ΠΟΛΥΤΕΝΧΕΙΟ
Διατμηματικό Μεταπτυχιακό Πρόγραμμα Υπολογιστικής Μηχανικής
Σχολή Μηχανολόγων Μηχανικών
Μονάδα Παράλληλης Υπολογιστικής Ρευστομηχανικής &
Βελτιστοποίησης

Διερεύνηση Τεχνικών Πλεγματοποίησης στη CFD Μοντελοποίηση Περιστροφής Τροχών Αυτοκινήτων

Εκτενής Περίληψη Μεταπτυχιακής Εργασίας

Αλέξανδρος Παπακωνσταντίνου

Επιβλέπων: Κυριάκος Χ. Γιαννάκογλου,
Καθηγητής ΕΜΠ

Αθήνα, Φλεβάρης 2021

7. Εκτενής Περίληψη στα ελληνικά

Εισαγωγή

Η συνεισφορά των περιστρεφόμενων τροχών στην συνολική αεροδυναμική αντίσταση ανέρχεται στο 30%, το εξωτερικό σχήμα του οχήματος συμπεριλαμβανομένου συστήματος ψύξης συνεισφέρει κατά 50% στην αεροδυναμική αντίσταση, ενώ το κάτω μέρος κατά 20%. Τα τελευταία χρόνια, το ενδιαφέρον μετατοπίζεται στην μελέτη των ροικών φαινομένων γύρω από τους τροχούς και τον αεροδυναμικό σχεδιασμό τους.

Σκοπός της εργασίας αυτής είναι η εφαρμογή και αξιολόγηση γρήγορης και ακριβούς μεθόδου πρόλεξης των αεροδυναμικών χαρακτηριστικών επιβατικών οχημάτων με περιστρεφόμενους τροχούς. Χρησιμοποιήθηκε η μέθοδος του Ολισθαίνοντος Πλέγματος με χρήση του πλεγματοποιητή snappyHexMesh και της τεχνικής AMI για τη σύζευξη των στατικού και περιστρεφόμενου χωρίου. Για τη διασφάλιση ακρίβειας και ταχύτητας της σύζευξης, η μέθοδος απαιτεί τη γένεση υψηλής ποιότητας πλέγματος στη διεπιφάνεια ολίσθησης.

Μοντελοποίηση Ροής

Για την ανάλυση της τυρβώδους ροής εφαρμόζονται δύο προσεγγίσεις. Η πρώτη προσέγγιση είναι αυτή των RANS εξισώσεων μαζί με το μοντέλο των Spalart-Allmaras. Η δεύτερη προσέγγιση στη μοντελοποίηση τυρβώδους μη-μόνιμου πεδίου γίνεται με τη χρήση του μοντέλου DDES, σύμφωνα με το οποίο επιλύονται οι εξισώσεις RANS κοντά στα στερεά τοιχώματα και οι LES μακριά από αυτά. Και στις δύο προσεγγίσεις, χρησιμοποιούνται συναρτήσεις τοίχου για τον υπολογισμό των τυρβωδών μεταβλητών στη περιοχή κοντά στα στερεά τοιχώματα χωρίς τη χρήση πολύ πυκνού πλέγματος στις εν λόγω περιοχές.

Μέθοδοι Μοντελοποίησης Περιστροφικής Κίνησης

Μέθοδος μη-μηδενικής Εφαπτομενικής Ταχύτητας: Σύμφωνα με τη μέθοδο αυτή, διάνυσμα ταχύτητας εφαρμόζεται εφαπτομενικά στην επιφάνεια του περιστρεφόμενου σώματος. Για την εφαρμογή της αρχής διατήρησης μάζας, η επιβολή διανύσματος

ταχύτητας κάθετου στην επιφάνεια του σώματος θα υποδήλωνε ροή διαμέσου του τοιχώματος παραβιάζοντας τοπικά την αρχή αυτή. Για αυτό το λόγο, επιφάνειες κάθετες στη φορά περιστροφής μοντελοποιούνται λανθασμένα. Η μέθοδος εφαρμόζεται με επιλύτες μόνιμης και μη-μόνιμης ροής.

Μέθοδος Πολλαπλών Συστημάτων Αναφοράς: Επιλύονται οι εξισώσεις μόνιμης ροής σε σχετικό σύστημα ως προς το ολικό σύστημα αναφοράς. Με αυτό τον τρόπο επιπρόσθετοι όροι πηγής προκύπτουν στις εξισώσεις διατήρησης ορμής προσεγγίζοντας την περιστροφική κίνηση χωρίς την περιστροφή πλέγματος.

Μέθοδος Ολισθαίνοντος Πλέγματος: Μέσω διαχωρισμού του πλέγματος σε δύο γειτονικά και ανεξάρτητα χωρία, υλοποιείται περιστροφή του πλέγματος. Κατά την γένεση αλλά και την περιστροφή του χωρίου, προκύπτει μη-σύμμορφο (non-matching) πλέγμα τοπικά στη διεπιφάνεια στατικού-περιστρεφόμενου χωρίου. Απαραίτητη είναι η διασφάλιση της σύζευξης των χωρίων, για την όσο το δυνατόν ακριβέστερη πρόλεξη του πεδίου ροής, η οποία πραγματοποιείται μέσω της τεχνικής Διεπαφής Αυθαίρετων Πλεγμάτων (AMI).

Τεχνική Διεπαφής Αυθαίρετων Πλεγμάτων (AMI)

Μέσω της AMI, γίνεται ο υπολογισμός των ροών πάνω στη μη-σύμμορφη διεπιφάνεια μέσω παρεμβολής με χρήση βαρών, για την ανταλλαγή πληροφορίας ροής ανάμεσα στα εκατέρωθεν γειτονικά κελιά. Μέσω της προβολής των γειτονικών χωρίων (source-target) πάνω σε ενδιάμεσο επίπεδο (supermesh), Σχήμα 3.8, γίνεται υπολογισμός των AMI βαρών ως ο λόγος του εμβαδού επιφανείας αλληλοκαλυπτόμενων εδρών, εκφράζοντας την ποιότητα της AMI σύζευξης. Η τιμή αθροιστικά των βαρών σε κάθε έδρα κυψέλης θα πρέπει να ισούται με 1, δηλώνοντας απόλυτη συναρμογή των γειτονικών χωρίων.

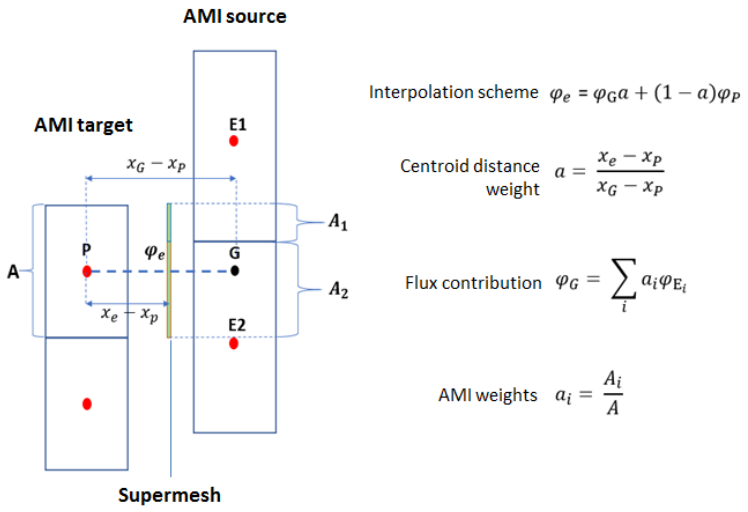

Figure 7.1: 2D αναπαράσταση του AMI υπερπλέγματος κατά την AMI παρεμβολή, από [38].

Πλεγματοποιητής snappyHexMesh

Για τη γένεση του υπολογιστικού πλέγματος χρησιμοποιείται το λογισμικό snappyHexMesh, το οποίο βασίζεται στη διαμέριση πλέγματος βάσης σε εξάεδρα και την πύκνωση πλέγματος στο χωρίο (castellation). Γίνεται προσαρμογή του πλέγματος πάνω στις επιφάνειες ακολουθώντας τη γεωμετρία και τέλος πραγματοποιείται προσθήκη οριακών στοιβάδων κοντά στα στερεά τοιχώματα (viscous layer addition). Σε κάθε στάδιο της πλεγματοποίησης, πραγματοποιείται έλεγχος ποιότητας του πλέγματος βάσει κατάλληλων κριτηρίων.

Εφαρμογές

Μεμονωμένος Τροχός

Οι αρχικές προσπάθειες εφαρμογής της μεθόδου Ολισθαίνοντος Πλέγματος σε τροχούς οχημάτων με τη χρήση προ-καθορισμένων παραμέτρων του snappyHexMesh και αρχικής AMI γεωμετρίας, οδήγησαν σε ατέλειες στο πλέγμα στις δύσκολες και έντονες γωνίες της AMI διεπιφάνειας. Με αυτό τον τρόπο προκύπτουν ανόμοια χωρία AMI source και AMI target και κατά την αλληλοκάλυψη τους υπολογίζονται αρθροίσματα AMI βαρών που αποκλίνουν από τη μονάδα, Σχήμα 7.2.

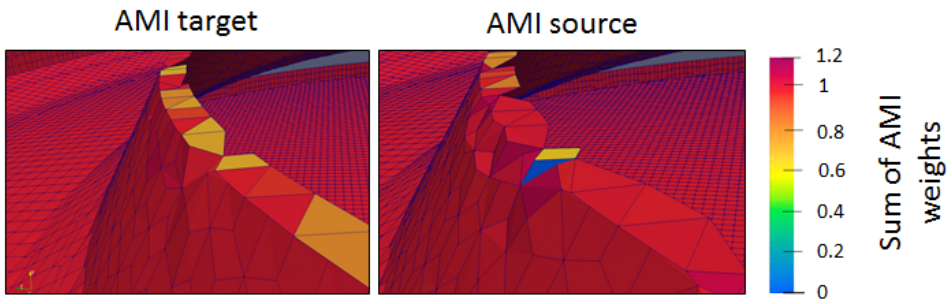

Figure 7.2: Ανόμοια AMI source και AMI target χωρία, λόγω ατελειών του πλέγματος στη ακμή της AMI γεωμετρίας, και το άθροισμα των AMI βάρων που υπολογίζονται.

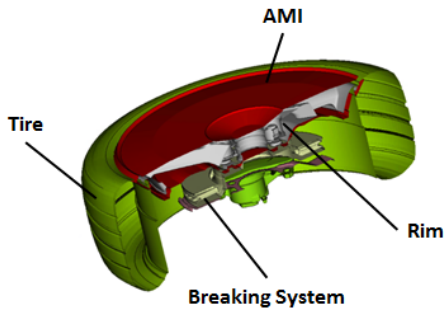

Figure 7.3: Τομή της γεωμετρίας του τροχού και της AMI διεπιφάνειας.

Διερεύνηση Παραμέτρων Πλεγματοποίησης

Για την αντιμετώπιση των ατελειών πλεγματοποίησης στις έντονες ακμές της AMI γεωμετρίας, πραγματοποιήθηκε διερεύνηση των τιμών των παραμέτρων πλεγματοποίησης και της γεωμετρίας AMI σε μεμονωμένο τροχό αυτοκινήτου. Γίνεται αξιολόγηση της επίδρασης των παραμέτρων πλεγματοποίησης με τον υπολογισμό του μέσου αθροίσματος των AMI βαρών για κάθε επιφανειακό κελί σε κάθε χρονική στιγμή κατά μία πλήρη περιστροφή της AMI διεπιφάνειας. Ως στόχος τέθηκε η επίτευξη μέσου αθροίσματος AMI βαρών όσο το δυνατόν πιο κοντά στη μονάδα. Διατηρείται σταθερή AMI γεωμετρία κατά την εναλλαγή των παραμέτρων και χρησιμοποείται επιπρόσθετη πύκνωση στις έντονες γωνίες της AMI γεωμετρίας και στις τομές της AMI με άλλες επιφάνειες του τροχού, Σχήμα 7.3. Το χωρίο βάσης που χρησιμοποιείται κατά τη διερεύνηση φαίνεται στο Σχήμα 7.4.

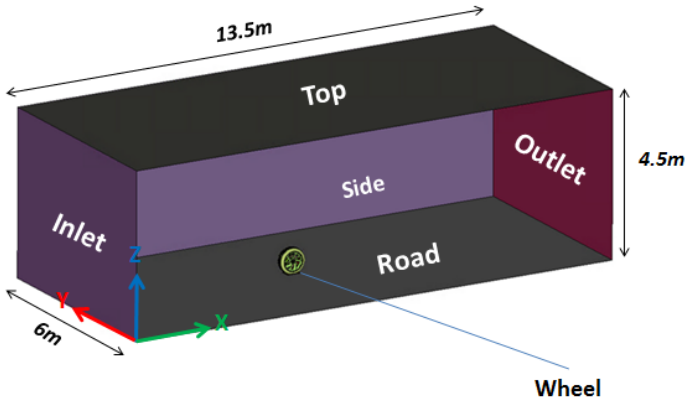

Figure 7.4: Διαστάσεις χωρίου βάσης για το μεμονωμένο τροχό.

Στο Σχήμα 7.5, παρουσιάζεται η συνολική επίδραση των παραμμέτρων πλεγματοποίησης στο μέσο άθροισμα των AMI βαρών συγκριτικά με το αρχικό σετ παραμέτρων. Η βελτίωση της ποιότητας πλέγματος φαίνεται και ως προς την εικόνα του πλέγματος, ακολουθώντας με καλύτερο τρόπο την AMI γεωμετρία, στις έντονες γωνίες της AMI και στην τομή της με άλλες επιφάνειες.

Διερεύνηση Τύπου Τομών Επιφανειών

Για την περαιτέρω βελτίωση των ατελειών πλεγματοποίησης στη δύσκολη περιοχή των τομών της AMI διεπιφάνειας με τις επιφάνειες του τροχού (ελαστικό, ζάντα, συνιστώσες συστήματος πέδησης), Σχήμα 7.3, πραγματοποιήθηκε διερεύνηση της μορφολογίας της τομής αυτής. Στόχος είναι η διατήρηση της ποιότητας των εξαέδρων, που παράγονται κατά την διαμέριση του πλέγματος βάσης, στη περιοχή των τομών AMI-patches. Στην εργασία αυτή, ο προσανατολισμός των εξαεδρικών κελιών είναι ίδιος με αυτόν του ολικού

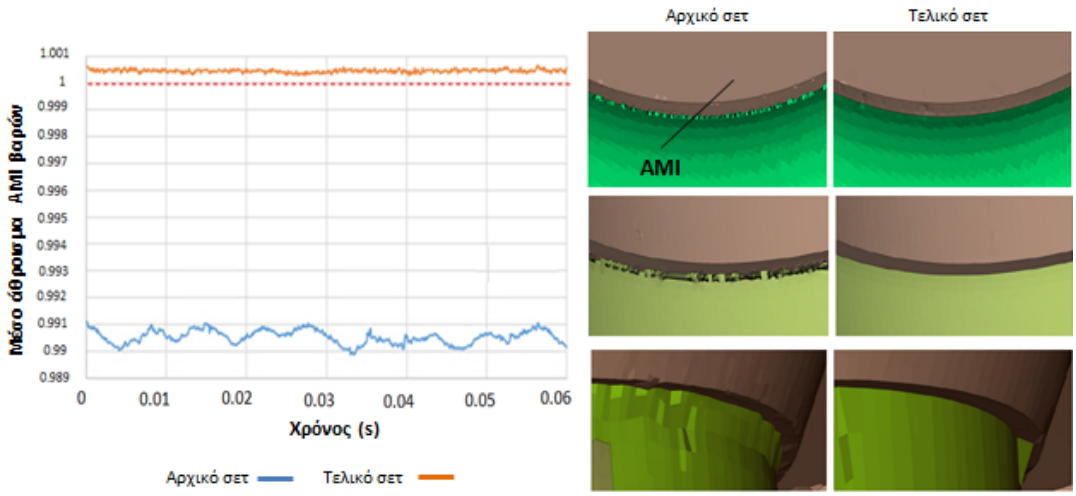

Figure 7.5: Συνολική βελτίωση της AMI ποιότητας υπό την επίδραση του τελικού σετ παραμέτρων πλεγματοποίησης. Αριστερά: Ποσοτική αξιολόγηση μέσω της βελτίωσης του επιπέδου του μέσου αθροίσματος AMI βαρών. Δεξιά: Οπτική αξιολόγηση της επίδρασης του τελικού σετ παραμέτρων στις γωνίες και στις τρεις τομές της AMI διεπιφάνειας με άλλα patches.

σύστημα συντεταγμένων, Σχήμα 7.6, λόγω της θέσης του πλέγματος βάσης. Οι τύποι τομής AMI-patches που χρησιμοποιήθηκαν είναι οι παρακάτω:

Αρχική: Προκύπτει από την εφαρμογή AMI διεπιφάνειας κατασκευασμένης με κριτήριο την διατήρηση σταθερής απόστασης από τα patches τροχού και ζάντας και χωρίς την εφαρμοφή των παραμέτρων που προτάθηκαν.
Ένα κεκλιμένο: Διαμόρφωση που ευνοεί την διατήρηση της ποιότητας των εξαέδρων στην τομή, με την γεωμετρική τροποποίηση μίας εκ των επιφανειών στη τομή. Έγινε εφαρμογή των προτεινόμενων παραμέτρων πλεγματοποίησης.
Κανένα Κεκλιμένο: Διαμόρφωση τομής χωρίς έντονες ή μεγάλες γωνίες, για την προσαρμογή εξαεδρικών κελιών με την υψηλότερη δυνατή ποιότητα στη περιοχή της τομής, με εφαρμογή των παραμέτρων πλεγματοποίησης που προτάθηκαν.
Κανένα Κεκλιμένο - καμμία επιπλέον πύκνωση: Χρήση του τύπου τομής *Κανένα Κεκλιμένο*, αλλά χωρίς την περαιτέρω πύκνωση του πλέγματος στις έντονες ακμές της AMI γεωμετρίας. Γίνεται γένεση πλέγματος στην AMI διεπιφάνεια με ομοιόμορφη κατανομή μεγέθους επιφανειακών κελιών, δίνοντας τα καλύτερα επίπεδα AMI βαρών που ευρέθησαν αλλά και μειωμένο πλήθος AMI επιφανειακών κελιών.

Ο τύπος τομής *Κανένα Κεκλιμένο - καμμία επιπλέον πύκνωση* σε συνδιασμό με το προτεινόμενο σετ τιμών παραμέτρων πλεγματοποίησης αποτελεί τη τεχνική πλεγματοποίησης που προτείνεται. Η ευρωστία της τεχνικής αυτής επικυρώθηκε σε έξι διαφορετικούς τύπου τροχών.

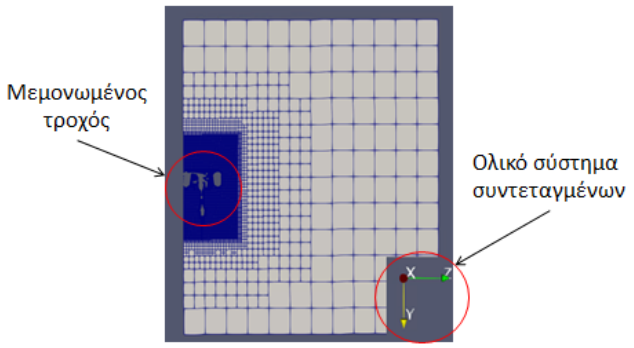

Figure 7.6: Τομή του CFD πλέγματος για τη διερεύνηση πάνω μεμονωμένο τροχό.

Figure 7.7: Η απόδοση του μέσου αθροίσματος AMI βαρών για τις διαφορετικού τύπου τομές, κατά μία πλήρη περιστροφή της AMI διεπιφάνειας.

Ανάλυση Ροής Γύρω από Μεμονωμένο Περιστρεφόμενο Τροχό

Εφαρμόσθηκε η μεθόδος Ολισθαίνοντος Πλέγματος σε μεμονωμένο τροχό, με χρήση τεσσάρων AMI διεπιφανειών με διαφορετικό επίπεδο τιμών μέσων αθροισμάτων AMI βαρών, Σχήμα 7.8, για τη μελέτη επίδρασης αυτών στο χρόνο επίλυσης και στη πρόλεξη αεροδυναμικών χαρακτηριστικών. Η σύγκριση ανάμεσα στα αποτελέσματα με χρήση των διαφορετικών AMI είναι παράπλευρη καθώς δεν υπήρχαν διαθέσιμες πειραματικές τιμές. Οι AMI διεπιφάνειες που χρησιμοποιήθηκαν είναι οι παρακάτω:

Αρχική: Κατακευάστηκε χωρίς τη χρήση των παραμέτρων πλεγματοποίησης και της AMI γεωμετρίας που προτάθηκε.

Αραιή 1: Κατασκευάστηκε με εφαρμοφή της τεχνικής πλεγματοποίησης που προσδιορίστηκε, αλλά με χρήση αιραιώτερου πλέγματος στην διεπιφάνεια.
Αραιή 2: Κατασκευάστηκε με εφαρμοφή των τιμών παραμέτρων πλεγματοποίησης και γεωμετρίας που προτάθηκαν.
Πυκνή: Κατασκευάστηκε με εφαρμοφή της τεχνικής πλεγματοποίησης που προσδιορίστηκε, αλλά με χρήση πυκνώτερου πλέγματος στις γωνίες της διεπιφάνειας.

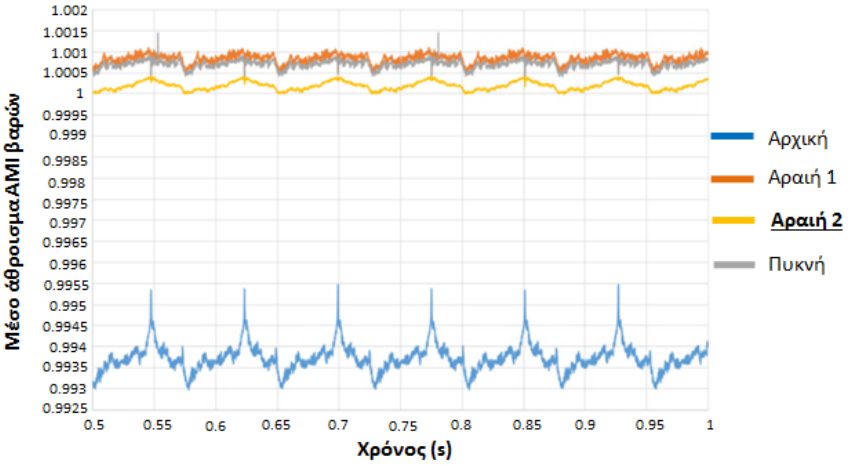

Figure 7.8: Το μέσο άθροισμα AMI βαρών για τις τέσσερις AMI διεπιφάνειες κατά τη διάρκεια 0.5 sec επίλυσης.

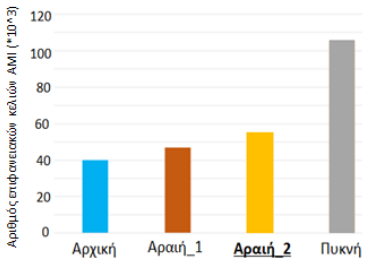

Figure 7.9: Πλήθος AMI κελιών στις τέσσερις διεπιφάνειες.

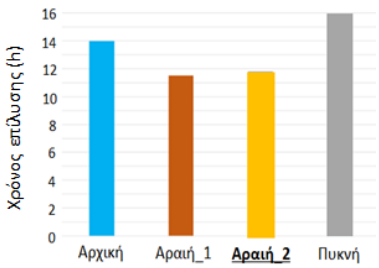

Figure 7.10: Χρόνος επίλυσης για τις τέσσερις AMI διεπιφάνειες.

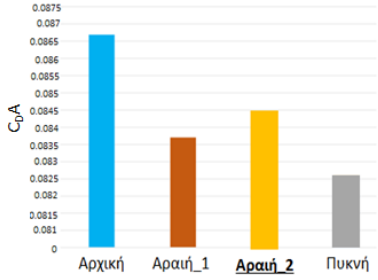

Figure 7.11: Τιμές C_DA για τις τέσσερις AMI διεπιφάνειες.

Εφαρμογή σε Αυτοκίνητο Παραγωγής

Έγινε εφαρμογή της μεθόδου Ολισθαίνοντος Πλέγματος για την πρόλεξη πεδίου μη-μονιμης ροής γύρω από επιβατικό όχημα με περιστρεφόμενους τροχούς σε μοντέλο ολόκληρου αμαξιού (full car), Σχήμα 7.12, με μοντέλο DDES Spalart-Allmaras με συναρτήσεις τοίχου. Πραγματοποιήθηκε κατασκευή τεσσάρων AMI διεπιφανειών, με εφαρμορφή της τεχνικής πλεγματοποίησης που προτάθηκε, προσδιορίζοντας τα περιστρεφόμενα χωρία για τους τροχούς με $95 \cdot 10^6$ AMI επιφανειακά κελιά. Η μέθοδος

Ολισθαίνοντος Πλέγματος εφαρμόστηκε μόνο στις ζάντες του αυτοκινήτου, καθώς οι υπόλοιπες επιφάνειες μοντελοποιήθηκαν με επιβολή της συνθήκης μη-μηδενικής Εφαπτομενικής Ταχύτητας. Πραγματοποιήθηκε σύγκριση της μεθόδου Ολισθαίνοντος πλέγματος ως προς την πρόλεξη αεροδυναμικών χαρακτηριστικών με τη μέθοδο μη-μηδενικής Εφαπτομενικής Ταχύτητας, εφαρμοζόμενη σε ανάλυση μη-μόνιμης ροής με μοντέλο DDES, και της μεθόδου Πολλαπλών Συστημάτων Αναφοράς εφαρμοζόμενη σε ανάλυση μόνιμης ροής με την επίλυση RANS εξισώσεων αλλά και πειραματικών μετρήσεων. Τα υπολογιστικά και πειραματικά δεδομένα οπτικοποιούνται στα επίπεδα X και Z που παρουσιάζονται στο Σχήμα 7.13.

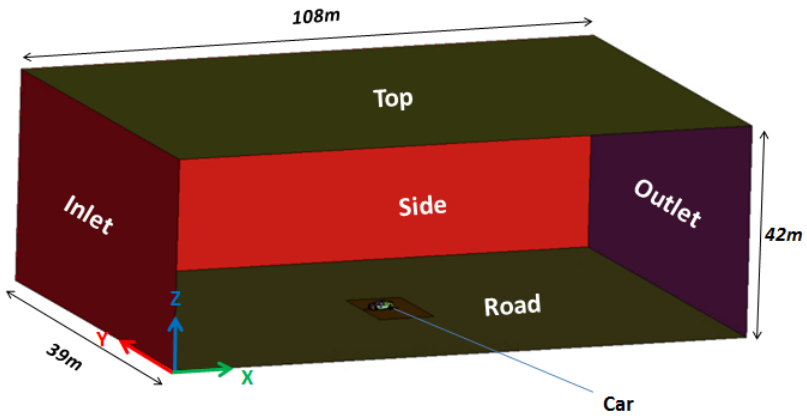

Figure 7.12: Διαστάσεις χωρίου βάσης για τη προσομοίωση ροής γύρων από επιβατικό αυτοκίνητο.

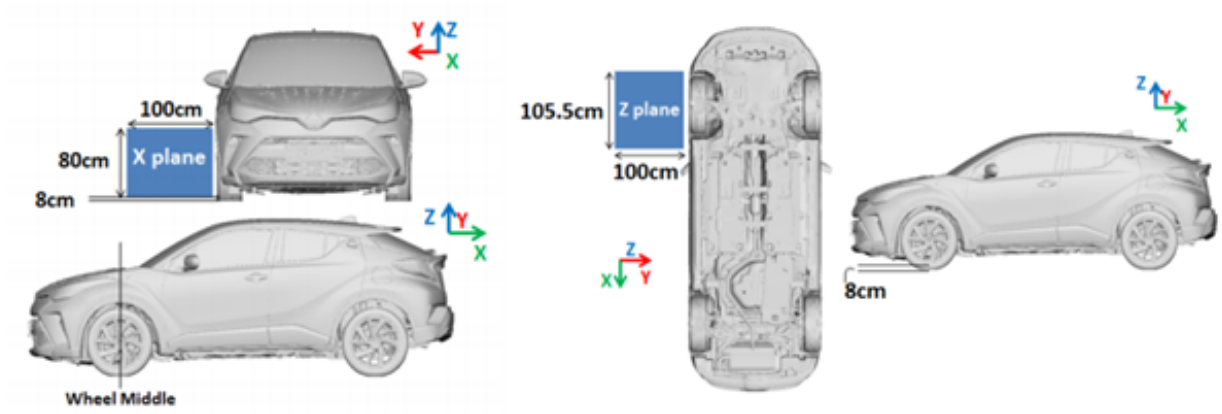

Figure 7.13: Θέση και διαστάσεις του επιπέδου X και του επιπέδου Z.

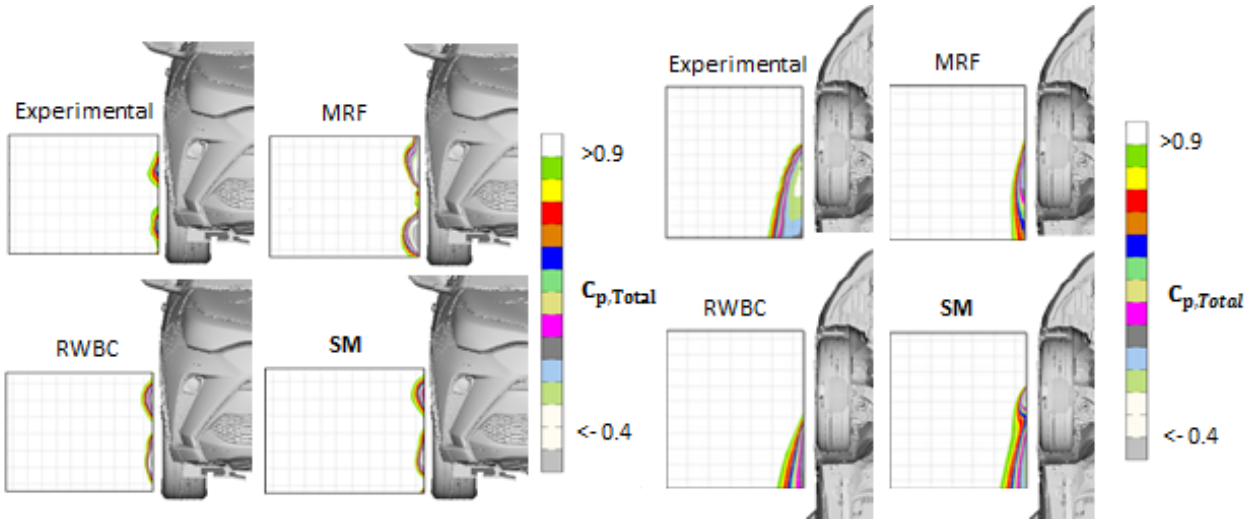

Figure 7.14: Πεδίο του συντελεστή ολικής πίεσης ($C_{p,Total}$) στον ομοόρρου του τροχού. Αριστερά: X επίπεδο. Δεξιά: Z επίπεδο.

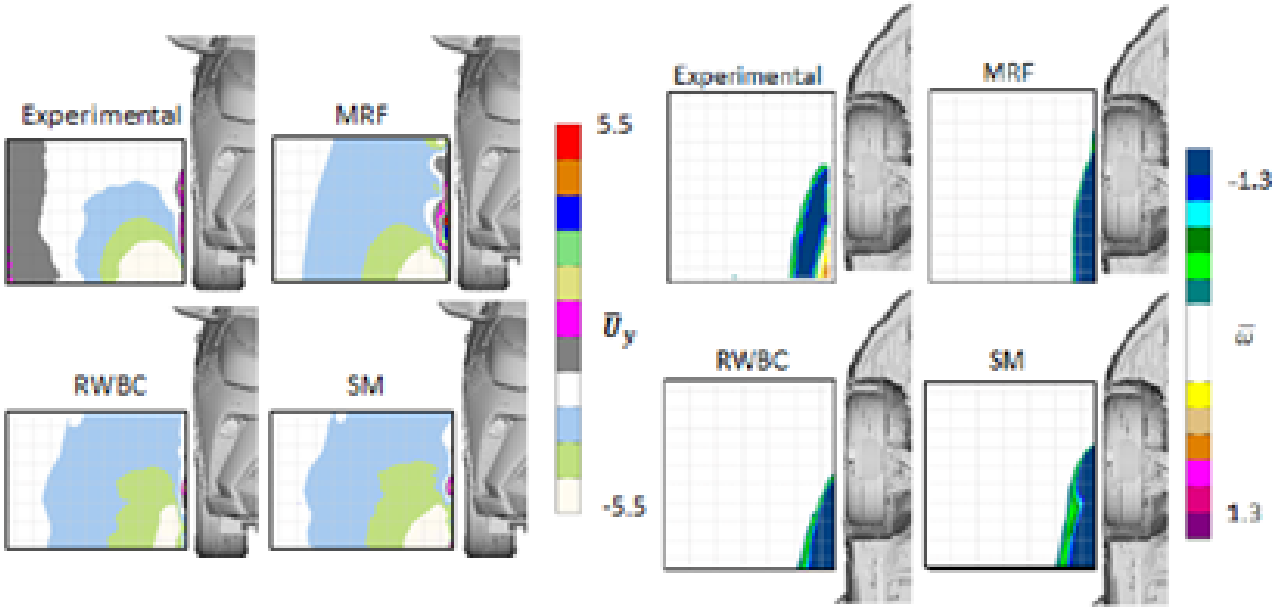

Figure 7.15: Αριστερά: Πεδίο της Y συνιστώσας της μέσης ταχύτητας στο X επίπεδο. Δεξιά: Πεδίο μέτρου μέσου στροβιλισμού στο Z επίπεδο.

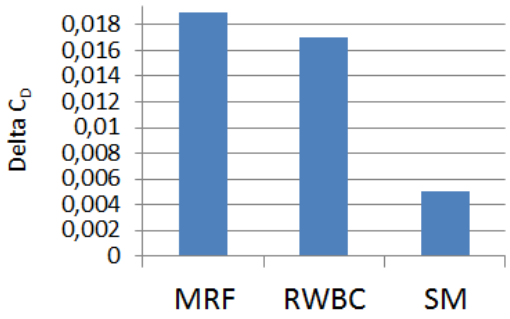

Figure 7.16: Τιμές Δέλτα C_D για τις MRF,RWBC και SM αναλύσεις.

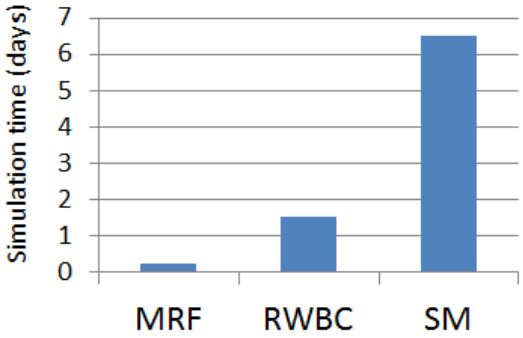

Figure 7.17: Ο χρόνος επίλυσης σε μέρες, για τις MRF,RWBC και SM αναλύσεις.

Σύνοψη

Σε αυτή την εργασία, εφαρμόσθηκε και επικυρώθηκε η ακρίβεια της μεθόδου Ολισθαίνοντος Πλέγματος στην πρόλεξη αεροδυναμικών χαρακτηριστικών σε ροή γύρω από επιβατικό αυτοκίνητο με περιστρεφόμενους τροχούς. Πραγματοποιήθηκε, προκαταρκτική διερεύνηση των παραμέτρων του πλεγματοποιητή snappyHexMesh και της γεωμετρίας της AMI διεπιφάνειας, και προσδιορίστηκε εύρωστη τεχνική πλεγματοποίησης για την γένεση υψηλής ποιότητας πλέγματος στις διεπιφάνειες. Έγινε εφικτή η κατασκευή AMI διεπιφανειών με μέσο άθροισμα AMI βαρών κοντά στη μονάδα. Δεν εφαρμόσθηκε επιπρόσθετη πύκνωση στις ακμές της διεπιφάνειας, οδηγώντας σε 50% μείωση των AMI επιφανειακών κελιών το οποίο είχε σαν αποτέλεσμα τη μείωση του χρόνου επίλυσης κατά 25% . Η μέθοδος Ολισθαίνοντος Πλέγματος έδειξε μεγάλη ακρίβεια στην πρόλεξη του αεροδυναμικού συντελεστή με Δέλτα τιμή (ΔC_D) ίση με 0.005 σε σύγκριση με 0.017 της μεθόδου μη-μηδενικής Εφαπτομενικής Ταχύτητας. Ο χρόνος επίλυσης με τη μέθοδο Ολισθαίνοντος Πλέγματος παρουσιάζεται τέσσερις φορές υψηλότερος από τον χρόνο της μεθόδου μη-μηδενικής Εφαπτομενικής Ταχύτητας.

Bibliography

[1] An official website of the European Union *https* : $//ec.europa.eu/clima/policies/transport/vehicles/regulation_en$

[2] Uriegas, Andrés Contreras. "CFD Investigation on Sliding Mesh as a Method to Model Wheel Rotation - Implementation and Analysis on Different Rims." (2018).

[3] Orszag, S. (1970). Analytical theories of turbulence. Journal of Fluid Mechanics, 41(2), 363-386. doi:10.1017/S0022112070000642

[4] Moukalled, F., Darwish, M., and Mangani, L.: The Finite Volume Method in Computational Fluid Dynamics. An Advanced Introduction with OpenFOAMand MATLAB. Springer, 2016.

[5] P. R. Spalart, S. R. Allmaras, A One-Equation Turbulence Model for Aerodynamic Flows, 30th Aerospace Sciences Meeting and Excibit, Reno, NV, U.S.A. , 1992.

[6] D.L. Sondak, Wall functions for the k-εturbulence model in generalized nonorthogonal curvilinear coordinates, Retrospective Theses and Dissertations. 9954. 1992.

[7] Yang, Z.:Large-eddy simulation: Past, present and the future. Chinese Journalof Aeronautics, 91, December 2014. 10.1016/j.cja.2014.12.007.

[8] P. Farrell, M. Piggott, C. Pain, G. Gorman, C. Wilson, Conservative interpolation between unstructured meshes via supermesh construction, Comput. Methods Appl. Mech. Eng. 198 (2009) 2632–2642.

[9] P. Farrell, J. Maddison, Conservative interpolation between volume meshes by local Galerkin projection, Comput. Methods Appl. Mech. Eng. 200 (2011) 89–100.

[10] M. Berger, On conservation at grid interfaces, SIAM J. Numer. Anal. 24(5) (1987) 967–984.

[11] M. Beaudoin, H. Jasak, Development of a generalized grid interface for turbomachinery simulations with OpenFOAM, in: Open Source CFD International Conference, Berlin, 2008.

[12] H. Jasak, "Error analysis and estimation in the finite volume method with applications to fluid flows," Ph.D. dissertation, Imperial College, University of London, 1996.

[13] T. Lucchini, G. D'Errico, H. Jasak, Z. Tukovic, Automatic Mesh Motion with Topological Changes for Engine Simulation, Tech. rep., SAE technical paper, 2007.

[14] Z. Wang, N. Hariharan, R. Chen, Recent development on the conservation property of chimera, Int. J. Comput. Fluid Dyn. 15(4) (2001) 265–278.

[15] F. Piscaglia, A. Montorfano, A. Onorati, Development of Fully-automatic Parallel Algorithms for Mesh Handling in the OpenFOAM®-2.2.x Technology, Tech. rep., SAE technical paper, 2013.

[16] F. Piscaglia, A. Montorfano, A. Onorati, A moving mesh strategy to perform adaptive large eddy simulation of IC engines in OpenFOAM, in: International Multidimensional Engine Modeling User's Group Meeting, The Detroit Downtown Courtyard by Marriott Hotel, Detroit, MI, USA, 2014.

[17] C. J. Greenshields. OpenFOAM User Guide 5.0. The OpenFOAM Foundation Ltd., 2017. URL http://foam.sourceforge.net/docs/Guides-a4/OpenFOAMUserGuide-A4.pdf. [Online; Retrieved 26.02.2018].

[18] D. B. Spalding, A Single Formula for the "Law of the Wall", Journal of Applied Mechanics, vol. 28, issue 3, 1961.

[19] Spalding, D. B.:A single formula for the law of the wall. Journal of AppliedMechanics, 28:455–457, 1961.

[20] J. Frohlich and D. von Terzi: Hybrid LES/RANS methods for the simulation of turbulent flows. In Progress in Aerospace Sciences Journal, 44(5):349 - 377, 2008.

[21] A. Leonard: Energy cascade in large-eddy simulations of turbulent fluid flows. In Turbulent Diffusion in Environmental Pollution, pages 237-248, 1974.

[22] E. de Villiers: The Potential of Large Eddy Simulation for the Modeling of Wall Bounded Flows. PhD thesis, Thermo uids Section Department of Mechanical Engineering, Imperial College of Science, Technology and Medicine, London, July 2006.

[23] Ph. Spalart,WH Jou, M. Strelets, and S. Allmaras: Comments on the feasibility of les for wings, and on a hybrid rans/les approach. In International Conference on DNS/LES, Aug. 4-8, 1997, Ruston, Louisiana., 1997.

[24] P. R. Spalart, S. Deck, M. L. Shur, K. D. Squires, M. Kh. Strelets, and A. Travin: A new version of detached-eddy simulation, resistant to ambiguous grid densities. In Theoretical and Computational Fluid Dynamics Journal, 20(3):181, May 2006.

[25] Menter, F.R., Kuntz, M., Langtry, R.: Ten years of experience with the SST turbulence model. 4th International Symposium on Turbulence Heat and Mass Transfer, pp. 625–632 (2003)

[26] Menter, F.R., Kuntz, M., Adaptation of Eddy-Viscosity Turbulence Models to Unsteady Separated Flow Behind Vehicles. Proc. Conf. The Aerodynamics of Heavy Vehicles: Trucks, Busses and Trains, Asilomar, Ca, (to be published by Springer, 2003

[27] Teddy Hobeika, Simone Sebben, and Christoffer Landstrom. Investigation of the influence of tyre geometry on the aerodynamics of passenger cars. SAE Int. J. Passeng. Cars - Mech. Syst., 6:316–325, 04 2013.

[28] Wäschle, A., "The Influence of Rotating Wheels on Vehicle Aerodynamics - Numerical and Experimental Investigations", SAE World Congress & Exhibition, (SAE International, Apr. 2007), doi: 10.4271/2007-01-0107.

[29] Haag, L., Blacha, T., and Indinger, T., "Experimental Investigation on the Aerodynamics of Isolated RotatingWheels and Evaluation of Wheel Rotation Models Using Unsteady CFD", International Journal of Automotive Engineering 8(1): 7–14, 2017, doi:10.20485/jsaeijae.8.1_7.

[30] Reiß , Jan & Haag, Lukas & Indinger, Thomas.(2019) . CFD investigation on fully detailed and deformed car tires. International Journal of Automotive Engineering. 10 324-331. 10.20485/jsaeijae.10.4-324

[31] Hobeika, T., Sebben, S., and Lofdahl, L., "Study of Different Tyre Simulation Methods and Effects on Passenger Car Aerodynamics", International Vehicle Aerodynamics Conference 2014, (Holywell Park, Loughborough, UK, 2014): 187–195, isbn: 978-0-08-100199-8.

[32] Lee,M.-H., Shiah, Y., and Bai, C.-J., "Experiments and numerical simulations of the rotor-blade performance for a small-scale horizontal axis wind turbine", Journal of Wind Engineering and Industrial Aerodynamics 149: 17 –29, 2016, issn: 0167-6105, doi: http://dx.doi.org/10.1016/j.jweia.2015.12.002.

[33] Shur, M. L., Spalart, P. R., Strelets, M. K., and Travin, A. K., "A hybrid RANS-LES approach with delayed-DES and wall-modelled LES capabilities", International Journal of Heat and Fluid Flow 29(6): 1638 –1649, 2008, issn: 0142-727X, doi: https://doi.org/10.1016/j.ijheatfluidflow.2008.07.001.

[34] Wittemeier, F, Willey, P, Kuthada, T, Widdecke, N, and Wiedemann, J, "Classification of Aerodynamic Tyre Characteristics", International Vehicle Aerodynamics Conference 2014, (Holywell Park, Loughborough, UK, 2014): 175–185, isbn: 978-0-08-100199-8.

[35] A. Montorfano, F. Piscaglia, A. Onorati An Extension of the Dynamic Mesh Handling with Topological Changes for Les of ICE in OpenFOAM Paper presented at: SAE 2015 World Congress and Exhibition, Detroit, MI, USA, 21-23 April 2015, p. 1-15, 2015-01-0384 doi:10.4271/2015-01-0384

[36] Hobeika, T., Sebben, S. (2018) CFD investigation on wheel rotation modelling Journal of Wind Engineering and Industrial Aerodynamics, 174: 241-251 http://dx.doi.org/10.1016/j.jweia.2018.01.005

[37] S2A, Wind Tunnels: Souffleries aeroacoustiques automobiles. https://www. soufflerie2a.com/en/

[38] F. Piscaglia, A.Montorfano, and F. Giussani. Multidimensional simulation of moving geometries with topological changes by an open source CFD code. 2014.

[39] $https://openfoamwiki.net/index.php/SimpleFoam$

[40] $https://openfoamwiki.net/index.php/OpenFOAM_guide/The_PIMPLE_algorithm_in_OpenFOAMl$